Utrecht University

Master Thesis

The sensitivity of land subsidence model predictions to parametric and structural uncertainties

A case study to groundwater extraction-induced subsidence in New Orleans

---

Author:
R.R. Melman (4099443)

Supervisors:
Dr. L.P.H. van Beek
Dr. G. Erkens

April 4, 2019

Abstract

Ongoing urbanization and agriculture cultivation of river deltas have initiated a wide range of subsidence processes. This makes deltas more vulnerable to floods, salinization and land loss and causes significant economic losses by damage to (natural) constructions. Excessive groundwater use is the main cause of subsidence in many large delta cities. The current rate and extent of this type of anthropogenic subsidence, demonstrates the need for predictive land subsidence models. Such models could be used to identify (future) subsiding areas and test the effect of mitigation measures. Conventional land subsidence studies employ groundwater coupled subsidence models to simulate vertical deformation. Currently, studies that make use of these models have mainly focused on well described study areas. Consequently, limited research has been conducted on how uncertainty due to the limited knowledge of hydraulic and geotechnical parameters and the geological schematization affect land subsidence model predictions. However, in order to make predictive regional land subsidence models globally - including data-scarce areas -, a basic understanding of the model sensitivity to these uncertainties is required. This thesis studied the effects of epistemic uncertainty in the geological schematization and corresponding parameterization of the hydraulic conductivity and geotechnical parameters on land subsidence model predictions on the basis of a land subsidence model of the New Orleans aquifer system. Here, industrial groundwater extractions have been related to land subsidence (Dokka, 2011; Jones et al., 2016).

An eight-layer conceptual hydrogeological model of the aquifer system served as base model. Hydraulic head dynamics were simulated using the MODFLOW-based environment iMOD. Land subsidence calculations were employed by the one-way coupled NEN-Bjerrum model, that decomposes deformation in an elastic and viscous component. To find statistically well performing hydraulic conductivity distributions, parameter calibration (PEST) and uncertainty estimation (GLUE) were combined using hydraulic head observations. Realistic geotechnical parameter combinations with a relatively low contribution of autonomous creep, were selected among the ranges of empirically established geotechnical parameters. These parameter distributions were used to assess the impact of parametric uncertainty on land subsidence predictions. The impact of structural uncertainty on the land subsidence prediction was determined by comparing the model results of a simplified geological schematization with the model predictions of the original eight-layer model. The effects of both parametric and structural uncertainties were all assessed based on three evaluation criteria: magnitude, spatial extent and timing of subsidence.

This study showed that the groundwater extractions in the Norco and Gonzales-NO aquifers contributed to historical land subsidence in the Greater New Orleans area. The best estimate model suggests that the groundwater extractions induced mean cumulative subsidence of 68.5 mm in the study area by 1970, which is the moment of maximum subsidence. Hereafter, the model results indicate significant rebound of the land surface. The magnitude of subsidence ranges significantly over the study area and subsidence hot-spots

were recognized at the industrial facilities at Michoud and Norco. The subsidence predictions demonstrated to be significantly affected by the hydraulic conductivity and geological schematization both with respect to the magnitude and spatial extent of subsidence. This highlights the large dependency of subsidence predictions on reliable hydraulic head predictions. However, the land subsidence predictions showed to be most sensitive to the geotechnical parameterization. Modelled subsidence varied significantly with respect to magnitude, spatial extent and timing of subsidence for different geotechnical parameter combinations. Hence, the in general poor match between subsidence observations (Dokka, 2011; Jones et al., 2016) and model results of this study is likely to be dominated by the uncertainty in geotechnical parameters.

Acknowledgements

Contents

1 Introduction

1.1 Background

The attractiveness of delta areas has resulted in rapid expansion of economic activity, agriculture and urban settlements during the 20th century: close to half a billion people live on or near river deltas (Syvitski et al., 2009). Land subsidence is a natural phenomenon in delta systems, which are composed of unconsolidated compressible sediments (Craig et al., 1979). Ongoing rural and urban expansion and the associated intensified land use enhance natural land subsidence in deltas by multiple mechanisms (Galloway et al., 2016). In urban areas, load-driven compaction by buildings and infrastructure may trigger land subsidence (Galloway et al., 2016). In contrast, drainage of wetlands to prepare for agricultural use drives consolidation and subsequent oxidation of organic soils, leading to substantial amounts of subsidence in rural areas (Van Asselen et al., 2009). Additionally, the extraction of natural resources such as oil, gas and groundwater can induce significant (deep-seated) subsidence in both urban and rural areas (Galloway & Burbey, 2011). Observed subsidence rates in coastal megacities are in the range of 0.006 - 0.1 m/yr (Erkens et al., 2015), locally surpassing the impact of eustatic sea level rise (Erkens & Sutanudjaja, 2015). Especially many large cities in Asia are rapidly sinking due to the effect of anthropogenic land subsidence. In China alone, more than fifty cities are affected by subsidence (Xue et al., 2005), a mean cumulative subsidence of 4.25 m was observed in Tokyo in the period from 1900 to 1975 (Kaneko & Toyota, 2011) and the Mekong river delta, hosting large cities as Ho Chi Min City, is sinking with rates up to 0.04 m/yr (Erban et al., 2014). Consequently, densely populated delta regions are becoming increasingly vulnerable to floods, salinization and land loss (Nicholls et al., 2007; Erkens et al., 2015). Moreover, land subsidence is responsible for significant economic losses by damage to (natural) constructions. The damage associated with subsidence worldwide is estimated at billions of dollars annually (Erkens et al., 2015).

Groundwater extractions to support the globally increasing fresh water demands for industrial, domestic and agricultural use, led to widespread declining hydraulic head levels, which induced significant land subsidence in many large delta cities (Galloway & Burbey, 2011; Erkens et al., 2015). Figure 1.1 shows the reported areas of groundwater extraction-induced land subsidence, clearly demonstrating the global scale of this type of land subsidence (Gambolati & Teatini, 2015).

Predictive land subsidence models could be used to get insights in (future) land subsidence, identify future subsiding areas under predicted socio-economic development and test the effect of remedial measures to limit additional subsidence (Erkens et al., 2015; Erkens & Sutanudjaja, 2015). Currently, land subsidence model studies are often performed at a
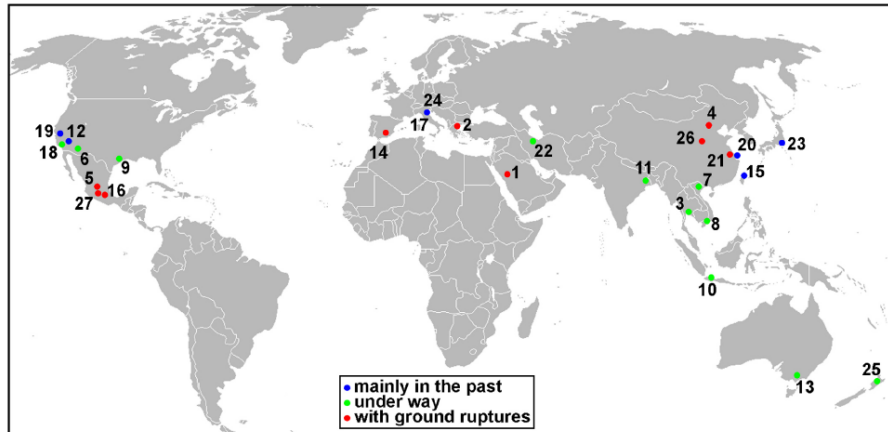
FIGURE 1.1: Reported locations of land subsidence accociated to groundwater overdraft
(Gambolati & Teatini, 2015).

small scale and biased towards well-studied areas such as Europe (e.g. Gambolati et al.
(1974)), North America (e.g. Tolman & Poland (1940)) and more recently also China (e.g.
Xue et al. (2005)). However, the rate and extent of subsidence induced by groundwater
extractions emphasize the need for reliable subsidence models globally, including data-
scarce areas.

Conventional land subsidence studies employ a groundwater coupled subsidence model to
simulate vertical deformation (Galloway & Burbey, 2011). These models require a geolog-
ical schematization and parameterization of the corresponding hydraulic and geotechnical
properties. These properties are of utmost importance and should be reliably identified to
make accurate land subsidence predictions (Gambolati & Teatini, 2015). However, often
generalizations and (empirical) approximations are adopted instead, as for many areas the
quality and quantity of these data limited. Consequently, land subsidence model predic-
tions are governed by high uncertainties and may not be sufficiently reliable to support
decision-makers (Gambolati & Teatini, 2015). The uncertainty that arises due to the lack
of knowledge about the actual properties of the study area, is referred to as epistemic
uncertainty. Epistemic uncertainty has two components: parametric and structural uncer-
tainty. The former reflects the partial knowledge about appropriate parameters and the
latter refers to uncertainty regarding the geological schematization (Turnadge et al., 2018).

Previous studies on the impact of epistemic uncertainty have mainly focused on ground-
water models. These studies showed that the dominant source of epistemic uncertainty
depends on the application of the groundwater model (Højberg & Refsgaard, 2005). Seen
the nature of subsidence models, which rely strongly on simulated drawdown, accurate
hydraulic head predictions are required to make reasonable land subsidence predictions
(Gambolati et al., 1974). Multiple studies demonstrated that hydraulic head predictions
are very sensitive to the hydraulic conductivity, a key hydraulic parameter that determines
the ease of the flow in groundwater systems (e.g. Gambolati et al. (1974); Turnadge et al.
(2018)). Moreover, the geological schematization influences hydraulic head predictions as
it controls the interconnectivity of hydrogeological layers (Martin & Frind, 1998) and de-
termines the spatial distribution of compressible material (Erkens et al., 2015). How the

uncertainty in these hydrogeological model components propagate exactly into land subsidence models and relate to uncertainty in geotechnical parameterization remains unclear. Hence, in order to make predictive regional land subsidence models globally - including data-scarce areas -, a basic understanding of the model sensitivity to both parametric and structural uncertainties is required.

1.2   Objective

The objective of this study is to make a first assessment of the sensitivity of land subsidence model predictions to epistemic uncertainty in the geological schematization and the corresponding parameterization of hydraulic conductivity and geotechnical parameters.

1.3   Research questions

The objective will be addressed by means of a case study of groundwater extraction-induced subsidence in the Greater New Orleans area and answering the following research questions:

1. How does uncertainty in the hydraulic conductivity contribute to uncertainty in the hydraulic head predictions and propagate in the land subsidence simulations?

2. How does uncertainty in the geological schematization contribute to uncertainty in the hydraulic head predictions and propagate in the land subsidence simulations?

3. How does uncertainty in the geotechnical parameterization of the NEN-Bjerrum model contribute to uncertainty land subsidence simulations?

4. Given the uncertainties in the subsidence signal, how vulnerable is the New Orleans aquifer system to land subsidence driven by the reported groundwater extractions over the last century?

1.4   Approach

This study selected the Greater New Orleans as research site, as the hydrogeological conditions of this area are reasonably well described (Rollo, 1966; Dial & Sumner, 1989; Prakken, 2009). Moreover, New Orleans is dealing with significant subsidence from various sources (Yuill et al., 2009). Recent studies have related a significant component of the observed subsidence to deep industrial groundwater extractions in urban New Orleans (Dokka, 2011; Jones et al., 2016). A conceptual hydrogeological model of the New Orleans aquifer system was constructed to serve as base for the sensitivity analysis. Land subsidence is simulated using the NEN-Bjerrum model. The utilisation of the NEN-Bjerrum viscoelastic model to calculate regional land subsidence induced by groundwater extractions was recently introduced by Bakr (2015), as this model accounts for deformation by creep. The compressibility of hydrogeological layers is defined by four geotechnical parameters: the recompression ratio (RR), the compression ratio (CR), the secondary compression ratio (C_α) and the overconsolidation ratio (OCR)).

This study assesses the sensitivity of both hydraulic head predictions and subsequent land subsidence calculations to the uncertainty in the hydraulic conductivity, geological schematization and all four geotechnical parameterization based on three criteria: magnitude, spatial extent and timing of drawdown and land subsidence. These criteria are selected as they cover the important aspects of potential impact of land subsidence. To do so, the hydrogeological model and subsidence calculations were decoupled to investigate how the uncertainty in hydraulic head predictions propagates into the subsequent land subsidence calculations.

The outline of this thesis is as follows: the basic processes and principles that are required to understand this thesis are explained in Chapter 2. Chapter 3 provides a more detailed description of the Greater New Orleans area and the observed land subsidence. Chapter 4 explains the model design, data acquisition and the proposed sensitivity analysis. In Chapter 5 the model results are analysed and partly validated. Subsequently, Chapter 6 starts by validating modelled land subsidence using existing literature and discusses the results of the sensitivity analysis. Finally, the conclusions that can be drawn from this study are summarized at Chapter 7.

2 Literature Review

2.1 Land subsidence induced by groundwater extractions

The mechanisms of compaction of confined unconsolidated aquifer systems in response to hydraulic head decline were unraveled by a series of model, field and laboratory studies carried out in the first half of the 20th century (Terzaghi, 1925; Meinzer, 1928; Jacob, 1940). Terzaghi (1925) related pore pressure and geostatic load (total overburden load) to internal grain-to-grain stresses by the principle of effective stress:

$$\sigma' = \sigma - u \tag{2.1}$$

- σ': effective or intergranular stress, (M L^{-1} T^{-2});

- σ: geostatic stress (the load of overlying saturated and unsaturated sediments and water), (M L^{-1} T^{-2});

- u: pore pressure of water in the sedimentary matrix, (M L^{-1} T^{-2}).

In undisturbed confined systems the total geostatic load (σ) acting on the aquifer system is supported by the pore pressure (u) and the effective vertical and horizontal intergranular stresses (σ'). The extraction of groundwater disturbs the balancing forces, as it lowers the porewater pressure. Consequently, in a confined system this induces an increase in effective stress, which forces the grains to rearrange and pack more tightly (Poland & Davis, 1969). Sediment compaction following a reduction in porewater pressure due to groundwater extractions is referred to as primary consolidation and was first observed by Meinzer (1928).

Jacob (1940) found that primary consolidation is different for coarse-grained aquifers and fine-grained aquitards, although it involves similar mechanisms. Figure 2.1 schematically depicts the primary stage of consolidation for both an aquifer and aquitard. In a pumped aquifer the reduction of porewater pressure and subsequent increase in effective stress occurs rapidly. Consequently, deformation of the aquifer is fast and primarily of limited recoverable elastic origin (Galloway & Burbey, 2011).

In contrast, as shown by Figure 2.1, deformation of aquitards may occur over prolonged periods and is not limited to the duration of groundwater extraction. The dissipation of excess porewater pressure in low-permeable aquitards in response to groundwater extractions in an adjacent aquifer is strongly time-dependent. Hence, the effective stress in

aquitards increases as rapidly as the excess porewater pressure can dissipate towards an hydrostatic equilibrium with the adjacent aquifer. This time-dependent process is referred to as hydrodynamic delay. Subsequent deformation of relatively compressible aquitards generally comprises significant non-recoverable deformation, but depends on the stress history of the aquitard (Jacob, 1940; Riley, 1969). The previous maximum effective stress that an aquifer system has sustained in the (geological) history determines the present compressiblity of an aquifer system (Riley, 1969). The maximum historical effective stress is called preconsolidation stress. An aquifer system is overconsolidated, if the stress enforced on the skeleton is smaller than the preconsolidation stress and any deformation is of elastic origin. In contrast, once the preconsolidation stress is exceeded, deformation is irreversible, as the sediments undergo rearrangement towards a configuration that is more stable at higher stresses (Riley, 1969).
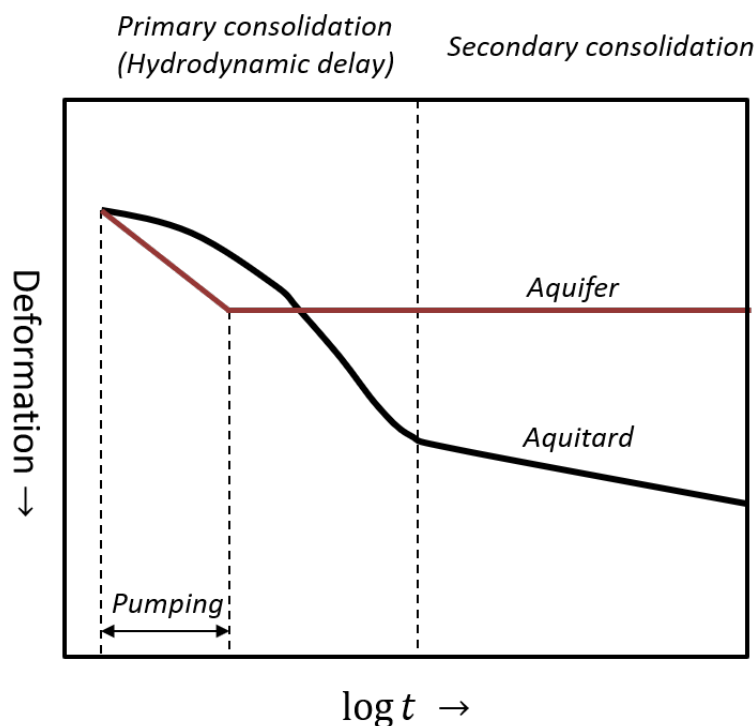
FIGURE 2.1: Schematically representation of different stages of consolidation for aquifer (red) and aquitard (black), adapted from Kooi et al. (2018).

As shown by Figure 2.1 deformation of fine-grained aquitards may continue after dissipation of the excess porewater pressure. This behaviour is known as secondary consolidation and comprises deformation by viscous behaviour or creep. Such viscous deformation is only observed in fine grained or organic sediments (Mesri et al., 1973). The physical mechanisms of deformation by creep are poorly understood, but it may involve rearrangement of water and clay particles at a molecular level (Kooi et al., 2018). Although the understanding of the physical processes is still lacking, deformation by creep is well incorporated in empirical methods (Kooi et al., 2018).

As demonstrated in Figure 2.1, the effect of viscous deformation appears after the phase of primary consolidation, which implies that creep occurs (also) for a constant effective stress. Creep rates reduce with time for a constant effective stress, while the preconsolidation stress

increases with time as a result of the ongoing viscous deformation (Taylor & Merchant, 1940). Hence, fine-grained sediments become more overconsolidated with time, which is called ageing (Bjerrum, 1967). Deformation by creep is not limited to the phase of secondary consolidation, but its effects may be limited relative to deformation induced by the increase in effective stress. Currently creep is widely applied in geotechnical engineering studies to load-driven subsidence, but the role of creep in deformation of deeper and aged aquifer systems is not yet well understood (Kooi et al., 2018).

2.2 Model principles and equations

2.2.1 Groundwater flow

IMOD employs the three dimensional finite difference groundwater flow model, which was developed by the USGS in the early 1980's as MODFLOW (McDonald & Harbaugh, 1988). This model combines Darcy's Law and the principle of conservation of mass to simulate hydraulic head in a three dimensional grid network. The core mathematical model of MODFLOW describes three dimensional movement of groundwater of constant density through porous media by the following partial-differential equation (Rushton & Redshaw, 1979):

$$\frac{\partial}{\partial x}\left(k_x \frac{\partial h}{\partial x}\right) + \frac{\partial}{\partial y}\left(k_y \frac{\partial h}{\partial y}\right) + \frac{\partial}{\partial z}\left(k_z \frac{\partial h}{\partial z}\right) - W = S_s \frac{\partial h}{\partial t} \tag{2.2}$$

- h: hydraulic head, (L);

- W: volumetric flux which represents sources and sinks of water, (L^{-1});

- t: time, (T).

- S$_S$, is the specific storage of the porous material (L^{-1});

- K$_x$, K$_y$ & K$_z$: hydraulic conductivity's along the x,y and z-direction respectively, (L/T);

In this equation the hydraulic conductivity (K) and specific storage (S$_s$) are related to the properties of the fluid and porous medium that may be both functions of space. The hydraulic conductivity is a measure of the ease with which a structure can transmit water. Systems with a high hydraulic conductivity transmit water more easily than structures with a low conductivity. The specific storage relates the amount of water that is expelled from the porous medium to a decline in hydraulic head (Fitts, 2011)

2.2.2 NEN-Bjerrum isotache model

Conventional land subsidence models are either based on the poroelastic consolidation theory of Biot (1941) or the groundwater flow theory of Jacob (1940) (Galloway & Burbey, 2011). Both models use the principle of effective stress of Terzaghi (1925) to relate fluid

flow and sedimentary matrix deformation. Although the approach of Biot is more sophisticated, as it describes the 3D displacement of the aquifer system instead of only vertical deformation (Galloway & Burbey, 2011), the approach of Jacob is more widely applied as it comprises a more groundwater-focused approach. This model decomposes deformation in an elastic and inelastic component, but neglects potential deformation by creep in aquitards, see section 2.1.

In contrast, this study employs the NEN-Bjerrum model that computes vertical viscoelastic deformation. Bjerrum was the first to notice that creep rate depends on both overconsolidation ratio and age, but Den Haan (1994) has developed a mathematical formulation for this model. Viscoelastic modelling is predominantly applied in field of geotechnical engineering and knows limited applications in the study of regional land subsidence due to groundwater extractions (Bakr, 2015; Kooi & Yuherdha, 2018; Minderhoud et al., 2017). However, these studies have shown to have the potential to better grasp the deformation behaviour of clayey aquitards (Bakr, 2015).

The model computes linear strain by decomposing it in a direct elastic contribution (ε_e) and a time-dependent viscous contribution (ε_{cr}). Elastic deformation is determined by the recompression ratio (RR) and mathematically defined as:

$$\varepsilon_{e,t} = RRlog\left(\frac{\sigma'_t}{\sigma'_0}\right) \tag{2.3}$$

- σ'_t, is the effective stress at time t, (M L^{-1} T^{-2});

- σ'_0, is the initial effective stress at the beginning of the simulation, (M L^{-1} T^{-2}).

$\varepsilon_{e,t}$, is the amount of direct elastic strain at time t. The effective stress is determined for every time step derived from hydraulic head changes.

The transient viscous component is defined by three compression parameters: the recompression ratio (RR), the compression ratio (CR) and the coefficient of secondary compression (C_α). The viscous component is computed in the following way:

$$\varepsilon_{cr,t} = (CR - RR)log\left(\frac{\sigma'_t}{\sigma'_p}\right) + C_\alpha log\left(\frac{\tau}{\tau_{ref}}\right) \tag{2.4}$$

- σ_p': initial pre-consolidation stress, (M L^{-1} T^{-2});

- τ: intrinsic time, (T).

$\varepsilon_{cr,t}$, is composed out of two terms that together define the viscous strain at time t. If C_α approaches zero, the creep component within the viscous component can be ignored and the NEN-Bjerrum model approaches an elastoplastic model. The concept of intrinsic

time was suggested by Den Haan (1994) building on the work of others. The intrinsic time accounts for the time-dependent creep rate, by relating each rate of strain to an equivalent time based on the geotechnical parameters and the preconsolidation stress. The intrinsic time is defined in the following way:

$$\tau = \tau_{ref} OCR^{\frac{CR-RR}{C_\alpha}} \tag{2.5}$$

- τ_{ref}: is the reference intrinsic time, 1 day;

- OCR: the overconsolidation, which is used to indirectly define the preconsolidation stress, using the ratio of the preconsolidation stress over the effective stress, (-):

$$OCR = \frac{\sigma'_p}{\sigma'_t} \tag{2.6}$$

Finally, the total strain is determined, as the sum of the two components:

$$\varepsilon = \varepsilon_e + \varepsilon_{cr} \tag{2.7}$$

Vertical strain is calculated every time step for every cell as a function of the effective stress, which is derived from solely hydraulic head dynamics. The amount of deformation depends on the original thickness of the layer (m_0) and is computed the following way:

$$\Delta m = \varepsilon \cdot m_0 \tag{2.8}$$

The NEN-Bjerrum model accounts for a source term of groundwater, Q_{creep}, that is released due to the inelastic deformation. However, this hydrogeological feedback mechanism of the NEN-Bjerrum model was disregarded, as this study separately assessed the groundwater dynamics and subsequent subsidence calculations.

2.3 Epistemic uncertainty

Hydrogeological systems are influenced by hydrological and meteorological conditions, geological structure, topography and human activities (Wu & Zeng, 2013). In order to capture such systems in a numerical simulation, the following steps are involved: conceptualization of the hydrogeological framework, defining model parameters and determination of initial/boundary conditions (Sun et al., 2012). The model predictions rely on how well the hydrogeological system is represented by the model. Prediction uncertainty due to a lack of knowledge of the system is referred to as epistemic uncertainty and has two components: parametric and structural uncertainty (see Figure 2.2).

Existing literature mainly focuses on the influence of epistemic uncertainties on groundwater models. Limited research has been carried out on how these uncertainties propagate

into land subsidence predictions. Since land subsidence predictions rely strongly on the hydraulic head dynamics (Minderhoud et al., 2017), relevant literature of the sensitivity of hydraulic head predictions to parametric and structural uncertainties is discussed in this section. Note that these studies may reflect regional and case specific findings.

2.3.1 Parametric uncertainties

The hydraulic conductivity is often recognized as most dominant hydraulic property (Carrera et al., 2005). The effect of hydraulic conductivity on simulated drawdown is illustrated by the simple but idealized Theis's solution (Theis, 1935), that inversely relates drawdown to hydraulic conductivity. Consequently, high hydraulic conductivity values correspond to limited drawdown and low hydraulic conductivity values correspond to more pronounced drawdown. However, as aquifer systems comprise of interconnecting aquifers and aquitards, the hydraulic conductivity of different hydrogeological units may affect the hydraulic head predictions of individual hydrogeological layers.

The hydraulic conductivity is strongly correlated to grain size: the hydraulic conductivity is generally high in coarse-grained aquifers and low in fine-grained aquitards (Fitts, 2011). Moreover, the subsurface sediments may have an anisotropic hydraulic conductivity distribution due to heterogeneities in the sedimentary stratigraphy: often the vertical hydraulic conductivity is significantly smaller that the horizontal hydraulic conductivity (Fitts, 2011). Hence, measured hydraulic conductivity values have a limited spatial coverage and may deviate from the large-scale averages. Consequently, the results of hydrogeological models based on solely measured hydraulic conductivity values, may not be able to reproduce observed hydraulic head distributions. Therefore inverse calibration using other measurements (e.g. hydraulic head, tracer concentrations) is often applied to adjust initial hydraulic conductivity values and fit observed hydraulic head levels (Kowalsky et al., 2012). Depending on the purpose of modelling, such calibration procedures may compensate for both erroneous hydraulic parameters and geological schematization (Refsgaard et al., 2012). However, also calibrated hydraulic conductivity values may still be governed by a significant uncertainty caused by uncertainty in observations used as calibration targets (Fitts, 2011).

The hydraulic conductivity of aquifers and aquitards may differently affect model predictions. Turnadge et al. (2018) determined that the hydraulic conductivity of aquifers predominantly influence the drawdown in an aquifer itself, while the vertical hydraulic conductivity of aquitards determine largely the recharge to adjacent aquifers (Cherry et al., 2004; Turnadge et al., 2018). Historically seen, mainly the characterisation of aquifers for water supply received attention (Turnadge et al., 2018). Aquitards were represented very simplified as 'no-flow barriers' or 'leaking layers' (Zhuang et al., 2015). The importance of aquitards is now increasingly recognized in many aspects, including their importance in land subsidence models (Poland & Davis, 1969). Improved characterization of aquitards in groundwater models have shown that aquitards affect the timing of maximum drawdown in adjacent aquifers (Turnadge et al., 2018). This may be very important to well account for the hydrodynamic delay of primary consolidation in land subsidence models.

Several studies have also identified recharge as a dominant parameter influencing the model predictions (Mishra et al., 2009; Gedeon & Mallants, 2012). However, these studies considered often contaminant transport. Zeng et al. (2012) found that the variance of modelled head is more dependent on the hydraulic parameters, while the mean of the modelled head is more affected by the boundary conditions including recharge. As land subsidence predictions rely especially on the relative hydraulic head dynamics, recharge is not expected to be a determining factor.

2.3.2 Structural uncertainties

As the geological structure controls the continuity and interconnectivity of different geological units, it has a dominant role in controlling groundwater flow (Martin & Frind, 1998). Hence, uncertainties governing the geological schematization can induce a dominant source of uncertainty in groundwater models (Refsgaard et al., 2012). Uncertainty with respect to the geological schematization may stem from different factors: for example due to incomplete information about the reality, alternative geological interpretations or alternative model choices with respect to parameterization or layer discretization (Refsgaard et al., 2012). Generally, there is accounted for these uncertainty by assessing multiple (alternative) geological schematizations, adjusting the corresponding hydraulic parameterization or by approaching the geological schematization stochastically (Refsgaard et al., 2012; Ye et al., 2010).
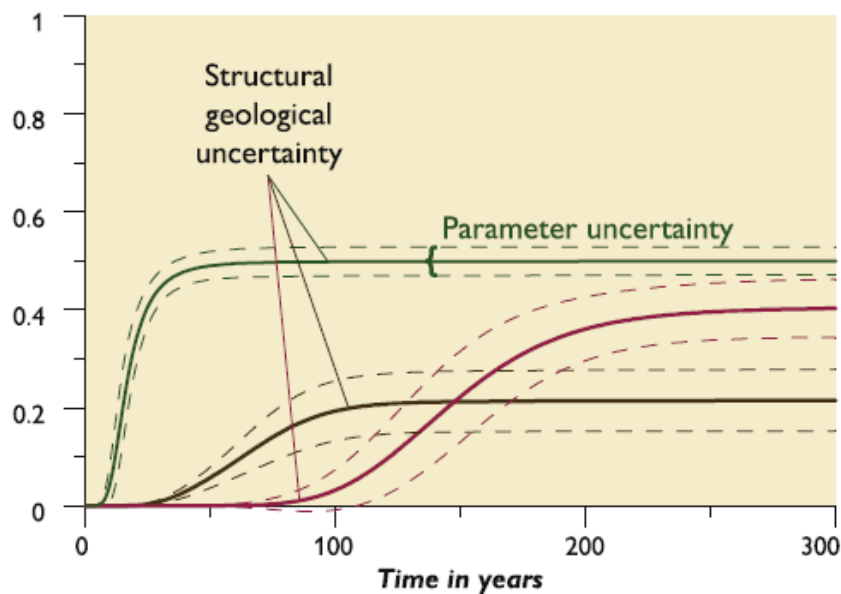
FIGURE 2.2: Simulated contaminant concentration breakthrough curves for three different models with different geological interpretations. The normalized concentration is shown at the y-axis. The prediction uncertainty due to parameter uncertainty is indicated with dashed lines (after (Højberg & Refsgaard, 2005)).

Højberg & Refsgaard (2005) analysed the importance of parameter uncertainty versus structural uncertainty by constructing three alternative groundwater models. All three groundwater models demonstrated a similar performance with respect the hydraulic head

predictions after model calibration of hydraulic parameters. Hence, parametric uncertainty showed to be the dominating source of uncertainty for the simulation of hydraulic head levels. In contrast, the structural uncertainty became much more important when the three groundwater models where used to model chemical transport and groundwater recharge (Højberg & Refsgaard, 2005). Figure 2.2 shows the concentration breakthrough curves at the same location for the three groundwater models (solid lines). The figure clearly demonstrates that the structural geological uncertainty dominates the prediction uncertainty. Hence, the relative importance of parametric and structural uncertainties is strongly related to the proposed application the groundwater model. Since land subsidence calculations rely predominantly on hydraulic head predictions, model calibration may significantly reduce the effect of structural uncertainty. However, the geological schematization additionally determines the distribution of compressible material depends and may accordingly affect the land subsidence predictions significantly (Erkens et al., 2015).

2.3.3 Uncertainty and sensitivity of geotechnical parameters

Due to the limited applications of the NEN-Bjerrum model in regional land subsidence studies, not much work has been carried out on the sensitivity and uncertainty of the land subsidence model predictions to the four geotechnical parameters: the compression parameter (CR), the recompression parameter (RR), the secondary compression parameter (C_α) and the overconsolidation ration (OCR). Data to well constrain these parameters at the scale of a regional aquifer-system is often very limited, as geotechnical data is mainly determined for the purpose of shallow load-driven compaction calculations. Previous regional land subsidence studies adopted, apart from (limited) local sample measurements, general relations among the compression parameters to find parameter values (Minderhoud et al., 2017; Bakr, 2015). Such natural relations exist among the compression and recompression ratio (Gunduz & Arman, 2007) and the compression and secondary compression ratio (Kooi et al., 2018).

Previous studies showed, that the NEN-Bjerrum model is very sensitive to the overconsolidation ratio (OCR) and can thus effectively be used to calibrate the model against observed land subsidence (Kooi et al., 2018). For example, Minderhoud et al. (2017), that used an equivalent land subsidence model (abc-model) to simulate subsidence in the Mekong delta, used the OCR to calibrate the land subsidence model based on land subsidence observations derived from InSAR data. They found the OCR to be a very sensitive parameter reflecting the strength of the sediments. A least conservative model with an OCR of 1.45 was found corresponding to an average subsidence rate of 1.8 cm/yr, while the most conservative model with an OCR of 1.75 corresponded to an average subsidence rate of only 0.5 cm/yr. However, too low values for the overconsolidation ratio (OCR) should be avoided, as this may may result in the simulation of unrealistically high background deformation by creep (Kooi et al., 2018).

Hence, natural relations among the geotechnical parameters and model restrictions, limit the number of possible geotechnical parameter combinations. Moreover, land subsidence models can be effectively calibrated using land subsidence observations. However, in absence of land subsidence observations, an uncertain geotechnical parameterization may significantly affect land subsidence model predictions.

3 Research Area

3.1 The Greater New Orleans area

The Greater New Orleans area constitutes the research area of this study and is delineated in Figure 3.1. The study area is located in coastal Louisiana on the Holocene deltaic plain of the Mississippi River. The study area encompasses the city of New Orleans, which forms a major economic and commercial hub for the broader Gulf Coast region (Cutter & Emrich, 2006). With respect to the vertical extent, the study area comprises the New Orleans aquifer system. This aquifer system comprises six aquifers separated by intervening aquitards of Holocene and Pleistocene age and reaches to a depth of about 300 m below New Orleans.
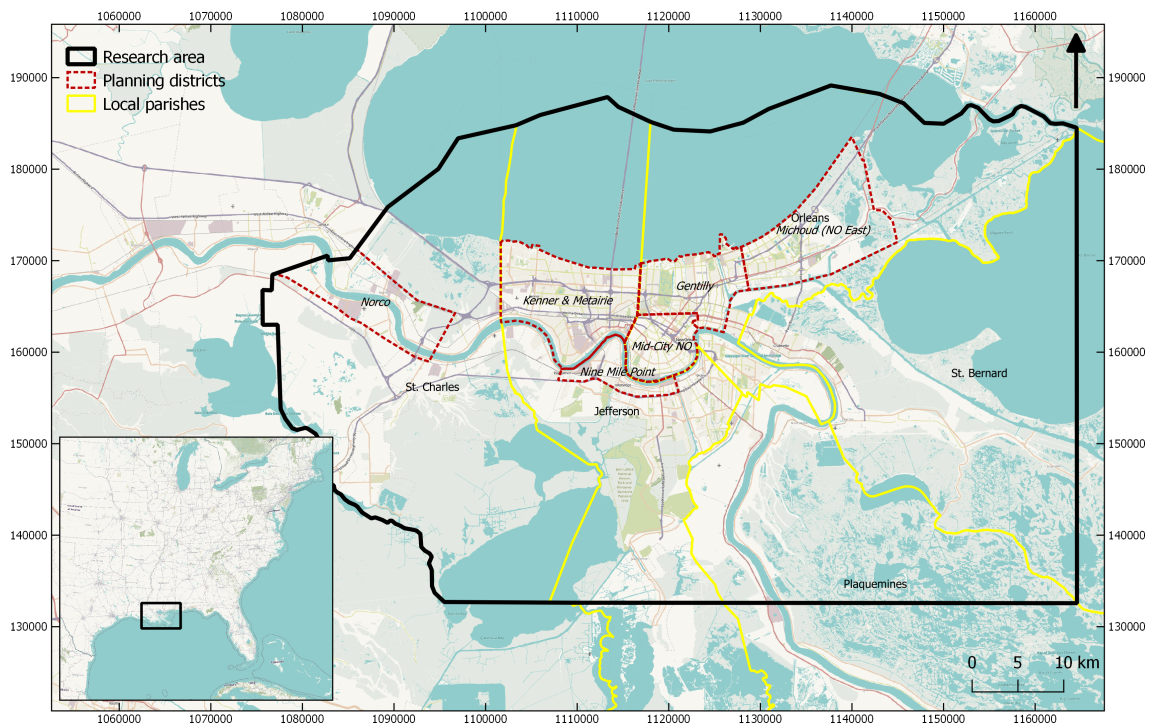
FIGURE 3.1: Location of the study area. In Yellow the relevant Parishes (Louisisian Geographic Information Center) and in red relevant planning districts (gis.nola.gov) are indicated.

The study area follows the boundaries of relevant parishes, which is a local administrative division, as groundwater data (i.e. hydraulic head observations, groundwater extractions) is often reported by parish. The study area includes the Saint Charles, northern part of Jefferson, Orleans, northern part of Plaquemines and the western part of Saint Bernard parishes (yellow in Figure 3.1). Additionally, planning districts (red) are indicated in Figure 3.1, which are used to spatially distinguish between regions in the study area.

3.2 Geological setting

The study area consists of a sedimentary deposits that were delivered by the Mississippi River and its tributaries during the Pleistocene and Holocene respectively. The Pleistocene deposits in the study area are composed of southward dipping sedimentary sequences, each containing a basal unit of coarse sediments and an upper unit of finer sediments (McFarlan Jr & LeRoy, 1988). These sedimentary sequences reflect the shifting depositional environments in the study area. During the Pleistocene, periods of continental glaciation and deglaciation and the equivalent changes in sea level were the dominant forcing mechanisms with respect to sedimentation and erosion (Coleman & Roberts, 1988). During sea level low-stands the river systems advanced to the edge of the continental shelf, while at the study area these periods were characterized by entrenchment of rivers and oxidation, consolidation and erosion of the surface deposits due to long term exposure (Kolb & Van Lopik, 1966; McFarlan Jr & LeRoy, 1988). After a glacial maximum, sea level rise and increased melt-water discharge caused sedimentation of coarse sands and silts in the study area (McFarlan Jr & LeRoy, 1988). Subsequent ongoing sea level rise caused the depositional environments to shift landwards covering the coarse sediments by clays and silts (McFarlan Jr & LeRoy, 1988).
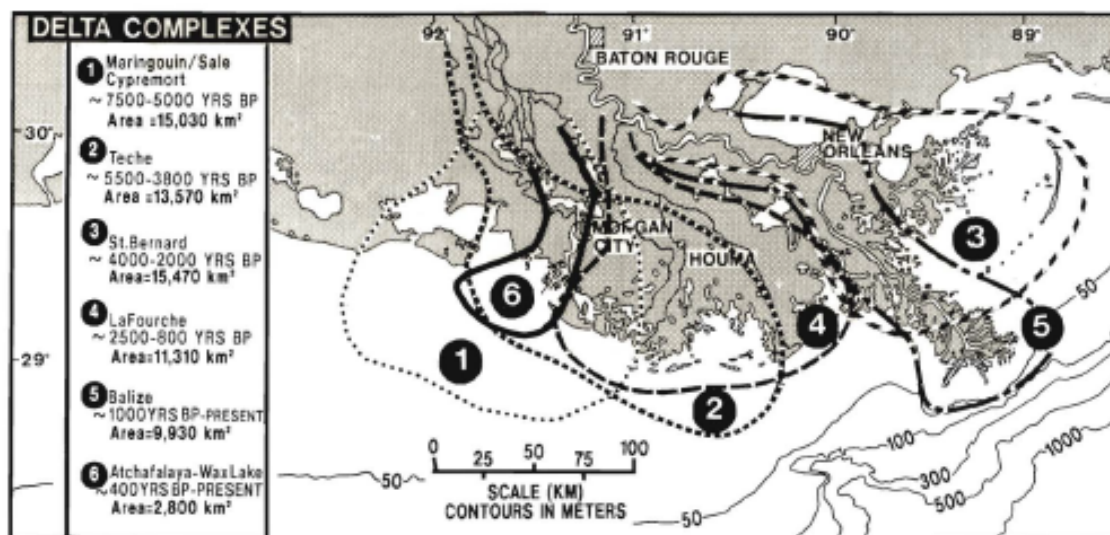
FIGURE 3.2: Multiple deltaic lobe complexes of the Mississppi Deltaic Plain (Snowden et al., 1980).

After the sea level stabilized and the current sea level high stand was attained around 7500 BP (Early Holocene), the area was characterized by frequent changes in the course of the Mississippi River (Kolb & Van Lopik, 1966). This way five prominent deltaic lobe complexes were formed, creating the modern deltaic plain (Coleman et al., 1998). As shown by Figure 3.2, the study area is located on the Holocene deposits of the St.Bernard and Atchafalaly-WasLake deltaic complexes. These deposits are consisting of predominantly fluvial sediments ranging from sands to clays locally (Kolb & Van Lopik, 1966). The Holocene deltaic deposits continue up to north of Lake Pontchartrain.

Several processes of natural land subsidence have been identified in the study area (Yuill et al., 2009). Although, the exact contribution of individual natural subsidence processes in the study area is unclear, the activity of deep subsidence processes may explain a deviation

between modelled and observed aquifer-system compaction. Hence, this section considers briefly two important natural mechanims of deep-subsidence, which are both likely to affect deep subsidence observations in the study area: isostatic adjustment of the lithospere and tectonic activity of fault systems.

Due to basinward steepening of Pleistocene river terraces in Coastal Louisiana, a significant component of crustal movement caused by sediment loading was presumed for a long time. However, the detailed model study of Wolstencroft et al. (2014) to isostatic adjustment of the lithosphere in response to sediment loading, does not support any high subsidence rates. The model results show that rates of isostatic adjustment are unlikely to exceed 0.5 mm/yr due to solely sediment loading (Wolstencroft et al., 2014). However, the ongoing effect of forebuldge colapse after the last period of glaciation may increase this rate of basement subsidence to approximately 2 mm/yr (Wolstencroft et al., 2014).
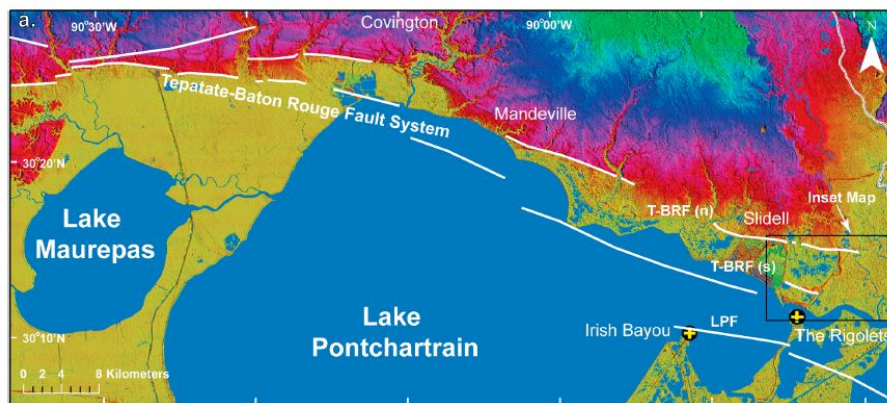
FIGURE 3.3: Location of Tepatate-Baton Rouge (T-BRF) and Lake Pontchartrain fault systems (LPF) north of New Orleans (Dokka, 2011).

Two major basin margin fault systems that border the Gulf of Mexico are identified just north of the research area, see Figure 3.3. These fault system are east-west striking normal fault systems (Dokka, 2011). The current rate and activity of these faults is topic of ongoing scientific discussion. Differential behaviour between observations provided evidence for recent activity of these faults (Dokka, 2011). However, the spatial extent and magnitude of the rates of subsidence related to these faults is unclear.

3.3 New Orleans aquifer system

The groundwater resources in the Greater New Orleans area are primarily situated in the New Orleans aquifer system (Dial & Sumner, 1989). This aquifer system forms the southern top part of the much larger and deeper (up to Miocene deposits) Southern Hill aquifer system, which covers large parts of southeastern Louisiana and western Mississippi (Chamberlain et al., 2013). The New Orleans aquifers system comprises six aquifers separated by intervening unnamed aquitards, from shallow to deep: the Mississippi River point-bar deposits, the shallow aquifers of the New Orleans area, Gramercy aquifer, Norco aquifer, Gonzales-New Orleans aquifer, and the 1,200 foot aquifer. The upper two aquifers, which were deposited during Holocene times, are relatively small and discontinuous in the study area. Therefore, these aquifers are not further considered in this study. The lower

four aquifers are the major water bearing aquifers, deposited predominantly in Pleistocene times (Dial & Sumner, 1989; Prakken, 2009). The depth and north-south orientation of these aquifers is shown by Figure 3.4. In line with the described geology (Section 3.2) the aquifer layers dip gently southward. The Holocene layer thins out towards the north, where the Pleistocene aquifers approach or even outcrop at the surface. Here, surface water can relatively easily enter the aquifer-system (Prakken, 2009).
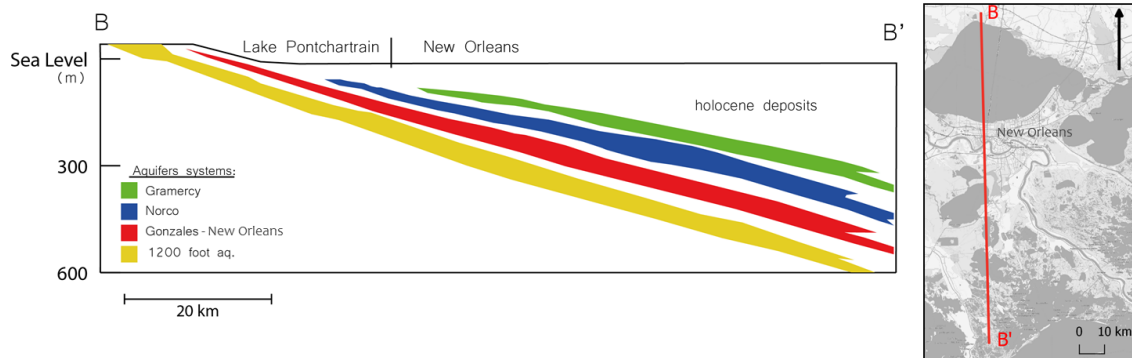
FIGURE 3.4: North-south cross-section of the deeper New Orleans aquifer system (adapted from Dial & Sumner (1989)).

Both the spatial extent and conditions of the Pleistocene aquifers were investigated by a series of reports (incl. Rollo (1966); Dial & Sumner (1989); Tomaszewski (2003); Prakken (2009)), which were carried out in relation to groundwater use. Based on these reports the following is known about the aquifers with increasing depth:

- **Gramercy**
  The Gramercy aquifer, which is absent in the northern part of the study area, progressively thickens in southward direction up to 45 m. This aquifer consists of fine to coarse sand and locally gravel and is directly located below the Holocene deposits at a depth of 60 m below the surface in New Orleans (Dial & Kilburn, 1980). Within the study area this aquifer contains only saltwater (Tomaszewski, 2003). Hence, no historical extractions of any significance are reported for this aquifer in the study area.

- **Norco**
  The Norco aquifer is most prominent in the western part of the study area and contains a significant amount of fresh water. A clay layer ranging between 3 and 25 m separates the Norco aquifer from the Gramercy aquifer. Below urban New Orleans the Norco aquifer is thin or even absent. However, where present in the study area, the thickness of the Norco aquifer ranges between 15 and 45 m at an mean depth of about 100 m below the surface. The aquifer consists of fine to coarse sands (Dial & Kilburn, 1980). Significant historical groundwater extractions from this aquifer have been reported for the Jefferson and Saint-Charles Parish. Groundwater extractions from the Norco aquifer peaked around 1965 and mainly served industrial purposes. Significant groundwater recovery of 18 m was observed in the aquifer below Saint-Charles parish since 1958 in line with the decreased groundwater extractions (White

& Prakken, 2015). Since 1996 water levels in the aquifer are stable in both the Jefferson and Saint-Charles parishes (Prakken, 2009; White & Prakken, 2015).

- **Gonzales-New Orleans**
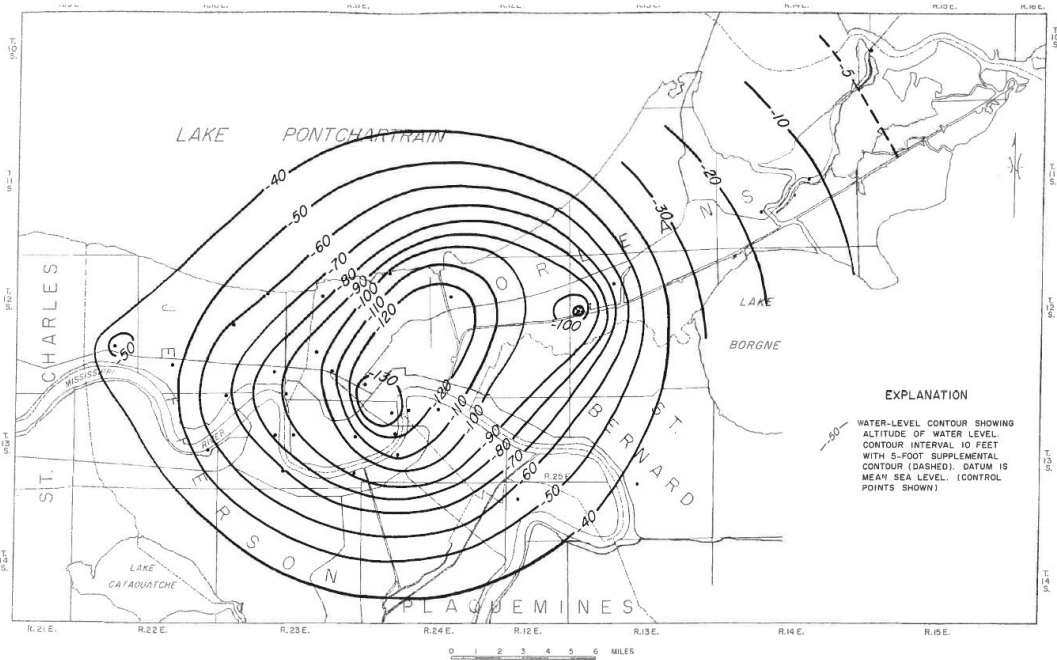 The Gonzales-New Orleans aquifer is the only aquifer that is continuous throughout the greater New Orleans area and contains a significant amount of fresh water (Tomaszewski, 2003). The Gonzales-New Orleans is separated with the Norco aquifer by an aquitard up to 60 m thick. The aquifer has an average thickness of about 60 m and is located 170 m below the surface in New Orleans. The aquifer consists of fine to medium-grained sands (Dial & Sumner, 1989). The Gonzales-NO aquifer knows the largest historical groundwater extractions in study area. Groundwater was mainly extracted for industrial purposes in the Orleans and Jefferson parish due to the low quality of the water (Rollo, 1966). The first groundwater extractions from the this aquifer date back to 1854 (Harris & Fuller, 1904). Groundwater extractions were the highest in 1970, with a total of 167 m^3/day in solely Orleans parish. These extractions reduced to 60 m^3/day in 2005 (Rollo, 1966). Both Rollo (1966) for 1963 and Prakken (2009) for 2008 produced potentiometric maps for the Gonzales-NO aquifer based on interpolations of hydraulic head observations, (Figure 3.5a & Figure 3.5b). These figures show a significant cone of depression extending over the entire research area. Comparing the figures shows that the focus of the cone shifted from Mid-city New Orleans towards Michoud (east of New Orleans) from 1963 to 2008. Figure 3.5b also indicates the locations of major groundwater extractions locations for 2007. This hydraulic head pattern is clearly dominated by the large industrial groundwater extractions at the industrial facilities at Michoud. Consistent with the trend in groundwater extractions, significant hydraulic head recovery occurred after 1970. The hydraulic head in the aquifer have risen about 18 meters south of the Mississippi River and east of New Orleans since 1970 (Prakken, 2009).

- **1,200 foot aquifer**
  The 1,200 foot aquifer is varied present in the study area, but contains predominantly saltwater (Prakken, 2009). The thickness of the aquifer ranges up to 30 m. Where present, the aquifer is separated by a significant aquitard of 45 m thick (Prakken, 2009). This aquifer constitute the lower limit of the New Orleans aquifer system. No significant historical groundwater withdrawals have been reported in this aquifer within the study area.

3.4   Land subsidence induced by groundwater extractions

Kazmann & Heath (1968) associated groundwater withdrawals with observed land subsidence for the study area already in 1968. Numerous studies have been carried out to identify the main drivers of subsidence in the Greater New Orleans area (e.g. Dokka (2006); Dixon et al. (2006); Yuill et al. (2009)). These studies show an inconsistent picture of different mechanisms of subsidence. The disagreement may stem from the fact that measurements cover different processes, which are acting at different depths and times (Jones et al., 2016). The exact contribution to land subsidence by groundwater extractions remains unclear. The studies of Dokka (2011) and Jones et al. (2016) discuss the

(a)
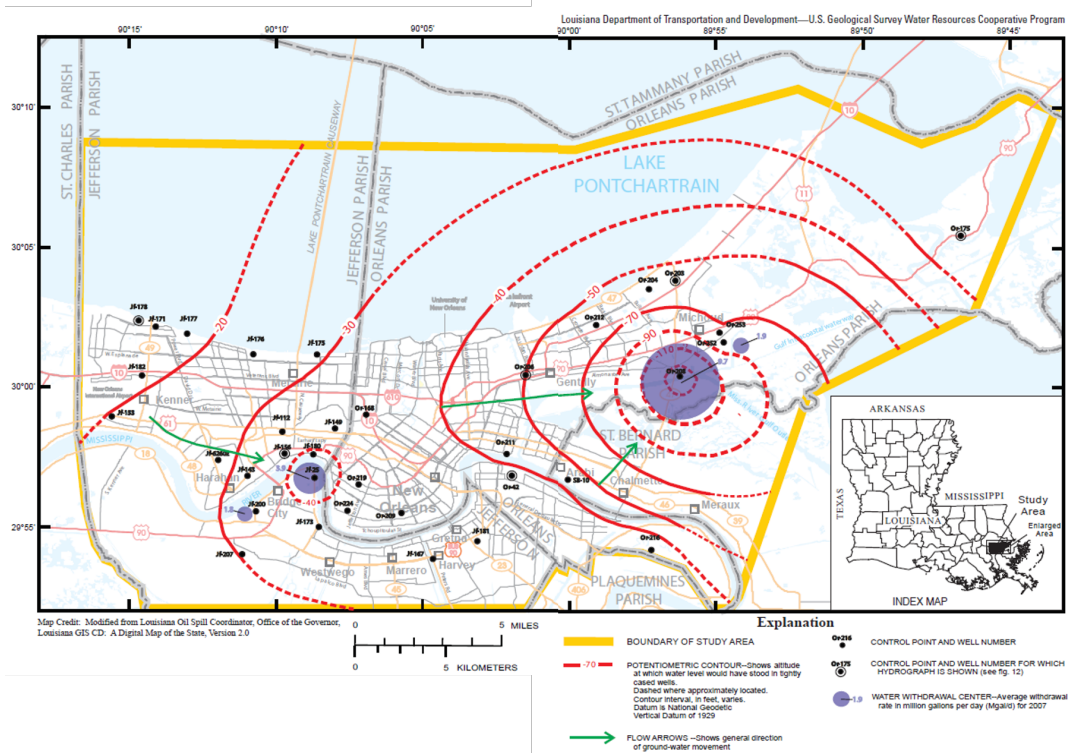
(b)

FIGURE 3.5: Potentiometric surface of the Gonzales-New Orleans aquifer for a) 1963 and b) 2008 in ft (Rollo, 1966; Prakken, 2009).

potential contribution of large industrial groundwater extractions at Michoud and Norco to land subsidence.

Dokka (2011) used geodetic levelling data and water gauge readings attached to monuments and bridges all founded at depths below the base of local Holocene deposits. This way the measurements contain no contribution of Holocene compaction. Both types of observations showed increasing subsidence rates towards the industrial facilities at Michoud, where multiple large groundwater extractions in the Gonzales-NO aquifer are reported (Section 3.3). Figure 3.6 shows the subsidence as inferred from the water level gauges. The locations of the water gauges are indicated on Figure 3.7. The subsidence signal at the Paris Road Bridge (Michoud) demonstrates clearly the highest amount of subsidence. Dokka (2011) suggested that the completion of last and largest generator at the Entergy Michoud Power Plant is reflected by the sharp increase in the subsidence signal at the Paris Road Bridge around 1967. With exception of the Rigolets bridge, the figure shows that the other more distant water gauge readings have similar subsidence signals, which slow down over time coinciding with the hydraulic head recovery. The latter supports the conclusion that these measurements contain a significant contribution of subsidence due to groundwater extractions (Dokka, 2011). The constant subsidence rate of 3.7 mm/yr at the Rigolets Bridge, as shown by the water gauge readings, may reflect the contribution of deep-seated subsidence (Dokka, 2011).
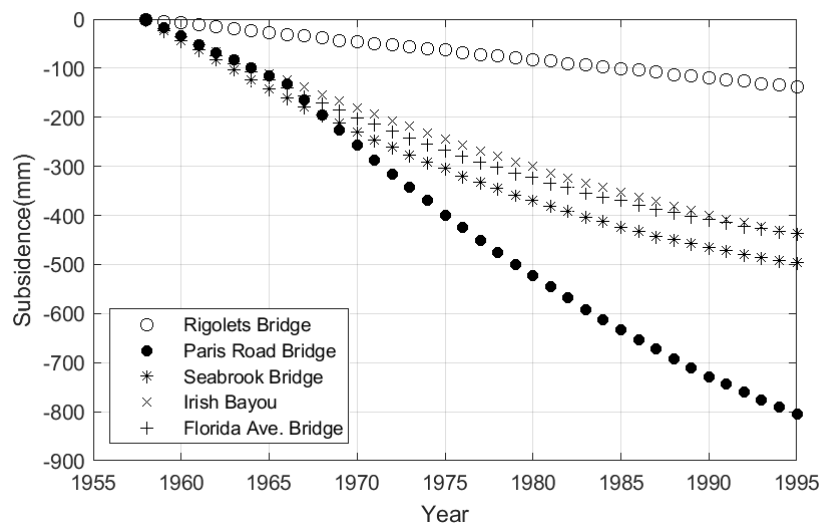
FIGURE 3.6: Subsidence histories inferred from water level gauges readings in the Greater New Orleans area (adapted from (Dokka, 2011)), see Figure 3.7 for locations of water level gauges.

The exact contribution of deep-seated subsidence in the measurements of Dokka (2011) is uncertain and may vary spatially. Geodetic levelling data of a 2000 m founded waste well at Michoud, indicated average subsidence of 9.5 mm/yr for the period of 1969 to 1995. As this measurement is below the vertical extent of the New Orleans aquifer system, the contribution of subsidence by groundwater extractions is ruled out. According to Dokka (2011), this high rate may include the contribution of subsidence by tectonic activity of the Michoud fault. The duration and spatial extent of the revival of this fault are uncertain. Its existence was supported by the InSAR data of Dixon et al. (2006) for 2002-2005, that

showed differential vertical movement between both sides of the fault. However, the InSAR study of (Jones et al., 2016) and deep GPS measurements did not find evidence for the activity of this fault in 2009-2012.
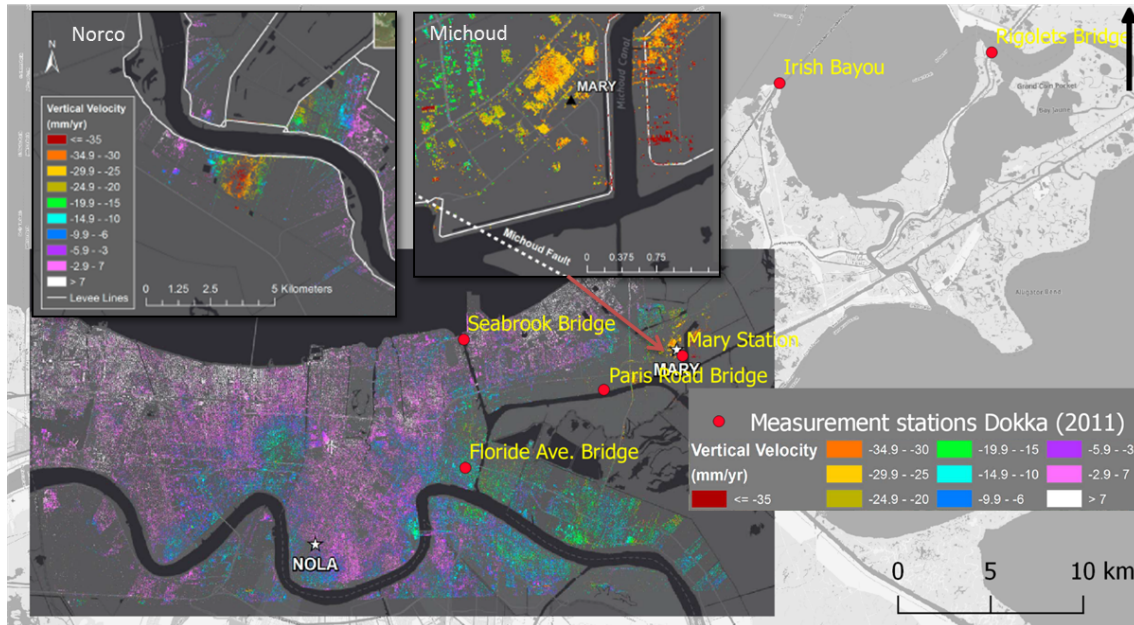
FIGURE 3.7: Overview of subsidence rates calcuated from InSAR data between 16 June 2009 and 2 July 2012 for the Greater New Orleans area. The subsidence rates at Norco and Michoud are outlined (adapted from Jones et al. (2016)). The in red indicated locations correspond to the measurement station of Dokka (2011). The inferred subsidence signals at these locations are depicted in Figure 3.6.

Jones et al. (2016) used an airborne techinque, InSAR, to derive average subsidence rates in urban New Orleans between June 2009 and July 2012. These measured rates are depicted in Figure 3.7 and reflect the activity of all subsidence mechanisms. Consistent with the findings of Dokka (2011), the figure shows a large subsidence hotspot at Michoud. Average subsidence rates of 25-30 mm/yr were found at the Michoud Entergy facility and even higher rates of 50 mm/yr were found further east at Michoud. Additionally, Jones et al. (2016) found subsidence rates up to 35 mm/yr at the chemical industry around Norco in the western part of the study area. These rates stand out with respect to measured subsidence in the rest of urban New Orleans (see Figure 3.7). Jones et al. (2016) discuss the potential contribution of subsidence induced by groundwater extractions at these locations, as they correspond well to the locations of large reported groundwater extractions from the Gonzales-NO and Norco aquifer. However, these rates are much higher than the rates found by (Dokka, 2011) and are in contradiction with the described head recovery in the Gonzales-NO and Norco aquifer.

4 Research Methods

Figure 4.1 summarizes the steps that were followed to fullfil the objective of this study. The constructed base hydrogeological model of the New Orleans aquifer system was used to perform a sensitivity analysis with respect to hydraulic conductivity (blue), geological schematization (green) and geotechnical parameterization (red). This chapter will first consider the model design and data acquisition and subsequently describe the sensitivity analysis that was carried out.
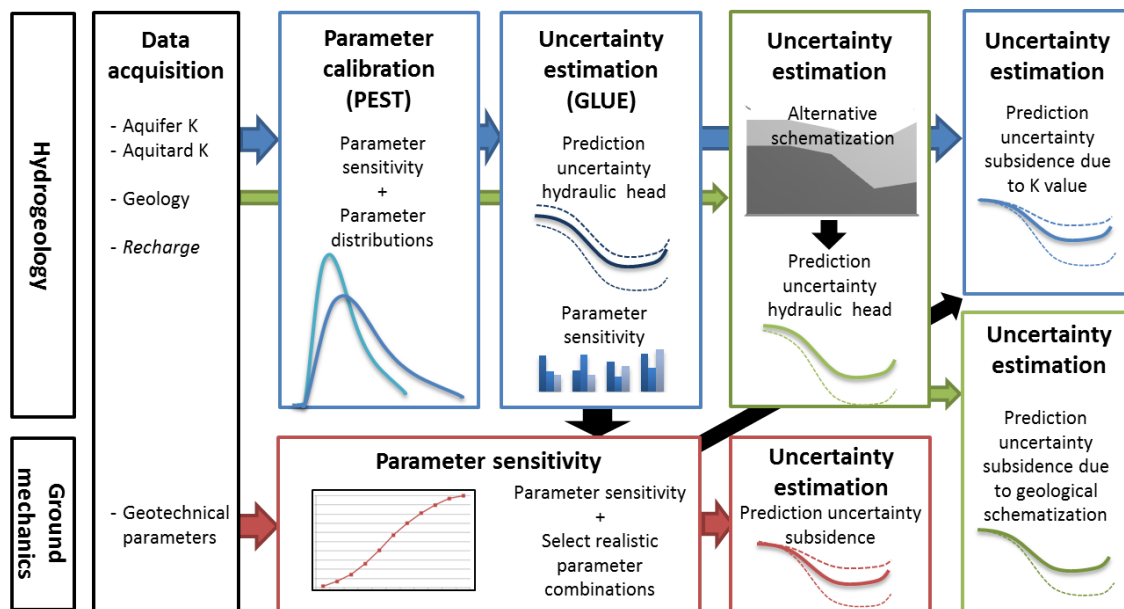
FIGURE 4.1: Flow chart of sensitivity and uncertainty analysis.

4.1 Model design and data acquisition

Vermeulen (2018) built a steady-state groundwater model of the New Orleans aquifer system in iMOD, which served as base hydrogeological model. However, significant adaptions were performed in order to be able to simulate groundwater and subsidence transiently and better grasp the hydrogeological system.

4.1.1 Model extent

The local Louisiana South NAD83 coordinate system was used to express the model domain and subsequent results. Vertical units are all set relative to NVGD29. The model domain comprises the entire extent of the New Orleans aquifer system in order to fully capture the regional groundwater dynamics. In north-south direction the model area ranges from to

the northern border of southeastern Louisiana to 50 km into the Gulf of Mexico. In east-west direction the model domain extends from Mobile Bay (Alabama state) to Lafayette. This model domain consists of 268 x 413, 1 x 1 km grid cells (see Figure 4.2), covering an area of 110,684 km². The model domain encompasses the study area that consists of the greater urban New Orleans area. As the boundaries of the model domain are sufficiently distant from the study area, the effect of extraction wells located in the study area was assumed to be limited at the model boundaries. Therefore, a no-flow boundary was used to delimit the model domain.
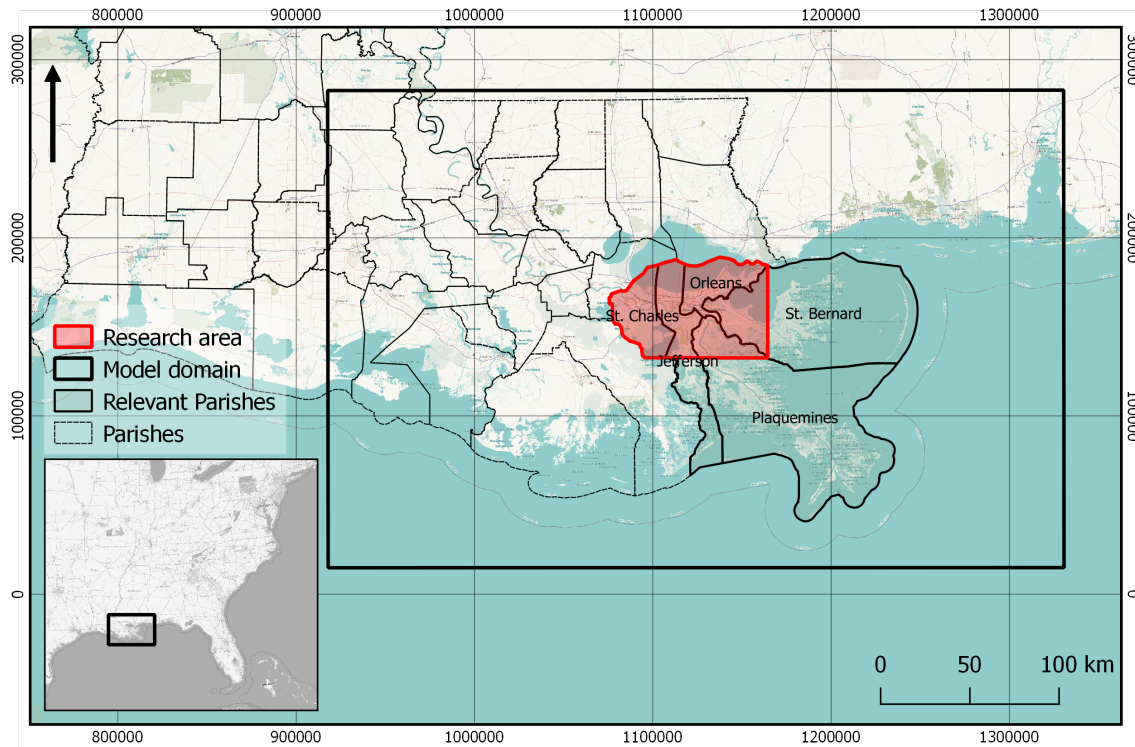
FIGURE 4.2: Delineation of the model domain (black) and study area (red). Relevant parishes, a local administrative division, are indicated in green. The shape and size of the research area is based on the boundaries of these parishes.

4.1.2 Geological schematization

A north-south orientated 2D model of the aquifer-aquitard subsurface was provided by Vermeulen (2018). This geological schematization follows largely the schematization of the aquifer system by Dial & Sumner (1989) and was slightly adapted for the purpose of this study. Since the study focuses on subsidence induced by groundwater extractions from the Pleistocene aquifers, the Holocene deposits were included as a single phreatic top layer. The underlying Pleistocene aquifer system was included as a confined system and comprises from shallow to deep the following aquifer units: Grammercy, Norco, Gonzales-New Orleans and 1,200 foot aquifer (see Section 3.3 and Figure 4.3). Similar to the geological schematization of Dial & Sumner (1989), all these aquifers are north-south continuous and isolated units, separated by unnamed aquitards. In addition, this study assumed the cross-section to be continuous in east-west direction. The surface elevation of the (Holocene) top layer was corrected using a Digital Elevation Model (DEM) obtained from NASADEM (https://earthdata.nasa.gov), to make sure that land surface was not located below the

stage of the Gulf of Mexico. This resulted in an eight layer geological schematization, representing a Holocene top layer underlain by four aquifers and three intervening aquitards.
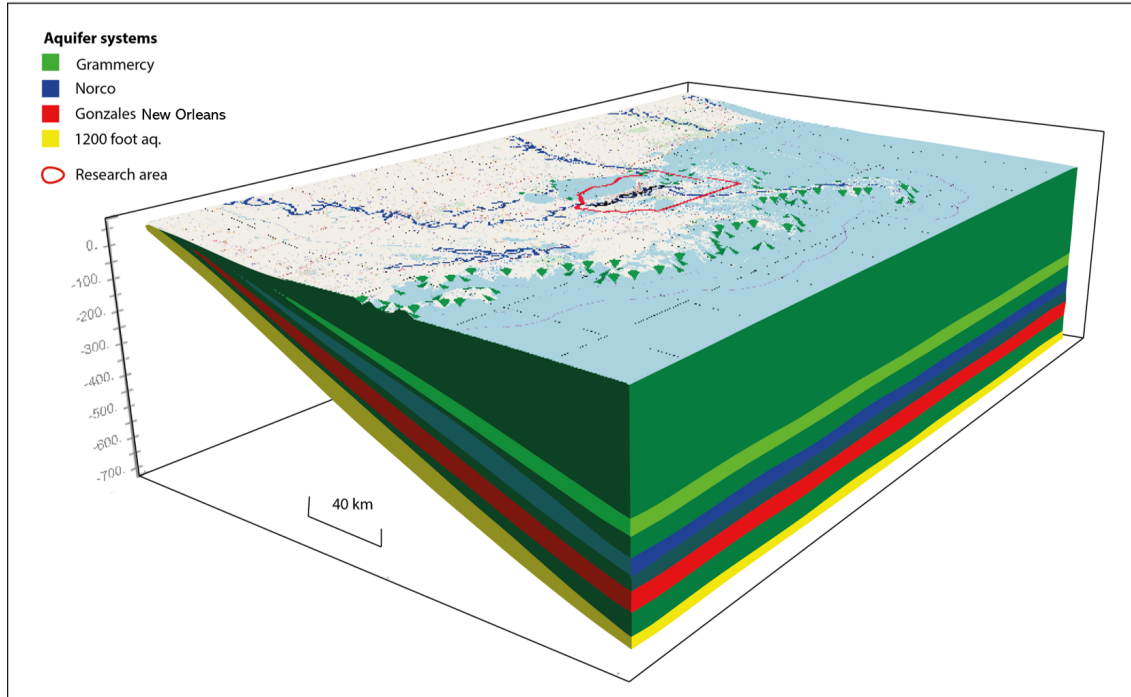
FIGURE 4.3: 3D representation of the geological schematization, which is largely based on the geological schematization of Dial & Sumner (1989). The depth and location of the Pleistocene aquifer systems are indicated. Note that the Pleistocene layers all dip towards the Gulf of Mexico and the thickness of the Holocene layer progressively increases southward.

4.1.3   Hydraulic conductivity

This study assumed both horizontal and vertical isotropy of the hydraulic conductivity for the aquifers and aquitards, as no information about anisotropy in the study area was present and to limit the options in the sensitivity analysis.

The initial parameterization of the hydraulic conductivity of the aquifers was based on the study of Dial & Sumner (1989) and Dial & Kilburn (1980), that determined aquifer properties based on previous investigations and aquifer-tests, see Table 4.1. As groundwater flow depends on transmissivity (hydraulic conductivity (k) x thickness (b)), rather than solely the hydraulic conductivity, the thickness-weighted mean of the reported hydraulic conductivity values was determined:

$$\bar{K} = \frac{\Sigma_{i=1}^{n} d_i K_i}{\Sigma_{i=1}^{n} d_i} \tag{4.1}$$

In contrast to the aquifers, information about the hydrogeological properties of the aquitards is limited. The hydraulic conductivity of the top layer was assigned a value of $3.33 \cdot 10^{-3}$ (m/d), which was based on the order of magnitude of the hydraulic conductivity for a Holocene clay layer north-west in the model domain determined by Hanor (1993). For

TABLE 4.1: Hydraulic conductivity and thickness of the aquifers. First two column are hydraulic conductivity values found based on Dial & Kilburn (1980) and Dial & Sumner (1989) respectively. The third column are the values adopted in this study.

	Dial & Kilburn (1980)		Dial & Sumner (1989)		This study
	K (m/d)	d[1](m)	K (m/d)	d[1](m)	K (m/d)
Gramercy	76.0	45.0	30.0	23.0	60.0
Norco	64.0	42.0	40.0	42.0	50.0
Gonzales-New Orleans	45.0	76.0	34.0	6.0	36.0[2]
1200 foot aq.	-	-	30	27	30

[1] Mean reported thickness.

[2] Slightly lower than thickness-weighted mean value, as initial modelling showed better model performance for lower value.

the Pleistocene aquitards the same procedure as in Dial & Sumner (1989) was employed. It was assumed that the degree of compaction of a fine-grained aquitard influences the hydraulic conductivity and that this degree of compaction increases with burial depth. A relation between porosity and burial depth of clayey sediments of Tertiary age in the Gulf of Mexico was established by Dickinson (1953). This relation was used to find porosity values for all Pleistocene aquitards, as measure of the degree of compaction. As the exact relation was not re-traceable in the work of Dickinson, an empirical relation was fitted by a simple quadratic function:

$$n = 1.193 \cdot 10^{-6} \cdot z^2 - 0.0015 \cdot z + 0.79 \tag{4.2}$$

- n is the porosity (-);

- z is burial depth in (m).

Subsequently, the porosity was converted to void ratio using Equation 4.3.

$$e = \frac{n}{1-n} \tag{4.3}$$

Subsequently, Equation 4.4 was used to relate hydraulic conductivity and void ratio (Abelev & Tsytovich, 1964) and find hydraulic conductivity values for all aquitards.

$$k = k_{ref}e^{C(e-e_{ref})} \tag{4.4}$$

- k_{ref}: hydraulic conductivity at a burial depth of 300 m, (m/d);

- C: Constant describing slope of log-transformed hydraulic conductivity versus void ratio relation, (-);

- e: void ratio, (-);

- e_{ref}: void ratio at a burial depth of 300 m, (-).

Optimized values for constants C and k_{ref} from model calibration by Dial & Sumner (1989) were adopted. Accordingly, C is 1 and k_{ref} is $3.05*10^{-5}$ (m/d).

(a)   (b)
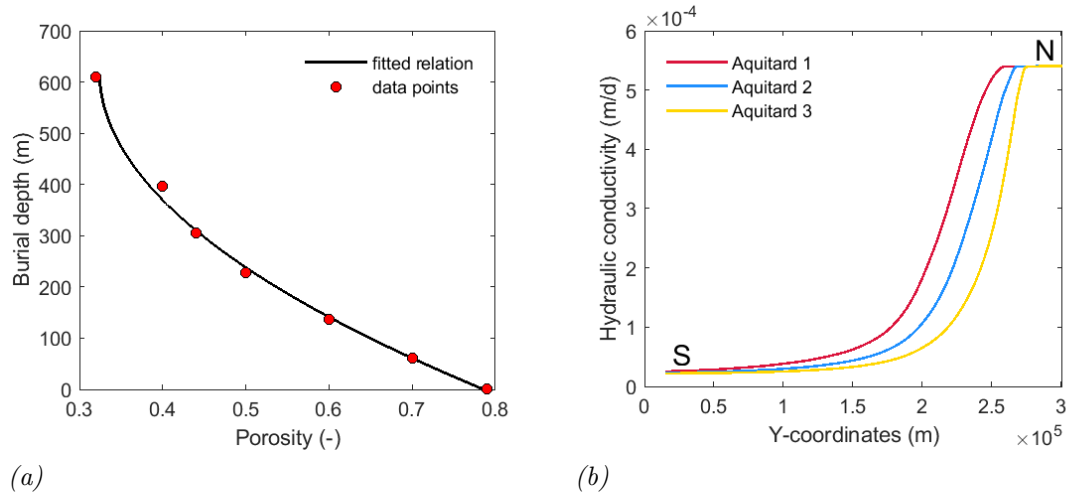
FIGURE 4.4: a) Burial depth versus porosity, based on relation of Dickinson (1953); b) Hydraulic conductivity of the three Pleistocene aquitards againt y-coordinates (north-south direction).

The resulting hydraulic conductivity of the three Pleistocene aquitards are depicted in Figure 4.4b. As the geological units dip towards the Gulf of Mexico, burial depth progressively increases southward. Consequently, the hydraulic conductivity of the aquitards have a southward decreasing gradient, see Figure 4.4b.

4.1.4 Storage coefficient

For transient modelling a storage coefficient for confined aquifer systems is required to simulate the water release of pores due to head changes. The storage coefficient is defined as follows (Fitts, 2011):

$$S = S_s * d \tag{4.5}$$

- S_s, is the specific storage, (m^{-1});

- d, is the vertical layer thickness, (m).

Equation 4.5 demonstrates that the storage coefficient depends on the vertical thickness of an aquifer/aquitard. Dial & Sumner (1989) estimated a mean storage coefficient of $0.5*10^{-3}$ (-) for all the aquifers in the study area. This mean storage coefficient and mean aquifer thickness were used to compute a specific storage value for each aquifer according to Equation 4.5. This value is indicated in Figure 4.5a for each aquifer. Subsequently, this

specific storage value was used to compute a thickness-varying storage coefficient for all the aquifers using Equation 4.5.

(a)   (b)
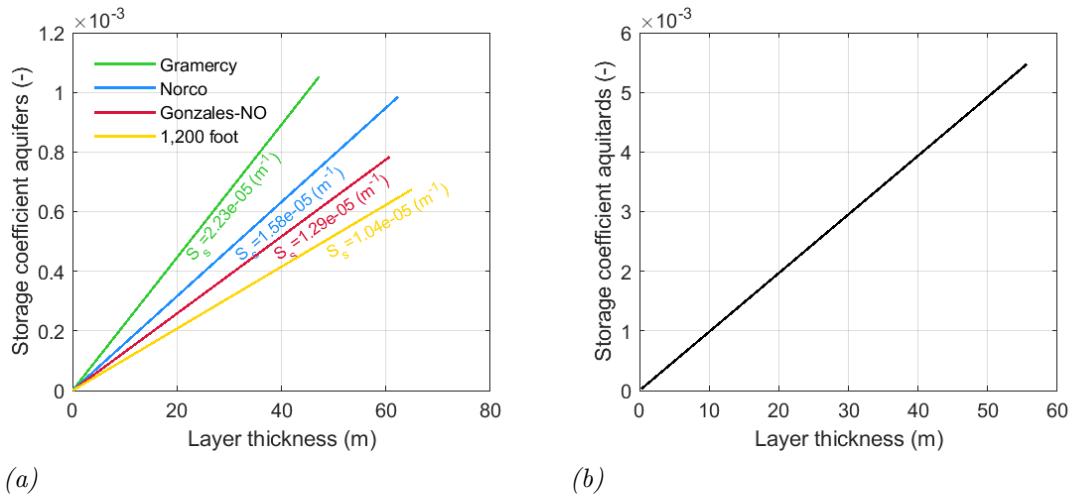
FIGURE 4.5: a) Layer thickness versus storage coefficient of aquifers. The specific storage for each aquifer is also indicated in the plot; b) Layer thickness versus storage coefficient of aquitards.

Whiteman (1980) measured an average specific storage of $9.14*10^{-6}$ (m^{-1}) for the aquitard system near Baton Rouge. This specific storage was used to compute a thickness-varying storage coefficient for three Pleistocene aquitards using the thickness of the aquitards. The relation between thickness and the storage coefficient is shown in Figure 4.5b. As the Holocene clay layer is phreatic, a specific yield was assigned. A specific yield of 0.02 was selected for this clay layer, which is the average specific yield for clay found by Johnson et al. (1967) for 17 samples at different locations mainly in the USA.

4.1.5 Surface hydrology

Mean annual potential recharge of 250 mm/yr determined for southwestern Mississippi and southeastern Louisiana over 1950-2010 by Beigi & Tsai (2015) was homogeneously applied to the top layer. Seasonal variation or climatic trends in recharge were neglected. The river network was represented by the most significant rivers within the model domain, including the Mississippi River and the Atchafalaya River tributary, Pearl River, Pascagoula River and Mobile River. The depth and the course of these rivers were obtained from a global river database, which used basic hydraulic geometric equations to derive river width and depth from discharge and velocity data from HydroSHEDS (Andreadis et al., 2013). The stages of these rivers were not modelled explicitly, as the influences of these rivers are assumed to be minor due to the thick Holocene clay layer. The rivers were assumed to have a stage similar to the surface elevation they are located in. River-groundwater interaction was simulated using a conductance of 10,000 (m^2/d) and an infiltration factor of 1. The gulf of Mexico was modelled using a constant head boundary of 0 meter NGVD29. The larger lakes and salt marshes at the land limit of the Gulf of Mexico were simulated using a general head boundary with a conductance of respectively 1,000 (m^2/d) and 500 (m^2/d). Drainage of water by sewers, small canals and irrigation is simulated by a constant drainage

of 1 meter below surface level. The drainage module has a conductance of 1,000 (m^2/d) excluding the areas where large surface water bodies are present. See Figure 4.6 for the spatial distribution of the different model elements.
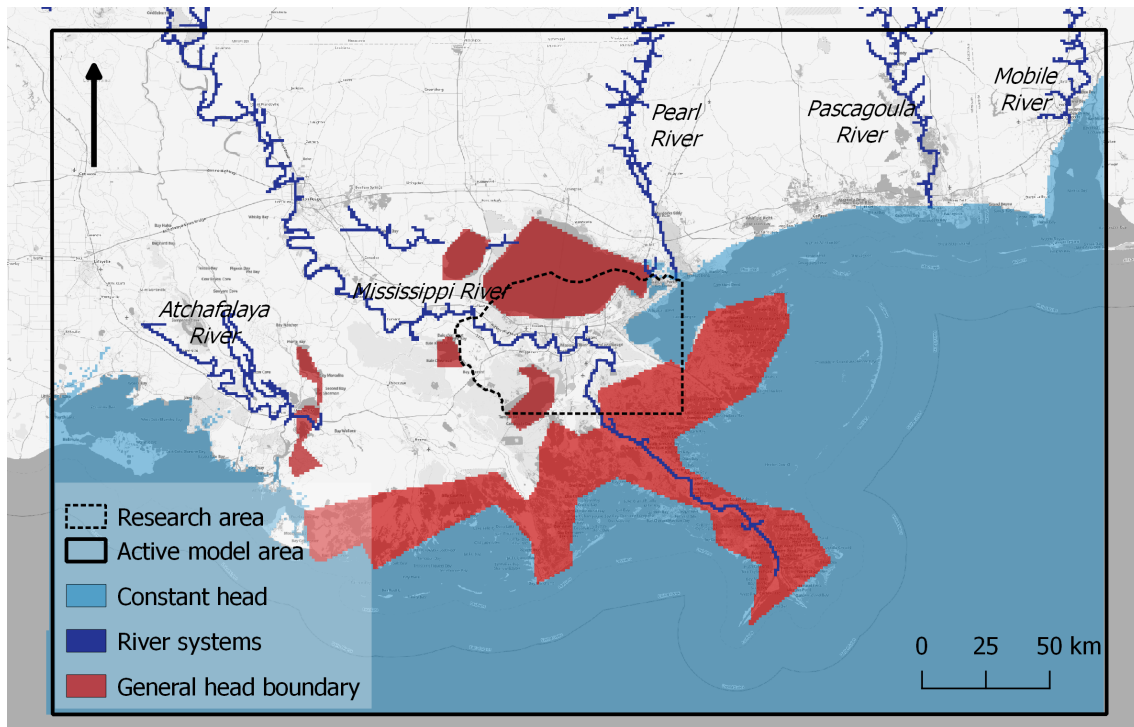
FIGURE 4.6: Spatial distribution of important model packages.

4.1.6 Groundwater extractions

Groundwater extractions were implemented to simulate the historical hydraulic head dynamics in the research area. Significant groundwater extractions have been reported since 1900 and are predominantly extracting groundwater from the Gonzales-NO aquifer and to a lesser extent from the Norco aquifer. Therefore only extraction wells located in these two aquifers were considered.

Unfortunately, historical information about groundwater extraction in the research area is limited and incomplete. All information about groundwater extraction wells in the research area is documented by the SONRIS database (www.SONRIS.com). This database provided a good overview of well locations, but additional information as yield, date of completion, current status, date of inactivation and casing diameter were inconsistently documented. Moreover, only a single yield per well is defined, which presumably corresponds to yield at moment of reporting. A variable yield depending on the groundwater demand was expected. The following steps were carried out to obtain a detailed and time-varying record of groundwater extractions in the research area:

- Well locations were retrieved from the SONRIS database. Only wells that were extracting from the Gonzales-NO and Norco aquifers in the Saint-Charles, Jefferson, Orleans and Saint-Bernard parishes were considered. If documented also the yield,

date of completion and data of inactivation were adopted. Wells with a very short lifespan or low yield were removed from the record.

- To estimate a yield for wells without a defined yield, a relation between the diameter of the well casing and yield of the remaining wells was fitted. The following relation was determined (R^2=0.43), see appendix A for fit:

$$\text{Yield (gal/min)} = 192.62 \cdot \text{Casing Diameter (in)}^1 \qquad (4.6)$$

- To account for a time-varying yield, a series of reports about water use in Louisiana, published every 5 years since 1960, were used (Snider & Forbes, 1961; Bieber & Forbes, 1966; Dial, 1970; Cardwell & Walter, 1979; Walter, 1982; Lurry, 1987; Lovelace, 1991; Lovelace & Johnson, 1996; Sargant, 2002, 2007; Sargent, 2011). These reports documented the total groundwater use per parish. The ratio's of groundwater use per parish between the Norco and Gonzales-NO aquifer were computed based on the SONRIS database. These ratios were multiplied with the total groundwater use per parish to obtain the total groundwater use per parish and per aquifer,

- These five yearly values were linearly interpolated to get yearly total groundwater use per parish and per aquifer;

- These values were used to compute a correction factor between cumulative extraction rate and the actual reported groundwater use. This yearly correction factor was multiplied by the yield of individual wells to obtain a final time-varying yield per well.

Accordingly 118 wells were implemented in the Gonzales-NO aquifer and 57 wells were implemented in the Norco aquifer (see Figure 4.7a). Figure 4.7b shows yearly cumulative extracted groundwater for both aquifers. The figure shows that the Gonzales-NO aquifer is most heavily pumped in the study area. Moreover, the yearly amount of extracted groundwater increases for both aquifers until 1960-70, followed by a significant reduction in groundwater use from these aquifers.

To evaluate the outlined method, Figure 4.8 shows the wells with the highest cumulative extraction rates for the entire model period. The fifteen most important wells extracting from the Gonzales-NO aquifer and ten most important wells extracting from the Norco aquifer are included. The wells displayed at Michoud and Nine Mile point, correspond with industrial extractions by the Entergy facilities and are both described by Prakken (2009) and Dial & Sumner (1989) (see also Figure 3.5b). The large extraction wells displayed at Mid-City NO and at the industrial canal in Gentilly are also identified by Dial & Sumner (1989). Finally the extraction wells at the industrial facility of Norco are mentioned by Jones et al. (2016). Although the previous does not provide any validation with respect to timing of individual wells, this method was able to identify the most prominent groundwater production sites.

---

[1]units were not explicitly mentioned.
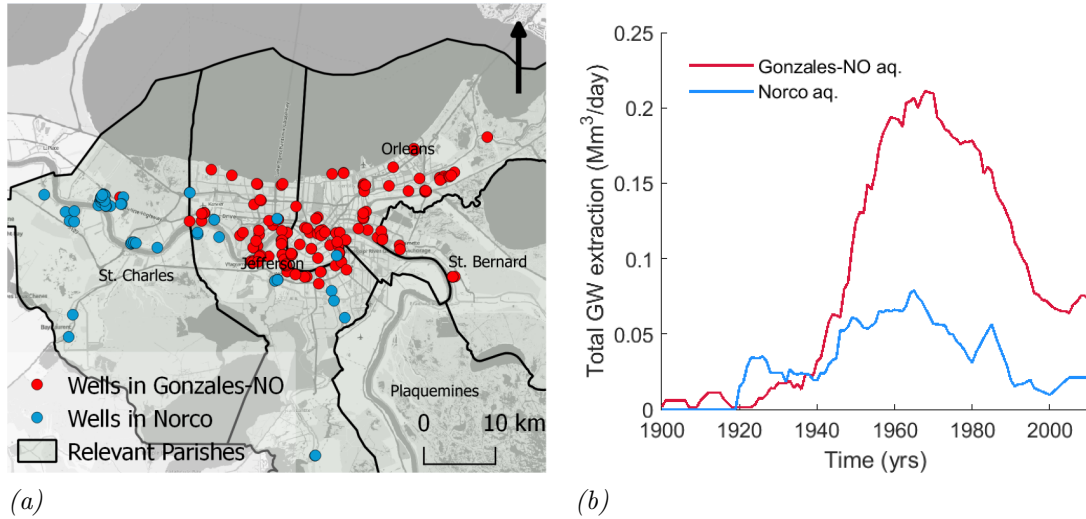
FIGURE 4.7: a) Groundwater extraction wells in the Norco (red) and Gonzales-NO aquifer;
b) Reconstructed historical groundwater use in the Greater New Orleans area for the
Gonzales-NO and Norco aquifer from 1900 to 2010.

4.1.7 Geotechnical parameterization

This section explains how ranges of geotechnical parameters were determined, which were later used as input for the sensitivity and uncertainty analysis. As local geotechnical data was restricted to the Holocene facies in the research area (Kuecher, 1994), the geotechnical parameters were based on general relationships between compression parameters and sediment properties. The NEN-Bjerrum model requires compression ratios, rather that compression indices for the geotechnical parameterization. The latter are the conventional type of geotechnical parameters considered by most of the literature. All determined compression indices were converted to compression ratios using Equation 4.7.

$$RR/CR/C_\alpha = \frac{C_r/C_c/C_{\alpha e}}{1 + e_0} \tag{4.7}$$

Where, e_0 is the initial void ratio, (-).

An average initial void ratio was determined for each aquitard based on its burial depth using Equation 4.2 (Dickinson, 1953) and Equation 4.3 (Abelev & Tsytovich, 1964). The geotechnical parameters determined in this section are summarized in Table 4.2.

The geotechnical parameterization of the aquifers was based on the NNI database for Dutch soils ((NNI, 2012) in (Kooi et al., 2018)). As no geotechnical data of aquifers was available and the compaction of sandy aquifer is less significant in comparison to compaction of fine-grained aquitards, this was assumed to be sufficient. See Table 4.2 for the geotechnical parameters of the aquifers. As this study aims at quantifying the contribution of land subsidence due to deep groundwater production, the parameterization of the Holocene Clay layer was similar to the aquifers. This way the contribution of high 'autonomous' creep rates by the Holocene clay layer, as might be the case for given parameter combinations is limited.
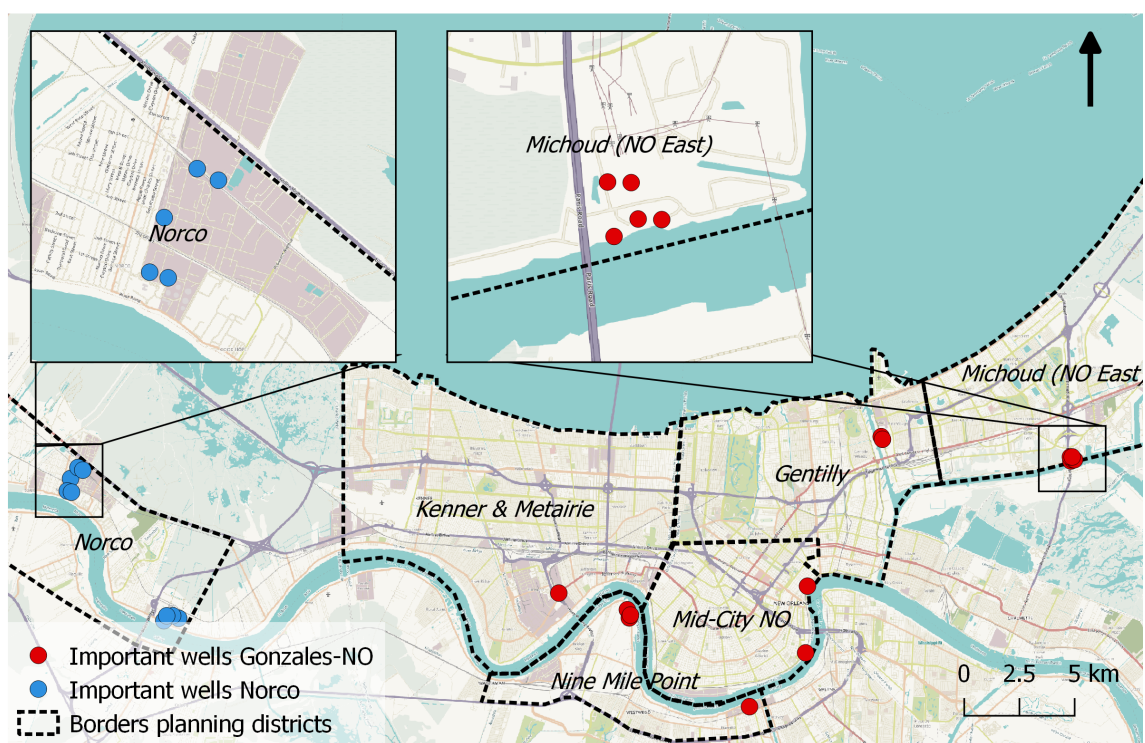
FIGURE 4.8: Most significant pumping wells for the Gonzales-NO (red) and Norco aquifer (blue).

In contrast, the geotechnical parameterization of the aquitards is much more relevant in this study and was based on (local) relations between physical soil properties and compression parameters.

Two empirical relations between initial void ratio (e_0) and compression index (C_c) were used to determine a range of compression ratios. Jafari et al. (2018) established Equation 4.8 for a Holocene clay in coastal Louisiana:

$$C_c = 0.39 \cdot e_0 + 0.06 \tag{4.8}$$

Alternatively Equation 4.9 comprises a more general relation for fine-grained inorganic clays (Hough (1957) in Jafari et al. (2018)):

$$C_c = 0.29 \cdot e_0 - 0.27 \tag{4.9}$$

The discrepancy between the two relations is discussed by Jafari et al. (2018) in the context of sample disturbance. Without information about how well equation 4.8 represents deeper clay layers, both equations were assessed. The previously determined initial void ratios

were used to compute two spatially uniform compression indices were computed for all aquitards (see Table 4.2).

Recompression indices were based on an empirical relation between the compression and recompression index for a New Orleans clay (Das (2004) in Vipulanandan et al. (2008)). Two relations between the compression and recompression indices define a range of New Orleans clays:

$$\text{Lower Limit}: C_r = 0.148 \cdot C_c \tag{4.10}$$

$$\text{Upper bound}: C_r = 0.280 \cdot C_c \tag{4.11}$$

Using these equations and the previously computed compression indices, two ranges of recompression indices for each aquitard were determined. In absence of a better definition and to limit our possibilities, only the mean values of both ranges were used for further computations. Finally, the secondary consolidation indices for all aquitards were computed using a $\frac{C_\alpha}{C_c}$ ratio of 0.04 ± 0.01 for inorganic clay's and silts (Mesri & Godlewski, 1977).

No OCR value is defined for the aquifer system in the research area. OCR values for similar delta deposits are within a wide range: Belfast, UK 1.2-1.8 (Crooks & Graham, 1976), Bangkok, Thailand 1.5 (Phien-Wej et al., 2006). A model study to subsidence in the Mekong Delta (Minderhoud et al., 2017) found an optimal spatially uniform OCR range of 1.45-1.75. Therefore, this study assessed an OCR range of 1.2 to 1.6 with an intervals of 0.1, which seems in combination with the other variables a reasonable range.

TABLE 4.2: Range of geotechnical parameters per geological unit.

Ratios	Compression (Hough - Jafari)	Recompression (Hough[1]- Jafari[1])	Secondary Compression (Hough[2]- Jafari[3])
Holocene Clay	0.004	0.002	0
Aquitard 1	0.1506 - 0.2651	0.0322 - 0.0567	0.0060 - 0.0106
Aquitard 2	0.1273 - 0.2442	0.0272 - 0.0523	0.0051 - 0.0098
Aquitard 3	0.1016 - 0.2212	0.0218 - 0.0473	0.0041 - 0.0088
Aquifers	0.004	0.002	0

[1] Median value.

[2] Multiplication factor is 0.04, note this factor is governed by an uncertainty of ±0.01.

Although the obtained geotechnical parameters for the aquitards cover a large range, the values are comparable to similar settings (e.g. (Bakr, 2015) and (Kooi & Yuherdha, 2018)). Evidently, Equation 4.8 (Jafari et al., 2018) generates significantly higher geotechnical parameters than Equation 4.9 (Hough, 1957). However, without information about how creep contributes to consolidation in aged and relatively deep buried Pleistocene clay, the obtained secondary consolidation ratios based on Equation 4.8 seem rather high.

4.1.8   Model settings

Hydraulic head levels were simulated using the MODFLOW-based environment iMOD (Vermeulen et al., 2018). Subsequently, the iMOD SUB-CR module (Kooi et al., 2018) was used to compute subsidence driven by the simulated hydraulic head dynamics. Both simulations were run transient from 1900 to 2010 with stress periods of one year. This is similar to the temporal resolution of the groundwater extractions. As this study decouples geohydrology and geotechnical response, subsidence was simulated one-way without the hydrological feedback of water release due to inelastic strain.

The initial starting heads of all model layers were set to 0 NVGD29, which is equal to mean sea level. As the hydrological feedback was disregarded, which typically may require a large spin-up time to prevent unrealistic shocks in the hydraulic head, no additional spin-up period was added before 1900. Moreover, hydraulic head levels were assumed to have approached new conditions by 1920, as the transient simulation starts with a steady-state simulation and significant groundwater extractions start only after 1920.

The iMOD option ICONSISTENCY (Vermeulen et al., 2018) was used to account for the intersecting model layers north in the model domain. As the alternating aquifers and aquitards converge towards the north, some layers have an outcrop area north of Lake Pontchartrain. As in the model design each geological unit is represented by a separate model layer, some model layers attain zero thickness and intersect each other in the north. IMOD does not allow model layers with zero thickness. The option ICONSISTENCY corrects for this by assigning a minimal thickness of 1 m to layer with zero thickness. Moreover, the hydraulic conductivity of the underlying layer is copied to this layer, to simulate the geological schematization correctly.

Table 4.3 lists the solver settings that were used to run the model and guarantee model convergence.

TABLE 4.3: Solver settings

Parameter	Setting
Number of outer iterations	150
Number of inner iterations	30
Head closure criterion	$1*10^{-3}$ (m)
Budget closure parameter	1000 (m^3)
Relaxation parameter	0.98

4.2 Model validation

4.2.1 Hydraulic head observations

Hydraulic head observations for both the Norco and Gonzales-NO aquifer were retrieved from the USGS waterdata website (waterdata.usgs.gov) and served as calibration and validation sets. The Gonzales-NO aquifer is relatively densely monitored over the last 100 years. In total 364 observation points were identified for the Gonzales aquifer in the greater New Orleans area. Norco is less intensively monitored in the study area, as only 134 observation points were identified. Most of the observation points comprise only one measurement in time. A few observation wells have relatively long time records.

TABLE 4.4: Locations of hydraulic head observation wells with a long time record.

Observation well	Aquifer	Location (x;y)	Period
Or-42	Gonzales-NO	1125504.2; 161287.2	1942-2010
Or-47 & Or-128	Gonzales-NO	1121966.0; 170534.7	1943-1986
Or-175	Gonzales-NO	1150132.8; 176754.1	1963-2010
Or-206	Gonzales-NO	1126110.2; 167929.4	1970-2010
Jf-178	Gonzales-NO	1104740.5; 170938.6	1984-2010
Jf-156	Gonzales-NO	1112995.6; 162419.2	1974-2010
Sc-6	Norco	1089441.4; 166976.0	1943-1953
Sc-24	Norco	1097192.2; 160067.4	1921-1985
Sc-82	Norco	1082764.3; 165748.4	1957-1989

4.2.2 Subsidence observations

Land subsidence observations in the research area are limited in time and space. The validation of the subsidence results will be more extensively considered in the discussion within the context of relevant literature. However, the subsidence observations derived from water gauge readings by (Dokka, 2011) were used to provide initial model validation. Dokka (2011) used monthly means of daily water gauge readings by the U.S. Army Corps of Engineers to derive a historical subsidence signal. Dokka (2011) employed several techniques to get rid of the effect of other processes, including: eustatic sea level rise, climatic factors and hydrological effects. As all the gauges were attached to bridges founded at depths below the based of local Holocene deposits, the measurements contain no contribution of Holocene compaction. However, the exact contribution of subsidence induced by groundwater extractions remains unclear, as multiple deep subsidence processes have been identified. Moreover, due to the employed techniques and the large distances covered, the observations are governed by a significant uncertainty. This study used the observations at four bridges located around urban New Orleans, see Table 4.5.

TABLE 4.5: Locations of land subsidence observations by (Dokka, 2011).

Name of station	Location (x;y)	Period
Paris Road Bridge	1132835.1; 167741.9	1960-1995
Seabrook Bridge	1125273.5; 170455.7	1960-1995
Irish Bayou	1142323.2; 184303.5	1960-1995
Florida Ave. Bridge	1125352.1; 163528.4	1960-1995

4.3   Sensitivity Analysis

The sensitivity of the land subsidence predictions was determined with respect to uncertainty in the hydraulic conductivity, geological schematization and geotechnical parameterization. The former two concern important components of the hydrogeological model and will first be assessed with respect to their influence on the hydraulic head predictions. Subsequently, it was assessed how the uncertainty in hydraulic head predictions propagates into the land subsidence predictions. This way we were able to disentangle the way hydraulic conductivity and geological schematization influence the land subsidence predictions. Three evaluation criteria were defined for the assessment of the prediction uncertainty of both hydraulic head and land subsidence predictions:

1. the magnitude of maximum drawdown/subsidence in the study area;

2. the maximum spatial extent of drawdown/subsidence in the study area;

3. the timing (year) of maximum drawdown/subsidence in the study area.

These three criteria cover the important aspects of potential impact by land subsidence: magnitude, scale and timing of subsidence. Previous studies have shown that both hydraulic conductivity and the geological schematization may affect the hydraulic head on all three aspects (Turnadge et al., 2018; Højberg & Refsgaard, 2005). Moreover, as the NEN-Bjerrum model accounts for transient viscous deformation, geotechnical parameterization may also affect the subsidence predictions on all three aspects. Drawdown instead of the hydraulic head predictions were incorporated in the evaluation criteria, as the subsidence calculations rely strongly on hydraulic head change rather than absolute values. With respect to the second evaluation criteria, the spatial extent was calculated summing the number of model cells exceeding drawdown of six meters and subsidence of 50 mm. These threshold values were chosen arbitrarily.

A wide range of model runs was performed to obtain the model sensitivity to the aforementioned model components. All model runs are summarized in Table 4.6. The model runs can be subdivided into two categories in line with the study set-up: runs that simulate the hydraulic head (H) and runs that simulate subsequent land subsidence (S). Within the first category two series of runs (HI1 and HI2) were performed to derive behavioral hydraulic conductivity distributions based on hydraulic head observations. Subsequently, the obtained hydraulic conductivity distributions were used to derive the uncertainty in hydraulic head predictions due to both hydraulic conductivity (HU1) and geological schematization (HU2). Within the second category first a series of runs was performed to obtain the model sensitivity to geotechnical parameters and select realistic parameter combinations (SI1). Due to the low quality of subsidence observations in the study area, the realistic parameter combinations were selected based realistic behaviour (no high autonomous creep) rather than model performance with respect to observations. Subsequently, three series of runs were performed to derive the uncertainty in the land subsidence predictions with respect to all proposed model components (SU1, SU2 & SU3).

TABLE 4.6: Overview of model runs.

	Name	Model focus	Model type	Model period	Number of runs	Hydraulic conductivity	Geotechnical parameterization	Geological schematization
						Parametric components		Structural component
	HI1	Calibration hydraulic conductivity (PEST)	Steady-state	1963 & 2008	2 x 1	Initial parameterization	-	8-layer model
	HI2	Select behavioural hydraulic conductivity combinations (GLUE)	Steady-state	1963 & 2008	2 x 3125	Combined PEST generated distributions	-	8-layer model
	HU1	Uncertainty due to hydraulic conductivity	Transient	1900-2010	31	Behavioural parameter combinations	-	8-layer model
	HU2	Uncertainty due to geological schematization	Transient	1900-2010	31	Behavioural parameter combinations	-	4-layer model
	SI1	Select geotechnical parameters and asses sensitivity	Transient	1900-2010	135 (81 visualized)	Deterministic parameter combination	All parameter combinations	8-layer model
	SU1	Uncertainty due to geotechnical parameters	Transient	1900-2010	47	Deterministic parameter combination	All selected 'realistic' parameter combinations	8-layer model
	SU2	Uncertainty due to hydraulic conductivity	Transient	1900-2010	4 x 31	Behavioural parameter combinations	4 selected parameter combinations (OCR 1.3 - 1.6)	8-layer model
	SU3	Uncertainty due to geological schematization	Transient	1900-2010	31	Behavioural parameter combinations	1 selected parameter combination (OCR 1.4)	4-layer model

Initialization — *Derive uncertainty* / *Initialization & sensitivity* — *Derive uncertainty*

Hydrogeology — **Land subsidence**

As demonstrated by the Table 4.6 the runs to derive the prediction uncertainty include all a series of runs rather than a single deterministic run. To obtain the prediction uncertainty the 95% confidence limits and median of the ensemble of runs were calculated. The relative performance of these statistical percentiles were compared on the basis of the three evaluation criteria to quantitatively asses the model sensitivity. Below the different type of runs are more detailed explained.

4.3.1   Hydraulic conductivity

The sensitivity of the model predictions to uncertainty in the hydraulic conductivity was most thoroughly investigated. Parameter calibration (PEST) and Generalized Likelihood Uncertainty Estimation (GLUE) were combined to find statistically well performing hydraulic conductivity distributions. These hydraulic conductivity distributions were used to obtain the prediction uncertainty of both the groundwater and land subsidence model.

Parameter calibration (HI1)

The iMOD PEST-tool, iPEST (Vermeulen et al., 2018), was used to find distributions of uniform optimization factors for the hydraulic conductivity. PEST compares hydraulic head predictions, ϕ, with observations, $\mathbf{y}$, and adjusts selected parameters using the Levenberg-Marquardt optimization algorithm and runs the model again until a minimal objective function value, ϕ_m, is obtained. iPEST uses the sum of squares as objective function (Vermeulen et al., 2018):

$$\phi_m(\mathbf{p}) = (\mathbf{y} - \phi(\mathbf{p}))^2 \tag{4.12}$$

- ϕ_m is the objective function, (-);

- p is the parameter vector with a length equal to the number of parameters to be optimized;

- y is vector of hydraulic head observations, (m);

- ϕ is the simulated hydraulic head for parameters p, (m).

After completing the parameter estimation process, iPEST calculates the 96% lognormal distributed confidence limits for the hydraulic conductivity of the adjustable parameters. These distributions indicate the sensitivity of a model layer to the hydraulic head observations. To ensure realistic values, the maximal optimization factor for initial hydraulic conductivity values was set to 100.

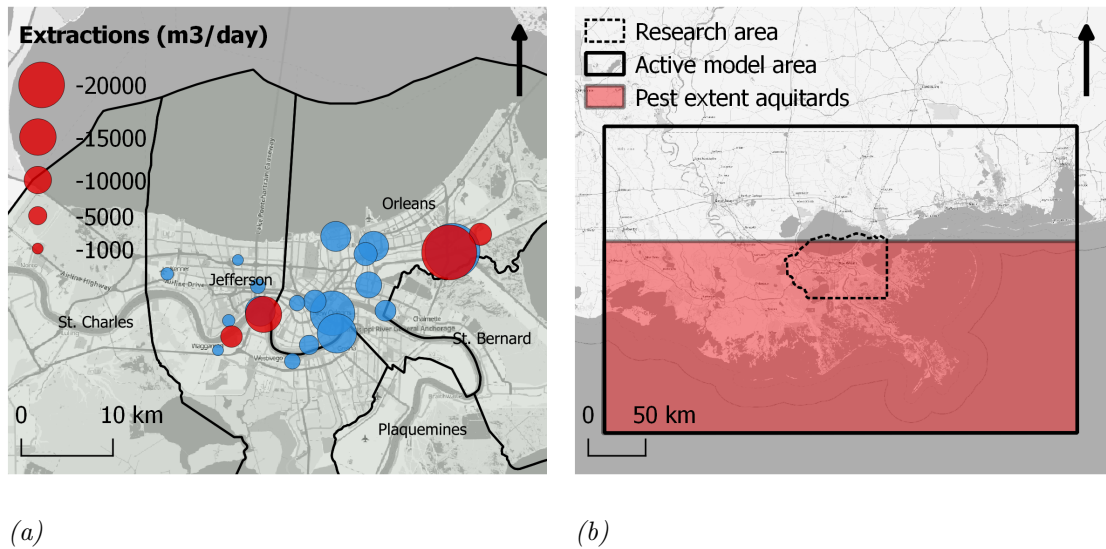(a)   (b)

FIGURE 4.9: a) Well locations and corresponding yield in the Gonzales-New Orleans aquifer (related to radius) for the situation in 1963 (Blue) and 2008 (Red). b) Pest extent with regard to the calibration of aquitards.

PEST was applied on a steady-state version of the hydrogeological model, as the record of historical groundwater extractions and hydraulic head observation was too limited to perform a full transient PEST analysis over the entire model period (1900-2010). Two steady-state models of 1963 and 2008 were selected, as for these years the spatial distribution and yield of extraction wells in the Gonzales-NO aquifers could be retrieved from the detailed reports by Rollo (1966) and Prakken (2009) respectively. Figure 4.9a shows the rate and locations of these extractions in the Gonzales-NO aquifer. For the Norco aquifer the locations and yield of extraction wells as found using the SONRIS database were incorporated.

Due to the lack of hydraulic head observations in the Gramercy and 1,200 foot aquifers and all aquitards, only hydraulic head observations of the Norco and Gonzales-NO aquifer were used for calibration. Consequently calibration of the upper model layers showed to be ineffective as high uncertainty values were attained. Therefore PEST was only applied on model layers 4 to 8, including the three lower aquifers and two lower aquitards. Hydraulic head observations were relatively abundant for both aquifers in 1963, see Table 4.7. If more than one observation per data point per year was available, the yearly averaged was used. In contrast, only one head observation was available for the Norco aquifer in 2008. Therefore, head observations from the entire period of 2000 to 2010 were used to better capture the spatial trend. As head levels are relatively stable over this period, this was assumed to be acceptable.

Constrained by hydraulic head observations, PEST was only applied on the southern part of the model domain, see Figure 4.9b. As aquitards have a north-south decreasing gradient in the hydraulic conductivity (see Section 4.1.3), this method also prevents unrealistically high or low hydraulic conductivity values by calibration in the northern part of the model domain.

TABLE 4.7: Number of hydraulic head observations used in PEST.

	1963	2008
Norco	13	6[1]
Gonzales-NO	37	39

[1] Over 2000-2010

Uncertainty estimation (HI2)

The Generalized Likelihood Uncertainty Estimation (GLUE) method was applied to select behavioural parameter combinations (i.e. model results exceeding a specified preset performance criterion) within the PEST generated hydraulic conductivity distributions. GLUE is a Monte Carlo based method, that rejects the idea of a unique set of parameters of the system to produce an optimal solution (Beven & Binley, 1992). The method is used to identify behavioral parameter sets within a large set of possible parameter combinations. By comparing predicted model results to observations, each set of parameter combinations is assigned a likelihood value that quantifies the model performance. Based on a cutoff threshold the total ensemble of simulations is divided in behavioral and non-behavioral parameter combinations. As this cutoff threshold is defined arbitrarily, the uncertainty bounds are rather subjective. This threshold is either defined in terms of a certain allowable deviation of the highest likelihood value or as a fixed percentage of the total number of simulations (Blasone et al., 2008). The GLUE method was implemented following these steps:

1. **Define a range of parameters**
   The PEST generated parameter distributions were used as input for the GLUE analysis. As PEST was performed on two-steady state models, two parameter distributions for each layer were available. PEST mean optimization factors for 1963 and 2008 were within the same order of magnitude and were averaged as input for the GLUE analysis. In contrast, due to the relatively large variation in the PEST 96% confidence limits between both models, all limits were used as input for the GLUE analysis. This way five hydraulic conductivity realisations per model layer formed input for the GLUE analysis. Similar to PEST, GLUE was only performed on the lowest five model layers. Five parameter options for five model layers, resulted in a total of, $5^5, 3125$ parameter combinations.

2. **Define likelihood function**
   The Kling-Gupta Efficiency (KGE) likelihood function was used to evaluate the modelled hydraulic head outputs against observed values. The Kling-Gupta Efficiency was derived by Gupta et al. (2009) as better alternative for the Nash-Sutcliffe efficiency (NSE). An advantage of the KGE coefficient is that it measures the model performance equally in the three main statistical component: the linear correlation, the bias and the variability, by calculating the Euclidean distance. The KGE function is defined as follows (Gupta et al., 2009):

$$KGE = 1 - \sqrt{(r-1)^2 + (\alpha - 1)^2 + (\beta - 1)^2} \tag{4.13}$$

- r (correlation coefficient): $\frac{cov(obs,sim)}{\sigma_{obs}\sigma_{sim}}$, (-);
- α (measure of variability): $\frac{\sigma_{sim}}{\sigma_{obs}}$, (-);
- β (measure of bias): $\frac{\mu_{sim}}{\mu_{obs}}$, (-).

Similar to PEST, the GLUE analysis was performed on the steady-state models of 1963 and 2008. Each steady-state model was run for 3125 parameter combinations. The KGE of the 3125 parameter combinations were calculated over entire set of hydraulic head observations and simulations lumped for both years. This method was allowed as the number of observations for both years were in the same order of magnitude. Moreover, by considering the performance of both model lumped, the method corrected for the unaccounted groundwater storage effects by steady-state models. It was assumed that the selected parameter combinations for the 2008 model were systematically producing lower head levels than the 1963 model in order to mimic the head observations, while a part of the drawdown is presumably caused by aquifer depletion due to the prolonged groundwater extractions.

3. **Choose a cutoff threshold value**
   The 1% best performing parameter combinations were selected to be behavioural. All selected models were assumed to be behavioural and equally true. The rest of the parameter sets was considered to be non-behavioural and not further considered. Hence 1% of 3125, 31 behavioural parameter sets for the hydraulic conductivity were appointed.

Transient model performance and uncertainty estimation
All 31 behavioural parameter combinations of the hydraulic conductivity were run transiently for both the hydrogeological model (HU1) and subsequent land subsidence module (SU2). The deterministic run, best performing hydraulic conductivity parameter combination, was used to evaluate the performance of the hydrogeological model. Hydraulic head observations in Gonzales-NO aquifer were used to calculate the correlation coefficient, r, for the period 1940-2010. Other layers did not include enough hydraulic head observations to assess their transient performance statistically. On the basis of nine observations wells (see Table 4.4) in both the Norco and Gonzales-NO aquifer, which all have relatively long time records, the model performance was assessed more qualitatively.

Modelled hydraulic head dynamics were converted to drawdown relative to the hydraulic head for 1900. The median and 95% confidence limits of the ensemble of drawdown and land subsidence predictions were determined and evaluated against the three evaluation criteria to assess the uncertainty due to hydraulic conductivity. To limit the number of transient model runs, only four selected geotechnical parameter combinations were run for the total ensemble of behavioral hydraulic conductivity parameter sets (see Section 4.3.3). Besides the average subsidence in the research area, modelled subsidence is compared with observed subsidence derived from water gauge readings by Dokka (2011) at four locations (see Section 4.2.2).

4.3.2 Geological schematization

An alternative, more simplified geological schematization was run to investigate the sensitivity of the hydraulic head and land subsidence predictions to the geological schematization. Since the Gonzales-NO aquifer is the most important aquifer in the study area with respect to groundwater production, predominantly information about this aquifer was available. Information of the other aquifers and aquitards is of lower quantity, as these units were historically seen less of interest. With up-scaling studies as proposed by Erkens & Sutanudjaja (2015) in mind, we need to asses how the subsidence model predictions are affected for a drastically simplified geological schematization. An alternative geological schematization composed of four hydrogeolocal units was considered, including the Holocene clay layer, an upper Pleistocene aquitard, the Gonzales-NO aquifer and a lower Pleistocene aquitard. To guarantee model convergence, the eight layer model structure was retained. Hydrogeological and geotechnical parameterization of the Holocene clay layer and Gonzales-NO aquifer was unaltered. The parameter values of the upper and lower Pleistocene aquitards were assigned according to the aquitard 2 and aquitard 3 respectively. The magnitude of the groundwater extractions were also unaltered, although all wells were set to extract from the Gonzales-NO aquifer. For a full comparison with the eight-layer model, the same behavioural parameter sets of hydraulic conductivity, as found with the GLUE analysis, were assessed. However, as less model layers were considered, not all parameter combinations were relevant.

Fourteen different parameter combinations were run transiently for both the hydrogeological model (HU2) and subsidence module (SU3). Similar to the previous section the hydraulic head predictions were converted to drawdown. The median and 95% confidence limits of the ensemble of drawdown and land subsidence predictions were determined and evaluated against the three evaluation criteria.

4.3.3 Geotechnical parameterization

Parameter sensitivity (SI1)

The geotechnical parameters, as perceived in Section 4.1.7, are rather ambiguous, as geotechnical information to constrain these parameters was absent. Both empirical relations (Equation 4.8 (Jafari et al., 2018) and 4.9 (Hough, 1957)) that were used to find the compression ratios for the aquitards cover a large range. To grasp the behaviour and sensitivity of the geotechnical parameters and to obtain land subsidence predictions corresponding to both empirical relations, a sensitivity analysis was carried out using the established range of geotechnical parameter of the aquitards. The proposed analysis did not consider whether parameter combinations were realistic or not. As the NEN-Bjerrum model calculates strain based on all four geotechnical parameters (see Section 2.2.2), it was expected that parameters influence each other significantly. Therefore a simple One-at-a-Time sensitivity analysis was assumed not to be representative. All possible parameter combinations were conducted to obtain the sensitivity to both the direct influence of a parameter and the joint influence due to interactions of parameters (Pianosi et al., 2016).

TABLE 4.8: Range of geotechnical parameters per geological unit as used in the sensitivity analysis. Bold parameter values were used in the uncertainty estimation of land subsidence predictions due to hydraulic conductivity and geological schematization.

Ratios	Compression	Recompression	Secondary Compression
Aquitard 1	0.1506	0.0322	**0.0030**
	0.2079	**0.0445**	0.0045
	0.2651	0.0567	0.0060
Aquitard 2	0.1273	0.0272	**0.0025**
	0.1858	**0.0398**	0.0038
	0.2442	0.0523	0.0051
Aquitard 3	0.1016	0.0218	**0.0020**
	0.1614	**0.0345**	0.0030
	0.2212	0.0473	0.0041

To limit the computational time, only a small number of parameter values were incorporated in the sensitivity analysis, see Table 4.8. Both outer values of the range and corresponding mean value were selected for the compression and recompression ratio. As described in the SUB-CR manual (Kooi et al., 2018) the geotechnical parameterization should be chosen in such a way to prevent unrealistically high initial creep strain rates. As the obtained secondary compression ratios were rather high, only the most conservative values were selected for the sensitivity analysis. A $\frac{C_\alpha}{C_c}$ ratio of 0.03 ± 0.01 instead of the 0.04 ± 0.01 ratio (Mesri & Godlewski, 1977) was used to compute three recompression ratios based on the compression ratio using Hough (1957). All OCR values of 1.2 to 1.6 with an interval of 0.1 were conducted. Accordingly, a total of 135 parameter combinations were assessed. Since the focus of this part of the study was on the geotechnical parameterization, only the deterministic set of hydraulic conductivity values adopted from GLUE was used in this analysis. The sensitivity of the land subsidence predictions to the geotechnical parameters, were assessed with respect to averaged maximum magnitude, maximum spatial extent and timing of averaged maximum subsidence in the research area for each parameter combination.

Parameter selection (SI1)

Despite the small adjustment of the secondary compression parameter, a significant number of parameter combinations generated unrealistic background subsidence (autonomous viscous deformation). To select realistic geotechnical parameter combinations and derive more realistic subsidence predictions, the parameter combinations that generated excessive background subsidence were filtered out. Equation 4.14 (Kooi et al., 2018) was used to estimate the contribution of creep deformation without pumping for all parameter combinations.

$$\dot{\varepsilon}_{cr} = \frac{d\varepsilon_{cr}}{dt} = \frac{log(e) \cdot C_\alpha}{\tau} \tag{4.14}$$

where,

$$\tau = \tau_{ref} OCR^{\frac{CR-RR}{C_\alpha}}, \tau_{ref} \text{ is 1 day.} \tag{4.15}$$

If creep deformation,$\dot{\varepsilon}_{cr}$, exceeded a threshold of 0.01 (-) in 100 years, the parameter combination was determined to be unrealistic. This way 47 geotechnical parameter combinations were selected as 'realistic'. Note that this selection criterion was based on realistic behaviour and not on model performance with respect to observed land subsidence.

A limited number of geotechnical parameter combinations were selected for the model runs to determine the uncertainty in land subsidence predictions with respect to hydraulic conductivity (SU2) and geological schematization (SU3). For the ensemble of hydraulic conductivity runs four parameter combinations were selected, including fixed values for the compression, recompression and secondary compression parameters (the selected parameter values are bold in Table 4.8) and a range of OCR values (OCR 1.3 - 1.6). These parameter combinations were chosen as they were all selected as realistic and cover a significant OCR range. For the model runs to determine the effect of the geological schematization the same values for the compression, recompression and secondary compression ratios were selected and combined with a fixed OCR of 1.4.

Uncertainty estimation (SU1)
The median and 95% confidence limits of the land subsidence predictions of the ensemble of realistic geotechnical parameter combinations were determined and evaluated against the three evaluation criteria. Besides the average subsidence in the research area, modelled subsidence is compared at five locations over the study area, which coincidence with the the locations of subsidence observations by Dokka (2011) (see Section 4.2.2).

5 Results

5.1 Hydrogeology

5.1.1 Hydraulic conductivity distributions

This section evaluates the hydraulic conductivity distributions, which were selected by combining PEST calibration and a GLUE uncertainty analysis. The PEST generated lognormal distributed optimization factors for the hydraulic conductivity are depicted in Figure 5.1. Both the width and the intensity of the distributions vary per layer and per steady-state model. Sharp and peaked distributions are associated with well identifiable parameters, while flat distributions indicate a higher parameter uncertainty. In general, the hydraulic conductivity is more tightly defined for the steady-state model of 2008 than for the model of 1963. This may be related to the lower number of extraction wells in 2008 in both the Norco and Gonzales-NO aquifer resulting in relatively clear hydraulic head patterns. Only the Gonzales-NO aquifer displays an actual narrow distribution for both steady-state models, indicating a high sensitivity to changes in hydraulic conductivity. This is consistent with the fact that observations used for calibration are predominantly located in the Gonzales-NO aquifer. All other layers show much wider distributions, indicating higher parameter uncertainty. The widest distribution is demonstrated by aquitard 3. Although no clear relation between parameter uncertainty and type of layer (aquifer vs aquitards) can be observed, clearly the number of observations decreases the parameter uncertainty. This is also supported by hydraulic conductivity distributions of the Norco aquifer that demonstrates less uncertainty for the steady-state model of 1963, which comprises more hydraulic head observations.
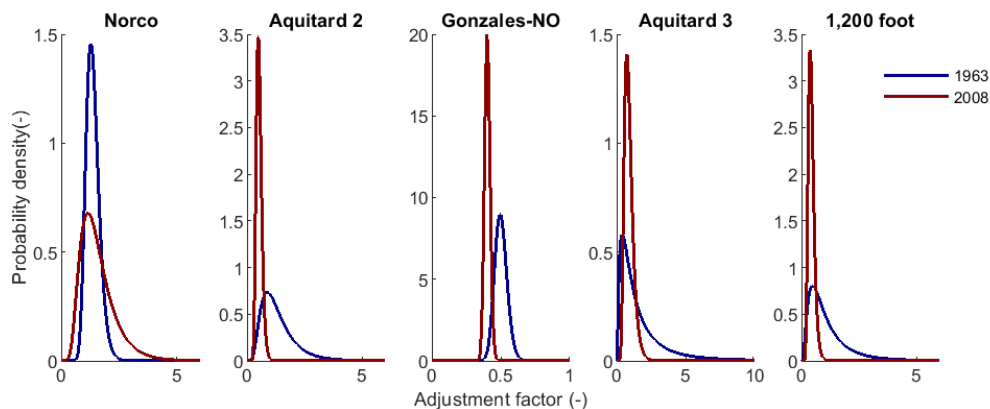

FIGURE 5.1: Lognormal distributed optimization factors as computed by the iMOD PEST-tool. Blue distributions correspond with the PEST analysis of the steady-state model of 1963 and the red distributions with the steady-state model of 2008. Note that the range of the y-axis varies per layer.

Table 5.1 lists the hydraulic conductivity values, retrieved from the initial hydraulic conductivity and PEST, which were used as input for the GLUE analysis. The hydraulic conductivity values of aquifers and aquitards are within the typical range of hydraulic conductivity values for sand and clays respectively (Fitts, 2011).

TABLE 5.1: Hydraulic conductivity values found with PEST and input for GLUE

		LL 1963 (m/d)	LL 2008 (m/d)	Mean (m/d)	UL 1963 (m/d)	UL 2008 (m/d)
Norco		43.59	27.78	69.08	102.87	182.44
Aquitard 2[1]	$\cdot 10^{-3}$	0.0476-0.0992	0.0389-0.0809	0.103-0.214	0.430-0.895	0.100-0.209
Gonzales -NO		14.97	13.07	16.22	21.57	16.03
Aquitard 3[1]	$\cdot 10^{-3}$	0.0137-0.0238	0.0383-0.0666	0.0946-0.164	0.866-1.50	0.169-0.294
1,200 foot		5.41	6.64	19.22	125.50	23.12

[1] Gradient within study area.

The with GLUE selected behavioral parameter combinations of both models performed well. The best performing parameter set of the steady-state model of 1963 has a KGE of 0.9503 and the steady-sate model of 2008 has a KGE of 0.9738. However, the selected 1% behavioural parameter combinations did not reveal any overlapping parameter combinations. Figure 5.2 shows the averaged simulated hydraulic heads corresponding with the selected behavioral parameter combinations for both steady-state models against observed hydraulic heads of both the Norco and Gonzales-NO aquifers in 1963. The figure shows that the assumption that both steady-state models, that in general disregard storage effects, correct differently for observed aquifer depletion was reasonable. The selected parameter combinations of the 2008 model are systematically producing lower head levels for the situation in 1963 than the selected parameter combinations of 1963. It was assumed that in order to mimic the groundwater observations the selected model parameters of the 2008 model produce lower heads, while a part of the drawdown can be actually explained by aquifer storage depletion due to the prolonged groundwater extraction.
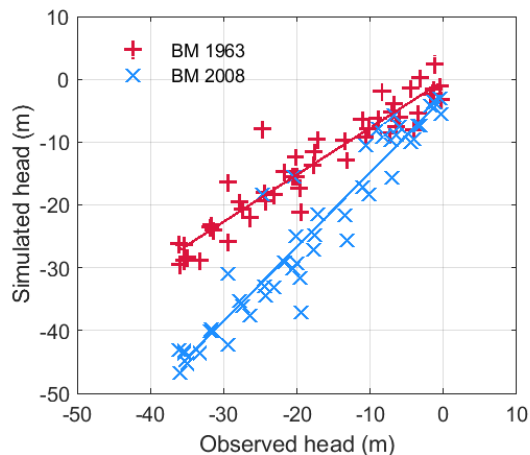

FIGURE 5.2: Scatter plot of observed and modelled heads for 1963. In red, averaged model results for best performing parameter combinations of 1963 and in blue averaged model results of best performing parameter combination of 2008 are depicted.

To account for this, the likelihood function, which was used to select the behavioural parameter combinations, assessed the model performance against all observed hydraulic head values for both years simultaneously. Figure 5.3 shows posterior frequency histograms of the selected behavioural parameter combinations of the hydraulic conductivity. Inherent to the method, the parameter sampling is restricted to the PEST-generated hydraulic conductivity distributions and are therefore not significantly different. However, the posterior frequency diagrams provide some new information. The shape of the posterior histrograms are expected to influence the shape of the prediction uncertainty of the transient simulations. Both the Norco and 1,200 foot aquifer show a more narrow distribution than the PEST generated distributions. These histograms are slightly skewed towards lower hydraulic conductivity values. The histogram of the Gonzales-NO aquifer shows a strong preference to the highest included hydraulic conductivity, although lower values are not ruled out. Both aquitards show still wide distributions, with a slight preference towards the higher hydraulic conductivity values. This is more pronounced for aquitard 2 than for aquitard 3.
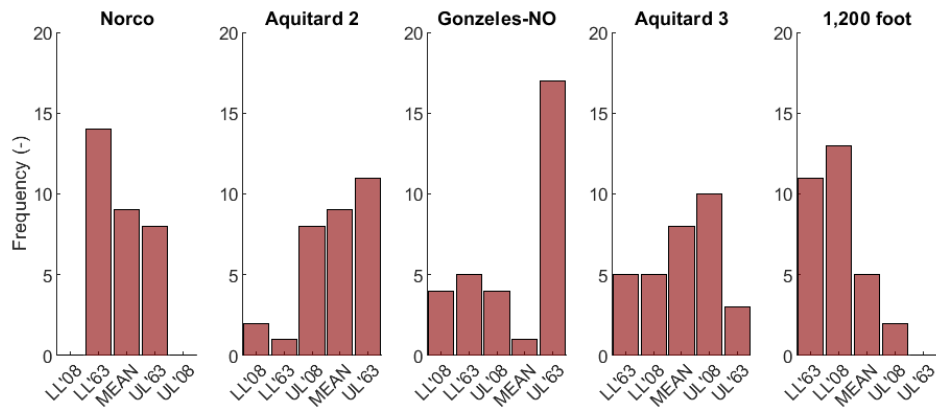

FIGURE 5.3: Posterior frequency histograms of hydraulic conductivity parameters. The labels on the x-axis correspond to the values in Table 5.1 and are ranked per model layer from low to high hydraulic conductivity values.

5.1.2 Transient model performance

This section considers the performance of the transient hydrogeological model based on hydraulic head observations in the Gonzales-NO and Norco aquifers. Figure 5.4a displays the modelled hydraulic head of the deterministic hydrogeological model (statistically best performing hydraulic conductivity combination) in the Gonzales-NO aquifer for 1970, which is the moment of maximum hydraulic head decline in the Gonzales-NO aquifer. Most significant head decline is displayed at the Michoud facility, with modelled heads exceeding 80 meters below NGVD29. Additionally, significant head decline near the industrial canal at Gentilly is modelled. The extent and locations of the cones of depression are fairly consistent with the situation as observed by Rollo (1966) for 1963 (see Figure **4.8**). For the simulated period with available hydraulic head measurements (1940-2010), the trend in the median groundwater head in the Gonzales-NO aquifer has a high correlation with head observations (r=0.83). Other layers do not have enough hydraulic head observations to assess their transient performance statistically.
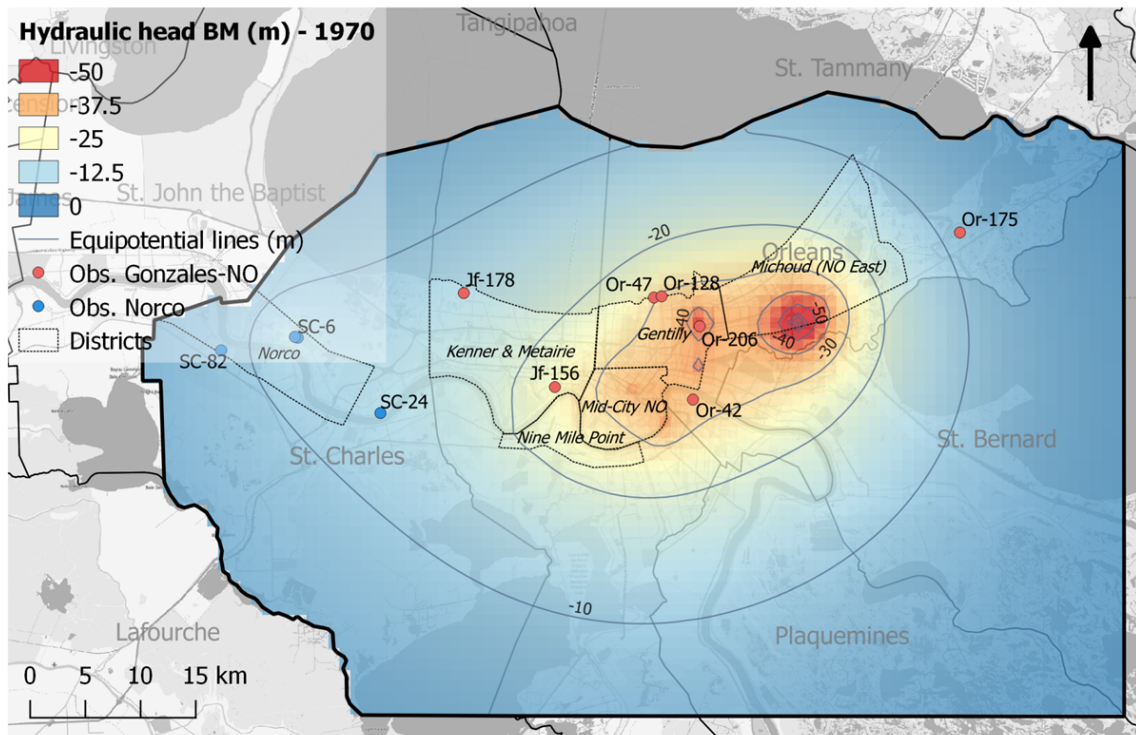
(a)
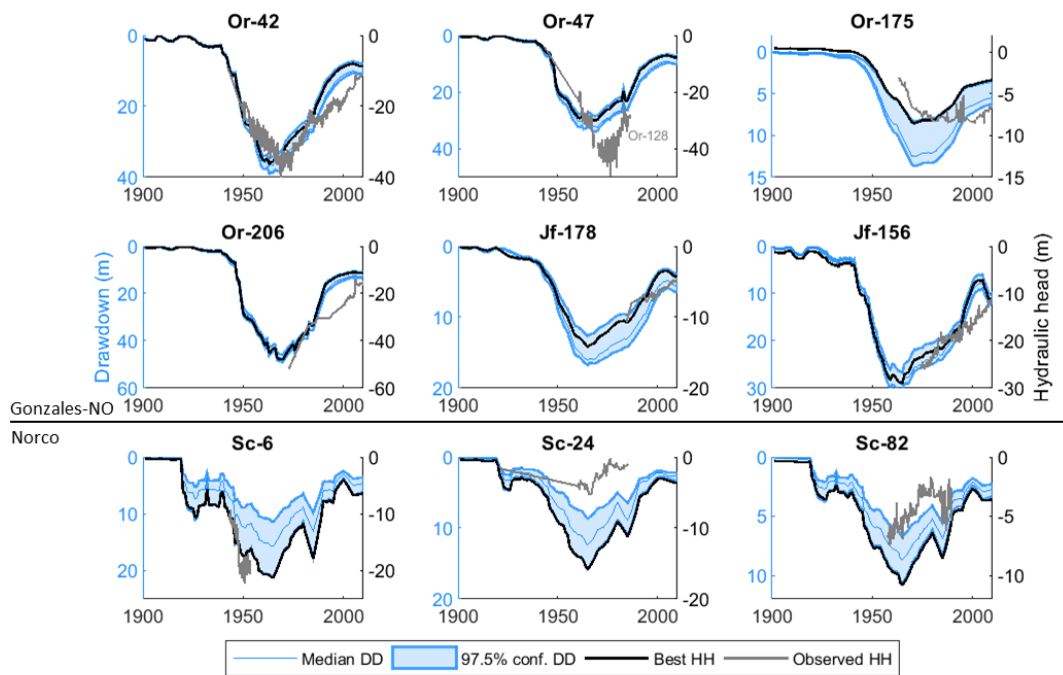
(b)

FIGURE 5.4: a) Modelled hydraulic head for deterministic hydraulic conductivity parameter set in the Gonzales-NO aquifer for 1970. Equipotential lines have a 10 m interval. b) Left y-axis: distribution of drawdown dynamics for the entire model period for Gonzales-NO and Norco aquifers. The median and 95 % confidence limits are indicated. Right y-axis: timeseries of hydraulic head for deterministic hydraulic conductivity parameter set. In grey the corresponding observed hydraulic head dynamics are depicted. ALl locations are indicated in figure a.

Figure 5.4b shows the observed head dynamics (grey) and modelled head dynamics for the deterministic model (black) at six locations in the Gonzales-NO aquifer and three locations in the Norco aquifer. The hydraulic head dynamics of the Gonzales-NO aquifer are clearly better grasped by the model in comparison to the Norco aquifer. However, also the model results for the Gonzales-NO aquifer deviate significantly from the observed hydraulic head at some locations. In the northern part of the research area, approximate to observation points Or-47 & Or-128 modelled heads underestimate the observed head decline, while the head dynamics in the eastern part of the research area, near Or-23 & Or-175 are overestimating the decline. At the other locations the hydraulic head is well simulated both with respect to timing and magnitude. Following maximum head decline, which occurs slightly earlier in the west around (1965) than in the east (1970), substantial head recovery is both simulated and observed. The hydraulic head dynamics in the Norco aquifer, show a more fluctuating signal. Although the trend shows to be reasonable in comparison to the observations, the absolute differences between simulations and observations are significant. Drawdown is underestimated at Sc-6, which is the location of the significant groundwater extractions at the Norco industrial facility. In contrast, more distant from this industrial facility the head decline is overestimated. The model seems to predict a more shallow, but further extending cone of depression in comparison with the observations.

5.1.3 Drawdown trends

The previous section showed that based on hydraulic head observations the groundwater model performance for the Gonzales-NO and Norco aquifers is reasonably accurate. Unfortunately, the performance of the remaining hydrogeological layers could not be assessed due to the lack of observations. As land subsidence calculations rely strongly on the hydraulic head change, the hydraulic head dynamics were converted to drawdown. This section considers the mean modelled drawdown trends in all relevant layers. Table 5.2 lists the mean maximum and absolute maximum drawdown in the study area since 1900 for all relevant hydrogeological layers. The table also includes the confidence limits due to uncertainty in the hydraulic conductivity. In addition, Figure 5.4b shows the distribution of drawdown dynamics (blue) for nine locations in the study area. This section only considers the median drawdown derived from the ensemble of behavioural model results. Comparing the locations of maximum drawdown in Table 5.2, demonstrates that the upper three Pleistocene layers are dominated by extractions from the Norco aquifer at Norco. Head decline is most pronounced in the Norco aquifer itself, although aquitard 1 also shows a significantly lowered hydraulic head locally. The Gramercy aquifer seems to be relatively unaffected by any extractions, as no significant drawdown is modelled in the layer. The lower four layers are clearly influenced by large extractions from the Gonzales-NO aquifer at Michoud. All four layers show a significant decline in hydraulic head, being most pronounced in the Gonzales-NO aquifer itself. Comparing the timing of mean maximum drawdown, shows that the response time of aquitards to the head decline in aquifers is fast. Only the moment of maximum drawdown in aquitard 1 occurs one year after the moment of maximum drawdown in the Norco aquifer. A similar trend is demonstrated by the timing of absolute maximum drawdown in the study area. Only the timing of drawdown in aquitard 3 occurs significantly later than in the Gonzales-NO aquifer. However, further consideration of the

head dynamics in Figure 5.4b, shows that the drawdown in both layers is relatively constant between 1970-80. Therefore, the apparent time lag of aquitard 3 may reflect subtle difference in head dynamics rather than a slow response time of the aquitard. The moment of maximum head decline occurs earlier in the layers influenced by the Norco extractions, than in the lower layers influenced by the extractions in Michoud.

TABLE 5.2: Mean maximum and absolute drawdown in all relevant hydrogeological layers.

	Max. mean dd (m)			Max. dd (m)			Location
	LL (year)	Median (year)	UL (year)	LL (year)	Median (year)	UL (year)	lowest head
Gramercy	0.80 (1970)	0.37 (1968)	0.24 (1968)	1.84 (1967)	1.28 (1966)	0.74 (1967)	East of Norco
Aquitard 1	4.65 (1969	2.81 (1968)	2.08 (1967)	11.76 (1965)	8.67 (1965)	6.16 (1965)	Norco
Norco	8.52 (1968)	5.27 (1967)	3.92 (1967)	22.00 (1965)	16.28 (1965)	11.74 (1965)	Norco
Aquitard 2	11.01 (1970)	10.12 (1970)	9.05 (1970)	50.64 (1980)	38.78 (1971)	36.96 (1980)	Michoud
Gonzales-NO	12.11 (1970)	10.94 (1970)	8.09 (1969)	90.25 (1980)	72.54 (1970)	70.56 (1970)	Michoud
Aquitard 3	15.68 (1970)	13.47 (1970)	7.51 (1972)	53.96 (1980)	45.33 (1980)	38.57 (1980)	Michoud
1,200 foot	15.10 (1970)	11.89 (1971)	3.45 (1974)	28.10 (1970)	20.46 (1970)	4.74 (1973)	Michoud

5.1.4   Uncertainty due to hydraulic conductivity

Figure 5.4b and Table 5.2 indicate the 95% confidence limits of the drawdown distributions due to uncertainty in the hydraulic conductivity. In addition Figure 5.5 shows the standard deviation of the drawdown distributions, as measure of uncertainty, for the most relevant hydrogeological layers. The prediction uncertainties are evaluated against the three criteria, magnitude, timing and spatial extent of drawdown:

- **Magntitude of drawdown**
  Both Table 5.2 and Figure 5.4b show that magnitude of drawdown ranges significantly for the different hydraulic conductivity combinations. In general, the width and symmetry of the mean drawdown distributions show large agreement with the posterior hydraulic conductivity histograms. Aquitard 2, Gonzales-NO aquifer and 1,200 foot aquifer all show a very asymmetric confidence interval, corresponding to their asymmetric posterior histograms. The Norco aquifer and Aquitard 3 show relatively symmetric, but wide drawdown distributions, corresponding to the relatively wide and balanced hydraulic conductivity histograms. Figure 5.4b and Table 5.2 demonstrate contrasting trends with respect to the width of the drawdown distribution of the Gonzales-NO aquifer: the figure shows very narrow drawdown distributions corresponding to its tight hydraulic conductivity histogram, while the table shows that the distribution of absolute drawdown varies significantly. Apparently, the prediction uncertainty may locally increase significantly at the location of an extraction well (location of maximum absolute drawdown), while in general the
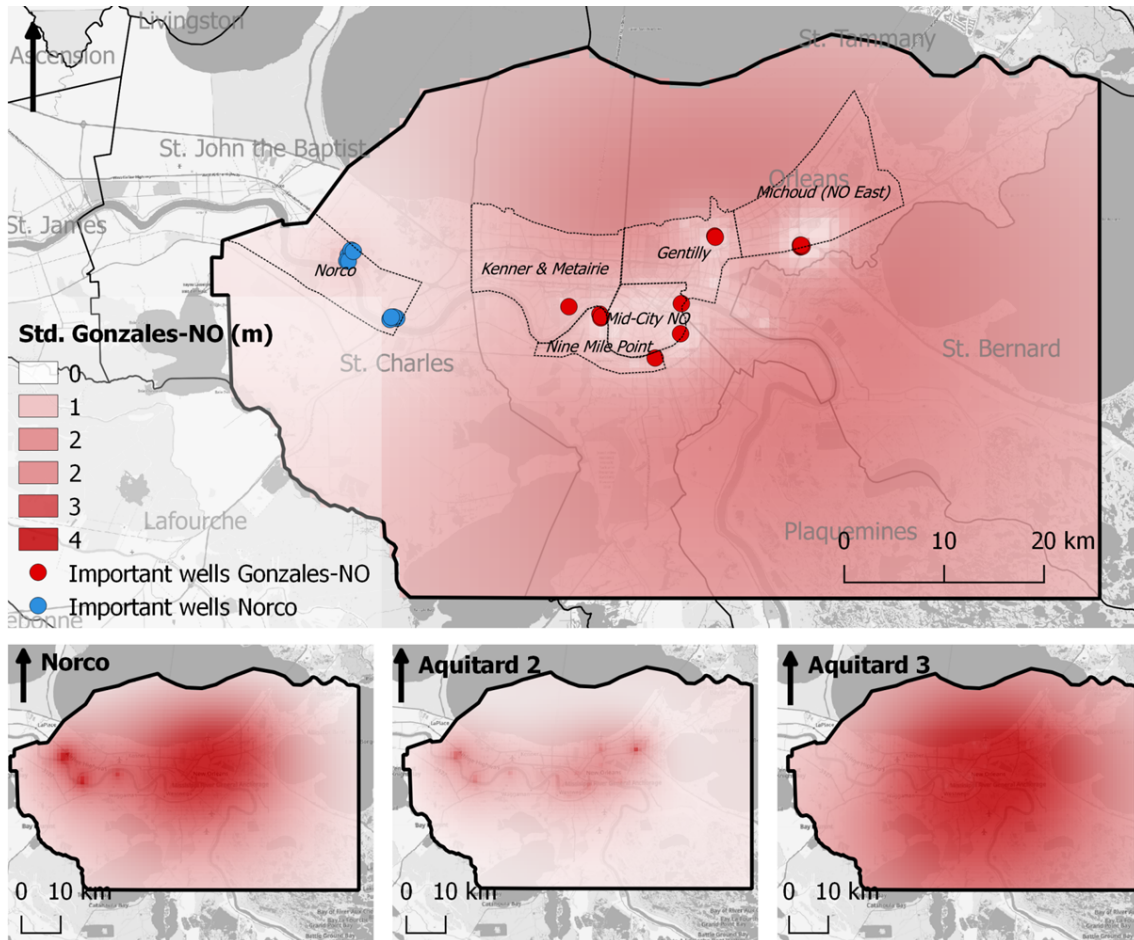
FIGURE 5.5: Standard deviation of the drawdown distributions for 1965 of the Norco (layer 4) and Gonzales-NO (layer 6) aquifers and lower two aquitards (layer 5 and 7 respectively).

hydraulic head distribution is narrow. Note that aquitard 1 has also a wide uncertainty distribution, despite it was disregarded in the GLUE analysis. Presumably, the aquitard is influenced by the uncertainty in hydraulic conductivity of the Norco aquifer. Figure 5.5 depicts a spatially more comprehensive picture of the variation in magnitude of drawdown for 1965. The Gonzales-NO aquifer displays the highest prediction uncertainty just outside the zone of large extraction wells. The opposite trend is demonstrated by both aquitards and the Norco aquifer, where the uncertainty in magnitude of the drawdown is the largest at the location of the groundwater extraction wells. As the uncertainty in hydraulic conductivity of the Gonzales-NO aquifer is small relative to the adjacent aquitards, the magnitude of drawdown in the Gonzales-NO aquifer is probably significantly influenced by uncertainty in hydraulic conductivity of these adjacent aquitards. In contrast the pattern of the other layer reflects more the variation due to the intrinsic uncertainty in hydraulic conductivity of these layers.

- **Spatial extent of drawdown**
  Figure 5.5 demonstrates that the hydraulic conductivity may significantly affects the extent of drawdown. Table 5.3 lists the extent of spatial drawdown in the research area for the 95% confidence limits and median of the total ensemble of behavioural

model predictions. This extent was determined by sum of the cells that exceeded 6 m of drawdown. Accordingly the maximum spatial extent is limited by the size of the study area, which is 4209 km^2. The table is largely in line with our previous findings. Layers with a high magnitude of drawdown, also show the largest spatial extent of drawdown. The variation in spatial extent due to the hydraulic conductivity is in a similar way linked to the symmetry and width of the posterior hydraulic conductivity histograms.

TABLE 5.3: Maximum spatial extent of drawdown in relevant hydrogeological layers.

	Max. spatial extent (km^2)		
	LL	Median	UL
Gramercy	0	0	0
Aquitard 1	1172	145	2
Norco	3002	1404	641
Aquitard 2	3754	3516	3026
Gonzales-NO	4209	4151	3342
Aquitard 3	4209	4166	2283
1,200 foot	4209	4185	0

- **Time of maximum drawdown**
  Table 5.2 lists the year of maximum head decline. Except for the fact that the Gonzales-NO dominating layers may alternate between the years 1980 and 1970, the influence on the timing of maximum drawdown due uncertainty in hydraulic conductivity of both the aquitards and aquifers seems low.

5.1.5 Uncertainty due to geological schematization

Figure 5.6 shows the drawdown dynamics of the mean of the research area and at two locations for the three lower layers of the four-layer model. Or-42 is located in the zone of large extractions, while Or-175 is located more distant from this zone. At first sight, the differences between the uncalibrated four-layer model and calibrated eight-layer are very significant. Comparing the simulated drawdown at both locations, show that both the extent and magnitude of drawdown increased significantly. However, the timing of maximum drawdown of both models is similar. In addition, the variation due to uncertainty in the hydraulic conductivity shows to be much larger in all layers in comparison to the eight-layer model. Also the symmetry of these prediction uncertainties deviate from the results of the eight-layer model, which is probably related to different hydraulic conductivity distributions of the four-layer model.
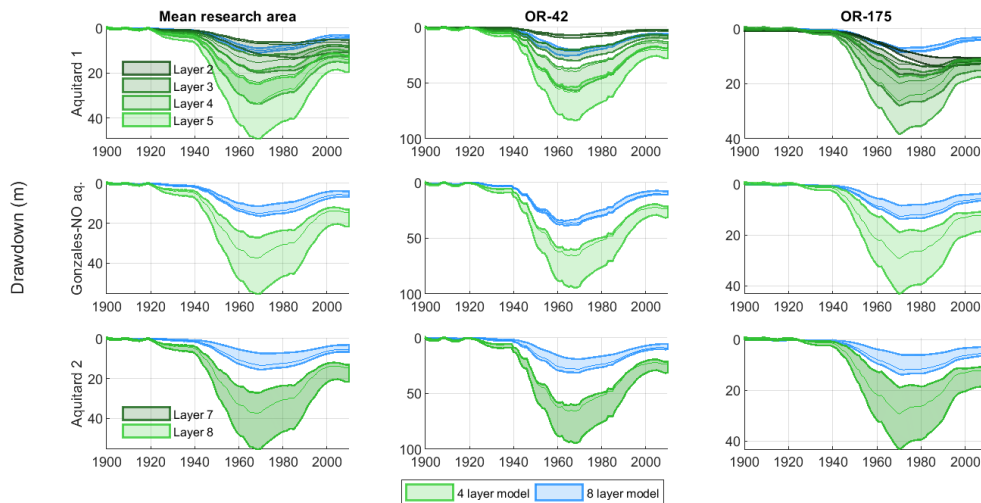
FIGURE 5.6: In green the drawdown dynamics of aquitard 1, the Gonzales-NO aquifer and aquitard 2 of the four-layer model are depicted. See Figure 5.4a for the corresponding locations. As the aquitards are composed of multiple model layers, the head dynamics of all layers are indicated. In blue the drawdown dynamics of the corresponding layers (aquitard 2, Gonzales-NO and aquifer 3 respectively) of the eight-layer model are depicted.

5.2 Land subsidence

The previous section showed that the performance of the groundwater model for the Gonzales-NO aquifer is good and for the Norco aquifer fairly good. In general, the uncertainty in hydraulic conductivity increases for the unmeasured aquifers and aquitards. Consequently these layers demonstrated a significant uncertainty in the hydraulic head predictions, mainly affecting the magnitude and spatial extent of drawdown. The simplified geological schematization affected the drawdown predictions on the same aspects. This section continues on the previous by assessing how the uncertainty in hydraulic head predictions due to both components propagates in the land subsidence predictions. However, this section starts by summarizing the key findings of the sensitivity analysis of the geotechnical parameterization, including both realistic and unrealistic parameter combinations. Subsequently, based on the selected realistic geotechnical parameter combinations the uncertainty due to the geotechnical parameterization will be assessed. Similar to the previous section, the sensitivity of the land subsidence predictions to the different type of uncertainties is evaluated against the three criteria.

5.2.1 Sensitivity of geotechnical parameters

Only the results corresponding to the OCR 1.3, 1.4 and 1.5 scenarios are considered to limit the amount of visual information. These OCR values cover a significant range of soft to rigid textures and well captures the key findings of the sensitivity analysis. The results considered in the sensitivity analysis are averaged subsidence results over the entire research area.

- **Magnitude of maximum subsidence**
  Figure 5.7 shows the maximum cumulative subsidence averaged for the entire research area for all possible parameter combinations of the recompression ratio (RR),

compression ratio (CR), secondary compression ratio (C_α) and the overconsolidation ratio (OCR). The magnitude of (maximum) subsidence shows to be very sensitive to the geotechnical parameterizations, as it ranges between 49.23 mm and 1034.0 mm for different parameter combinations. Parameter combinations that include a high value for RR, low value for CR, high value for C_α and a low value for OCR demonstrate the highest maximum subsidence, while the opposite parameter combination demonstrate the lowest maximum subsidence.
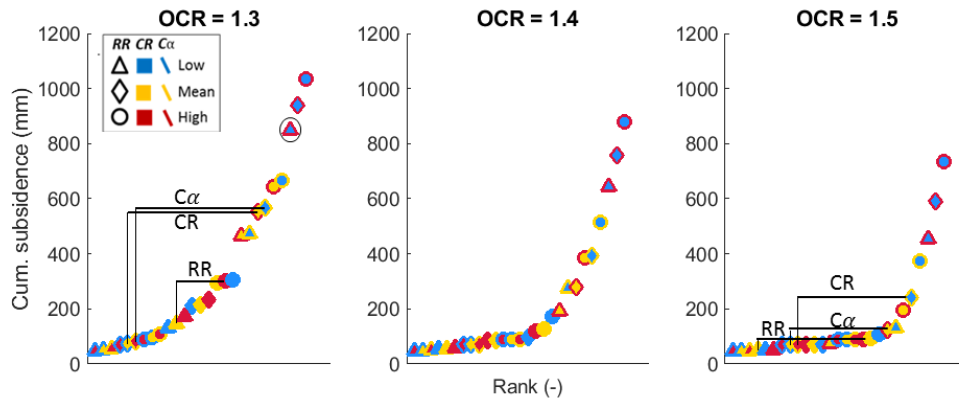

FIGURE 5.7: Magnitude of maximum subsidence averaged for the entire research area for all geotechnical parameter combinations. Shape of the point indicates the value of the recompression ratio (RR), fill of the point indicates the value of the compression ratio (CR) and outline of the point indicates the value of the secondary compression ratio (C_α). The different panels correspond with different OCR parameter values. For example the encircled point in the left most panel corresponds to a low RR value, low CR value, a high C_α value and an OCR of 1.3. All the parameter values are in agreement with the parameter values presented in Table 4.8. The black lines in the left and right panel indicate the effect of individual parameters. These lines connect points that correspond with the lowest and highest parameter values given constant values for the remaining parameters.

At the lower-left corner of the OCR 1.5 plot (right panel), a step-wise pattern can be recognized corresponding with subsidence levels of ~ 50 mm, ~ 70 mm and ~ 90 mm respectively. The difference between these levels is explained exclusively by the value of the recompressions parameter and is insensitive to the other parameters. Recall that the NEN-Bjerrum model decomposes subsidence in an elastic component, described by solely recompression ratio, and a viscous component described by all four geotechnical parameters. Consistent with this theory, the elastic component constitutes a base level of limited deformation, in this case clearly visible in the OCR 1.5 plot. Deformation that exceeds the base level of elastic deformation is of viscous origin. Although the contribution of viscous deformation may be much more significant, the figure shows that its contribution is highly variable and sensitive to all the geotechnical parameterization.

At first sight no clear distinction in most dominant geotechnical parameter with respect to the magnitude of viscous deformation emerges. As the NEN-Bjerrum model calculates viscous strain based on all four parameters, individual geotechnical parameters also control the effect of the other geotechnical parameters. To illustrate the effect of the individual parameters (RR, CR C_α) on the magntiude of viscous deformation and to show how these parameters are affected by a varying OCR, the black bars indicate the range of influence of individual parameters. For an OCR

of 1.3 the magnitude of viscous deformation is equally sensitive to CR and C_α and both parameters show to be very influential. In contrast, the magnitude of viscous subsidence is less sensitive to RR relative the other two parameters. For an OCR of 1.5 the range of influence of all three parameters declines. The magnitude of viscous deformation is in this case the most sensitive to CR, followed by C_α and RR. This example illustrates that the magnitude of (maximum) viscous deformation is dominated by the compression ratio (CR) and secondary compression ratio (C_α), but their effect is strongly controlled by the overconsolidation ratio (OCR).

- **Maximum spatial extent of subsidence**
  Figure 5.8 shows the maximum spatial extent of subsidence in the study area for all possible parameter combinations. This spatial extent was derived from the number of cells that exceeds an arbitrary subsidence value of 50 mm. Consequently, the spatial extent is limited by the size of the research area, which is equal to 4209 km^2. The variation in spatial extent of subsidence varies significantly for the different parameter combinations, as it ranges between 1885 km^2 and 4209 km^2. The latter value clearly reflects the size of the research area. Although less prominent, similar to Figure 5.7 a step-wise pattern can be recognized (indicated by arrows) in the OCR 1.5 plot, which corresponds with a spatial extent of ~ 1900 km^2, ~ 2650 km^2 and ~ 3200 km^2 respectively. Again the difference between these levels is predominantly described by the recompression ratio (RR). This illustrates that the spatial extent of subsidence is already seriously affected by solely the recompression ratio.

FIGURE 5.8: Maximum spatial extent of subsidence in the research area for all geotechnical parameter combinations. The shape of the point indicates the recompression ratio (RR), fill of the point indicates the compression ratio (CR) and the outline of the point indicates the secondary compression ratio (C_α). The different panels correspond with different OCR parameter values. The arrows in the right panel indicate the step-wise pattern that is dominated by the recompression ratio (RR).

The by elastic deformation dominated trend is less clear in the lower OCR plots. Parameter combinations that were associated with high viscous deformation, demonstrate a larger spatial extent of subsidence in comparison to equivalent parameter combinations with higher OCR values. Remarkably, a significant number of parameter combinations produce subsidence over the entire study area. This may seem unrealistic given the limited spatial extent of simulated drawdown, but it is consistent with the theory of the NEN-Bjerrum model that accounts for viscous deformation by ageing.

- **Timing of maximum subsidence**

  Figure 5.9 shows the year of maximum subsidence in the research area for all parameter combinations. All three plots show a similar tendency: maximum subsidence is modelled around either 1970 or 1985, or subsidence continues until the end of the model period (2010). Note that maximum drawdown was modelled for 1970 in the study area. Consequently all subsidence that is modelled after 1970, is of transient viscous origin, as elastic subsidence strictly follows the groundwater dynamics and is modelled instantaneously. Not surprisingly, especially geotechnical parameter combinations that were associated with high viscous deformation, show a delayed geotechnical response. Even though significant hydraulic head recovery is modelled, some parameter combinations show ongoing subsidence until 2010. This implies that the transient viscous deformation for these parameter combinations, exceeds elastic rebound over the entire period of hydraulic head recovery (40 years). Hence, these parameter combinations demonstrate unrealistically high viscous deformation. Again comparing the different OCR plots shows that OCR controls the effect of other parameters: the number of parameter combinations that demonstrate a delayed response increases for decreasing OCR values and vice versa.
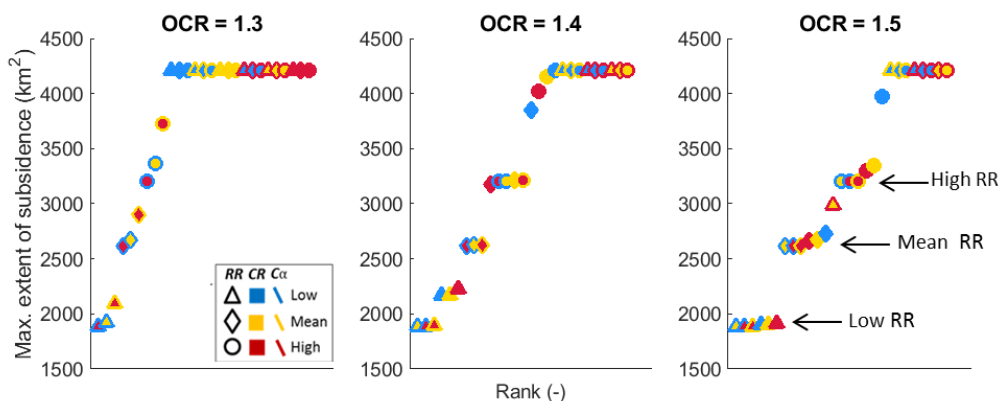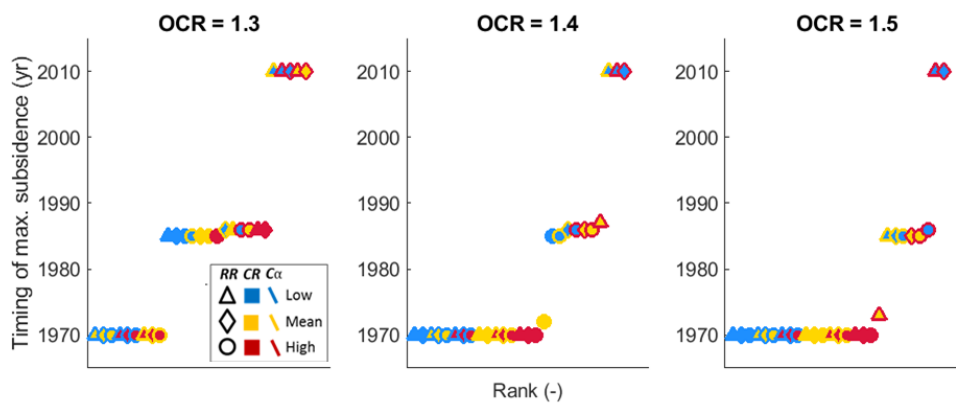

FIGURE 5.9: Year of maximum average subsidence in the research area for all parameter combinations. The shape of the point indicates the recompression ratio (RR), fill of the point indicates the compression ratio (CR) and the outline of the point indicates the secondary compression ratio (C_α). The different panels correspond with different OCR parameter values.

Land subsidence model results showed to be very sensitive on all three evaluation criteria with respect to the geotechnical parameterization. For all parameter combinations a limited amount of direct instantaneous deformation is modelled, inducing a limited but relevant amount of uncertainty with respect to magnitude and spatial extent of subsidence. In addition, for some parameter combinations transient viscous deformation is modelled, the exact contribution of viscous deformation depends strongly on the parameter combination and induces a huge uncertainty on all three evaluation aspects. The geotechnical parameterization was based on two empirical relations, which both resulted very different subsidence patterns for this study. Table 5.4 summarizes the subsidence characteristics corresponding to the parameter values established on Hough (1957) and Jafari et al. (2018). Clearly the parameterization based on Jafari et al. (2018) corresponds to relatively weak sediments producing significant viscous deformation (for an OCR of 1.3). In contrast, the

parameterization based on Hough (1957) corresponds to more rigid sediments resulting in limited viscous deformation.

TABLE 5.4: Subsidence characteristic corresponding with the parameterization based on Hough (1957) and Jafari et al. (2018)

	Hough (1957)		Jafari et al. (2018)	
	OCR 1.3	OCR 1.5	OCR 1.3	OCR 1.5
Max magnitude (mm)	131.3	49.8	301.8	90.7
Spatial extent (km^2)	4209	1905	4209	3295
Year of max. subsidence	1985	1970	1985	1970

5.2.2 Selection of realistic geotechnical parameter combinations

The way viscous deformation is incorporated in the model is arguable: a significant number of parameter combinations generates high viscous deformation over the entire study area, even at locations without significant hydraulic head decline. This type of deformation may be valid for recent deposited shallow clays, but seems unrealistic for the older aged Pleistocene clay layers as considered in this study. Therefore, parameter combinations were selected based on limited creep deformation.
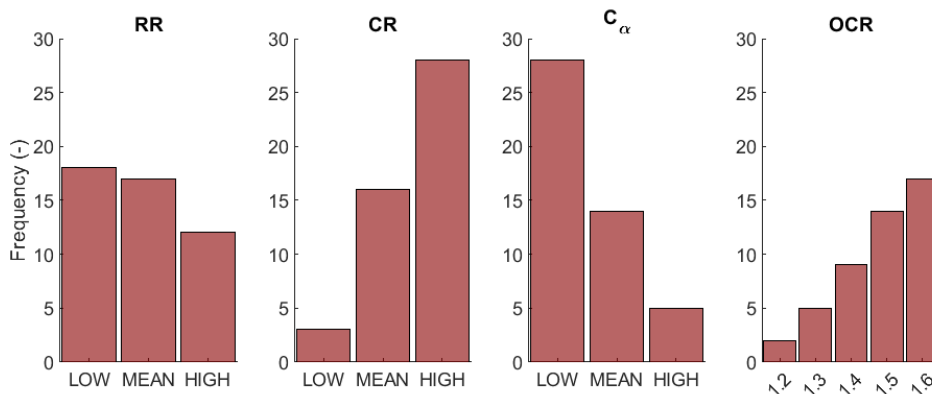
FIGURE 5.10: Frequency histograms of selected realistic geotechnical parameter combinations. The labels on the x-axis correspond to the values in Table 4.8 and are similar to the parameter values in Figure 5.7, 5.8 and 5.9.

Figure 5.10 shows the frequency histograms of the realistic geotechnical parameter combinations, which resemble a total of 47 geotechnical parameter combinations. The symmetry of the histogram is in line with the findings of the sensitivity analysis: RR and C_α are mostly represented by low values, while CR and OCR are predominantly represented by high values. These parameter configurations generally resemble more rigid sediments that are governed by a relatively low contribution of viscous deformation. Moreover the steepness of the histograms indicates the sensitivity of the individual parameters, as it reflects the number of parameters that were filtered out because of its influence on autonomous creep behaviour. Accordingly, CR and C_α are more sensitive than the RR parameter.

5.2.3 Modelled subsidence patterns

This section presents the modelled subsidence patterns of the ensemble median of all realistic geotechnical parameter combinations. The effect of uncertainties on modelled subsidence are considered in sections 5.2.4, 5.2.5 and 5.2.6 respectively. Figure 5.11a depicts the modelled subsidence for the entire research area at 1970, which is the year of maximum modelled subsidence in the research area. The contour lines in Figure 5.11a clearly demonstrate that subsidence is modelled over a significant part of the research area and increases in magnitude towards urban New Orleans and Norco. The zone of most prominent subsidence extends over entire urban New Orleans (districts: Michoud, Mid-City NO, Gentilly and Nine Mile Point), where subsidence exceeds 100 mm. The highest magnitude of subsidence is modelled in the Michoud district: ranging up to 234 mm at the Entergy facility in 1970. This location is in agreement with the location of the observed and modelled cone of depression in the Gonzales-NO aquifer and adjacent aquitards. Limited maximum subsidence of 133 mm is modelled at the industrial facilities in the Norco district for 1965. A clear correlation between the location of extraction wells and magnitude of subsidence can be recognized. However, the effect of the groundwater extractions on land subsidence is not limited to the locations of pumping, but extends over a much larger area.
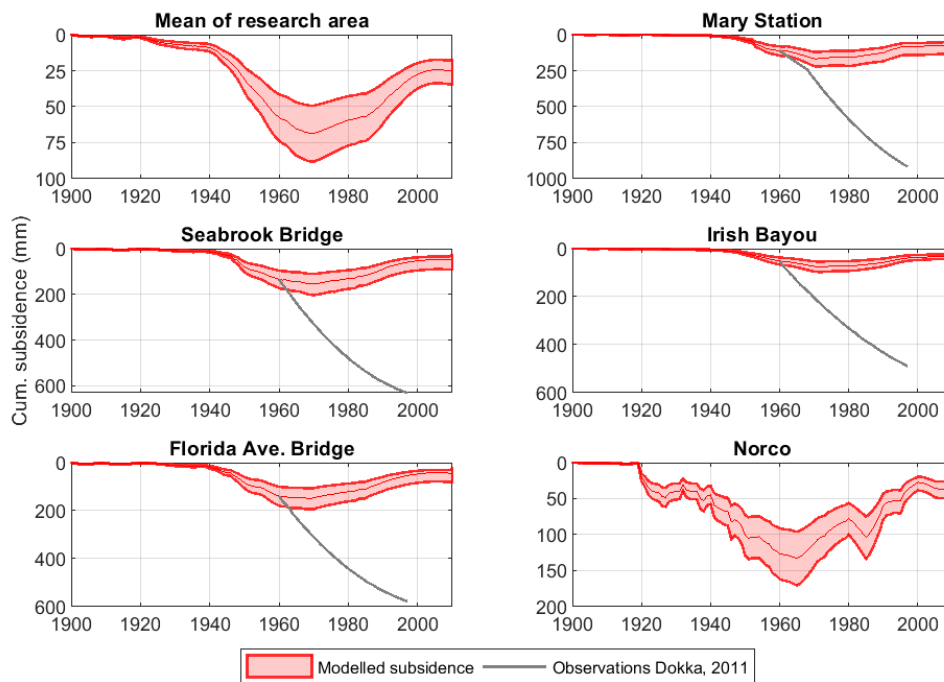
Figure 5.11b depicts the timeseries of modelled land subsidence for the entire model period, including the 95% confidence limits due to uncertainty in the geotechnical parameterization. This section concentrates on the dynamics of the timeseries of the ensemble median at different locations. The upper left panel shows the average subsidence of the entire research area: most significant subsidence is modelled before 1970, slowly initiating at 1900 and accelerating around the 1940's. Maximum average subsidence of 68.5 mm is modelled for the research area. Following 1970 significant land surface recovery is simulated: 63.5% of the initial modelled subsidence is recovered in 2010. This trend is in line with the modelled and observed hydraulic head recovery in the Norco and Gonzales-NO aquifers and implies that a significant part of the modelled subsidence is of elastic origin.

The subsidence patterns at the Mary Station, Seabrook Bridge, Irish Bayou and Florida Avenue Bridge reveal great similarities with the subsidence pattern of the mean of the research area. As those locations are most approximate to the locations of large groundwater extractions from the Gonzales-NO aquifer near Urban New Orleans (Michoud, Gentilly, Mid-City NO and Nine-Mile point), these extractions presumably dominate the subsidence dynamics in the research area. In contrast, the subsidence trend at Norco deviates from the other locations, as it shows a more erratic pattern and a different timing: maximum subsidence near Norco occurs around 1965, while maximum subsidence at the other locations occurs around 1970.

In grey the land subsidence observations of Dokka (2011) by water gauge readings from 1960 to 1997 are indicated. In order to make a fair comparison the observations have an offset equal to the median of subsidence at the corresponding location at 1961. Clearly the observed subsidence exceeds the modelled subsidence at all locations. Moreover, the observations show ongoing subsidence after 1970, while modelled subsidence exclusively demonstrates land surface recovery in the subsequent period. However, as mentioned before these observations cover the cumulative effect of subsidence processes below the
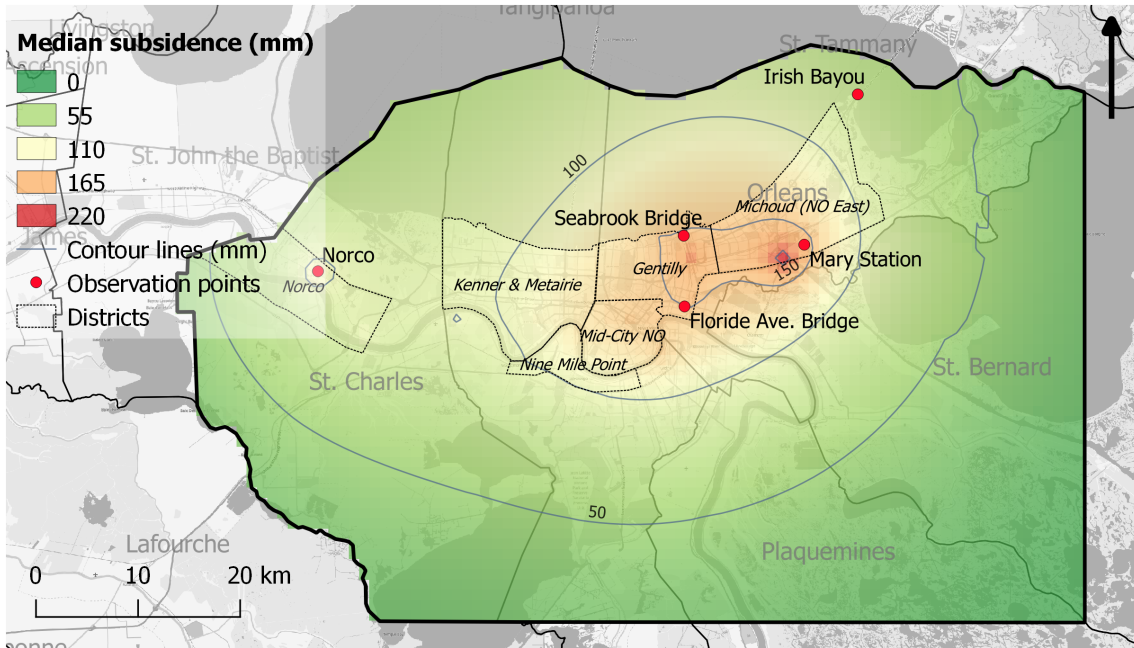
(a)

(b)

FIGURE 5.11: a) Modelled land subsidence at 1970. The figure shows the median of the land subsidence model results of the entire ensemble of realistic geotechnical parameter combinations. Contour lines have a 50 mm interval. Locations of timeseries plots are indicated by red dots. b) Timeseries of modelled subsidence for the entire model period including the 95% confidence interval due to geotechnical parameterization. The upper left plot shows the mean land subsidence in the research area. The other five plots depict subsidence at specific locations. These locations are indicated on figure a. Land subsidence observations by water gauge readings of Dokka (2011) are also plotted for the Mary Station, Seabrook Bridge, Irish Bayou and Florida Avenue Bridge from 1960 until 1997. The subsidence observations plotted at the Mary Station are the observations at the Paris Road Bridge, which is located 4.5 km west of the Mary Station.

Holocene deposits, which makes an fair comparison between observed and modelled subsidence difficult. Only the relative amount of modelled and observed subsidence between the stations is similar: Irish Bayou shows the lowest amount of subsidence both for the observations and model results, while at the Mary Station the highest amount of subsidence is modelled in line with the observations.

5.2.4 Uncertainty due to geotechnical parameterization

The sensitivity of the land subsidence model to the four geotechnical parameters was extensively evaluated in Section 5.2.1. This section contributes to the previous by addressing the uncertainty in the selected realistic geotechnical parameter combinations at multiple locations in the research area. Figure 5.11b shows the 95% confidence limits and median of the ensemble of subsidence model results for the selected realistic geotechnical parameter combinations. Table 5.5 lists the performance on the three evaluation criteria for the mean of the research area (upper-left panel) of the 2.5% confidence limit, median and 97.5% confidence limit respectively. Uncertainty in the selected geotechnical parameter combinations only affects the magnitude and spatial extent of subsidence. The variation within the subsidence distribution is (probably) dominated by the recompression ratio, as the range for the evaluation criteria shows large similarities with parameter combinations dominated by the recompression ratio as found at the sensitivity analysis (Section 5.2.1). At all locations the confidence limits have a symmetrical, distribution and the width of the confidence limits increase with the magnitude of modelled subsidence.

TABLE 5.5: Model performance due to uncertainty in geotechnical parameterization based on three evaluation criteria.

	LL	Median	UL
Max. subsidence (mm)	49.2 (-28.1%)	68.4	88.2 (29.5%)
Max. spatial extent (km^2)	1885 (-28.0%)	2618	3209 (22.6%)
Year of max. subsidence	1970	1970	1970

5.2.5 Uncertainty due to hydraulic conductivity

This section considers the uncertainty in the land subsidence predictions due to the hydraulic conductivity. The total ensemble of behavioural hydraulic conductivity parameter sets was run for a range of OCR (OCR 1.3-1.6) values to asses the influence of the hydraulic conductivity and geotechnical parameterization simultaneously. Figure 5.12 shows timeseries of the median and 95% confidence limits at five locations over the study area. In addition, the upper-left panel shows the distribution of average subsidence in the study area. As the differences between the OCR scenarios are well covered by the difference between OCR 1.3 and 1.4, only these OCR scenarios are further considered in the analysis. The performance of the model on the three evaluation criteria for the median and 95% confidence limits are listed in Table 5.6.
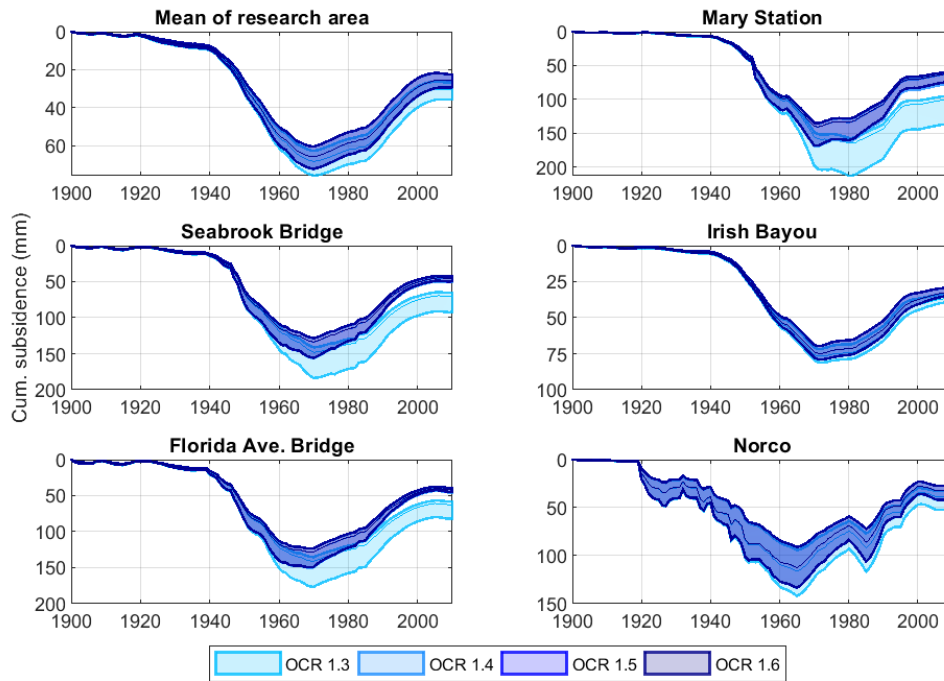
FIGURE 5.12: Timeseries of subsidence model predictions for a range of OCR value (1.3-1.6) at five locations over the study area. Both the median and 95% confidence intervals due to uncertainty in the hydraulic conductivity are indicated. The locations of the timeseries are indicated in Figure 5.11a

TABLE 5.6: Model performance due to uncertainty in hydraulic conductivity based on three evaluation criteria.

	OCR 1.3			OCR 1.4		
	LL	Median	UL	LL	Median	UL
Max. subsidence (mm)	62.8 (-8.2%)	68.4	75.9 (11.0%)	60.5 (-8.3%)	66.0	72.4 (9.7%)
Max. spatial extent (km^2)	2468 (-9.3%)	2720	2962 (8.9%)	2409 (-9.3%)	2657	2893 (8.9%)
Year of max. subsidence	1970	1970	1970	1970	1970	1970

- **Magnitude of maximum subsidence**

  According to Table 5.6 uncertainty in the hydraulic conductivity affects the subsidence prediction in the order of 10 % almost equally towards both confidence intervals. However, Figure 5.12 shows that both the width and symmetry of the confidence limits of the subsidence predictions vary over space and time. In general, the width of the prediction uncertainty decreases for decreasing modelled subsidence (over time) and likewise for increasing OCR values. Figure 5.13 depicts the prediction uncertainty of the study area averaged compression signal of individual layers for the OCR 1.4 model. As these prediction uncertainties were determined for each layer over all 31 models, the cumulative prediction uncertainty of the individual layer

does not equal the prediction uncertainty of the total subsidence signal. Instead the figure shows the influence of the hydraulic conductivity distributions on the deformation of the individual layers. Clearly, the contribution to the cumulative subsidence signal of aquitards is much higher than the contribution of aquifers. The symmetry of the confidence intervals of the different layer are in agreement with the symmetry of the drawdown distributions, which largely follow the hydraulic conductivity distributions. The high uncertainty in aquitard 1 stands out, as the hydraulic conductivity of this layer was not included in the calibration procedure of the hydraulic conductivity. As the confidence interval of the Norco aquifer has an fairly identical symmetry, presumably the uncertainty in the hydraulic head predictions of the Norco aquifer propagates into aquitard 1. Moreover, the contribution of aquitard 1 is relatively high, while the drawdown was shown to be limited. As the geotechnical parameterization is related to burial depth, sediments of the relatively thin buried aquitard 1 are more compressible.
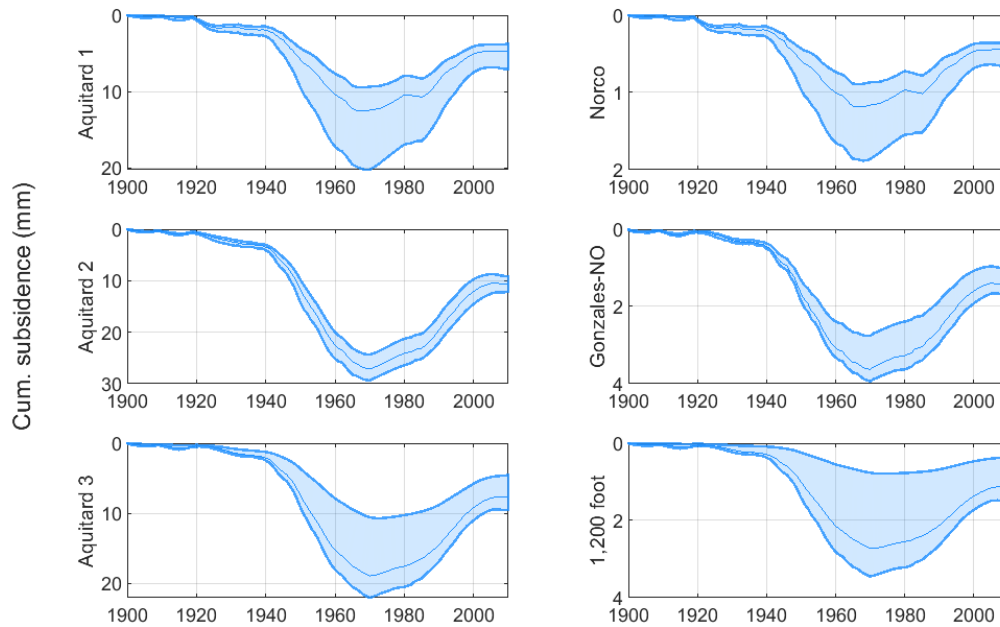
FIGURE 5.13: Average compression of individual layers in the research area for the OCR 1.4 scenarios.

- **Maximum spatial extent of subsidence**
  Table 5.6 lists the maximum spatial extent of subsidence in the study area for the median and 95% confidence limits. Model cells were classified as subsiding, if the cumulative subsidence in a cell exceeded an arbitrary value of 50 mm. The uncertainty in hydraulic conductivity affects the maximum spatial extent of the subsidence prediction about 10% towards both confidence limits.

- **Timing of maximum subsidence**
  Table 5.6 lists timing of maximum subsidence in the study area for the median and 95% confidence limits. The table and also Figure 5.12 shows that the moment of maximum subsidence is not affected by the uncertainty in hydraulic conductivity.

This is consistent with the previous findings that showed that timing of maximum drawdown is not affected by uncertainty in the hydraulic conductivity.

This section showed, in line with the findings of the sensitivity of simulated drawdown to uncertainty in hydraulic conductivity, that both the extent and magnitude of maximum subsidence is significantly affected by uncertainty in the hydraulic conductivity. However, the induced uncertainty by hydraulic conductivity is minor relative to the uncertainty induced by the geotechnical parameterization.

5.2.6 Uncertainty due to geological schematization

Figure 5.14 depicts the cumulative subsidence signals as modelled by the four-layer model averaged for the study area and at three locations over the study area, both distant (Irish Bayou) and approximate (Norco and Mary Station) to large extractions. The left panel shows that the simulated subsidence of the four-layer model exceeds the magnitude of simulated subsidence of the eight-layer model. Consequently, the spatial extent of subsidence is also significantly affected. The moment of maximum subsidence is not affected. Comparing the different locations shows that the relative amount of modelled subsidence is consistent with the predictions of the eight-layer model. The symmetry of the land subsidence prediction distributions at the different locations deviates from the eight-layer model, but is in agreement with the symmetry of the hydraulic head predictions of the four-layer model.
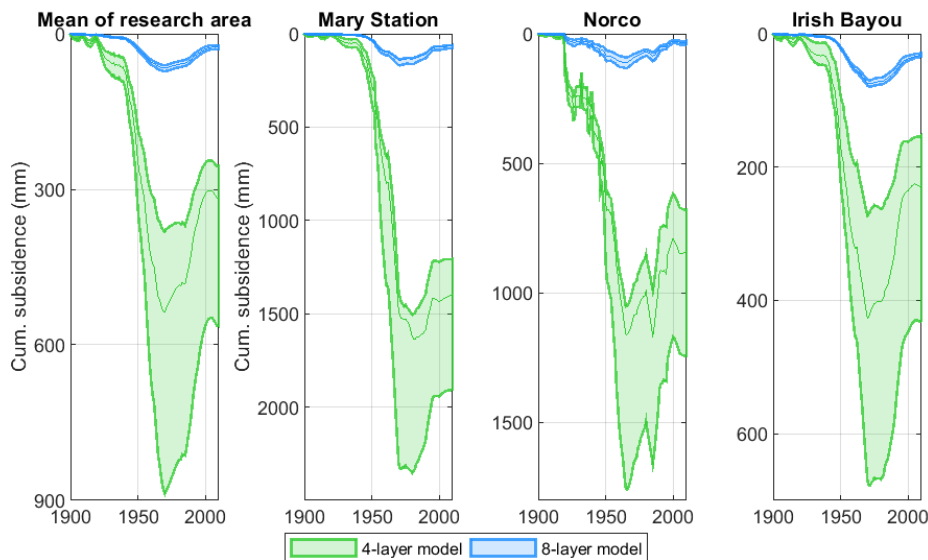

FIGURE 5.14: In green, the cumulative subsidence signal for the four-layer model at three location over the study area (see Figure5.11a) and averaged for the study area is depicted. In blue, the cumulative subsidence signal for eight-layer model is depicted.

6 Discussion

6.1 Model performance

Modelled drawdown induced by groundwater extractions simulated significant land subsidence in the study area. Major industrial groundwater extractions in the Gonzales-NO aquifer around urban New Orleans, dominated the (modelled) land subsidence in the study area. Additionally, industrial groundwater extractions in the Norco aquifer at the Norco district induced land subsidence to a more limited extent. Although, the modelled hydraulic head dynamics of both aquifers reproduced the observed hydraulic head reasonably, the results showed that the subsequent modelled land subsidence poorly match the (limited) cumulative land subsidence observations of Dokka (2011). This section will discuss the performance of the land subsidence predictions more extensively in the context of land subsidence observations of Dokka (2011) and Jones et al. (2016). This section mainly addresses (modelled) subsidence at the Mary Station, as the land subsidence observations are most extensive at this location. Both the simulated subsidence rates of the distribution of realistic geotechnical parameter combinations and the observed subsidence rates of Dokka (2011) and Jones et al. (2016) are depicted by Figure 6.1.

The InSAR study of Jones et al. (2016) provides spatially the most comprehensive picture of subsidence rates in the study area. Drawbacks of this study are that it considers cumulative deformation by multiple mechanisms between 2009-2012 at the end of our model period. Jones et al. (2016) identified average subsidence rates of 25-30 mm/yr at the Michoud Entergy Power Plant and 50 mm/yr at chemical industry further east at Michoud. Additionally, they observed subsidence rates up to 40 mm/yr at the industrial facility at Norco, predominately on the west Bank of the Mississippi river. Jones et al. (2016) discuss these exceptionally high subsidence rates in the context of groundwater extractions from the Gonzales-NO and Norco aquifer (see section 3.4). The indicated locations by Jones et al. (2016) are consistent with the predicted locations of severe subsidence by this study. However, as depicted in Figure 6.1, the timing of the high subsidence rates observed by Jones et al. (2016) are not supported by the model results, which demonstrate no subsidence at these locations for this period (2009-2012) at all.

The subsidence observations of Dokka (2011) cover a relatively large period and focus on compaction that occurred below Holocene deposits. The geodetic leveling data demonstrated average subsidence rates at the Mary Station of 13.5 mm/yr between 1955-69 and 16 mm/yr between 1969-77 (see Figure 6.1). For the same periods, this study produced average subsidence rates of 5.8 mm/yr and 0.66 mm/yr (median of ensemble of geotechnical runs), which indicates both a mismatch in trend and magnitude.
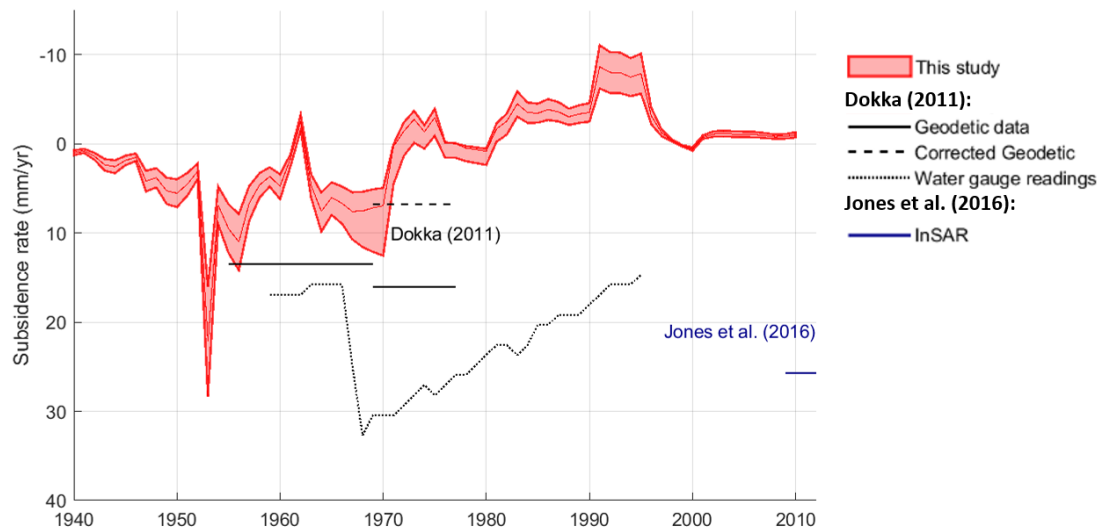
FIGURE 6.1: Distribution of subsidence rates at the Mary Station for the total ensemble of realistic geotechnical parameter model runs. Observed subsidence rates determined for the Mary Station by Dokka (2011) and Jones et al. (2016) are indicated. Note that the subsidence rates derived from water gauge readings were obtained at the Paris Road Bridge. The observations from this station were assumed to be representative for the conditions at the Mary Station, as this bridge is approximate to the location of the Mary Station.

The subsidence rates derived by Dokka (2011) from water gauge readings at the Paris Road Bridge are also plotted in Figure 6.1. As this bridge is located only 4.5 km west of the Mary Station, the subsidence rates are assumed to be representative for the Mary Station. The observed signal demonstrates a fairly constant subsidence rate of 16 mm/yr from 1959 until 1966, followed by rapid acceleration between 1966 and 1968, exceeding rates of 30 mm/yr that slowly return to the former subsidence rate. Again these rates poorly match the magnitude and timing of modelled subsidence rates: the modelled subsidence rates peak in 1953, while the observed vertical velocities are significantly higher and peak later in 1968.

Comparing the land subsidence observations by Dokka (2011) and Jones et al. (2016) with the modelled land subsidence rates of this study, clearly illustrates that the magnitude of observed land subsidence rates is structurally higher than modelled subsidence rates. Moreover, ongoing subsidence after the moment of maximum drawdown in 1970 as demonstrated by the observations, is not shown by the model. The discrepancy between model results and the observed subsidence by Dokka (2011) can be attributed to different factors, including:

- **Uncertainty of the land subsidence observations**
  The land subsidence observations are governed by a significant uncertainty itself. Especially, the contribution of deep subsidence processes below the vertical extent of the New Orleans aquifer system in the observations is unclear. For example, Dokka (2011) measured an average subsidence rate of 9.5 mm/yr at a 2000 m depth founded waste well at the Mary Station from 1969 until 1995. Dokka (2011) ascribes

this deep-subsidence rate to renewed tectonic activity of the Michoud fault. The activity of this fault would imply that compaction of the New Orleans aquifer system comprises only 6.75 mm/yr for 1969-77 (based on geodetic data). This corrected subsidence rate is also indicated in Figure 6.1 and shows to be more in line with the simulated subsidence rates. However, the revival and period of activity of this fault are uncertain. GPS measurements at the Mary Station from 2009 until 2012, indicate an average subsidence rate of 1.3 mm/yr at a depth of 2000 m (Jones et al., 2016). This rate corresponds well to the rate of Pleistocene basement subsidence as modelled by study of Wolstencroft et al. (2014) and does not provide any evidence for the revival of this fault.

- **Erroneous groundwater extractions**
  The groundwater extractions largely determine the (simulated) drawdown patterns and subsequent (simulated) land subsidence. The extractions as implemented in this study have a high spatial resolution, but the temporal resolution of the extraction yields may be erroneous as the documentation about historical extractions was limited. For example Dokka (2011) relates the accelerated subsidence mid-1968 demonstrated by the water gauge readings, to the initiation of the last and largest generator at the Entergy power plant and/or the completion of a large drink water well at Michoud. In contrast, the model results show only such a peak in subsidence rates for the general start-up of the groundwater extractions of the Entergy facility at Michoud in 1953 (see Figure 6.1). The relatively low temporal resolution of the groundwater extractions, as used in this model, may not capture these specific and local details.

- **Epistemic uncertainty**
  The discrepancy can be explained by parametric and structural uncertainty in the model set-up. Despite this study accounted for the uncertainty of main model component, the range of realistic model results still significantly deviates from the land subsidence observations, see Figure 6.1. Section 6.3 discusses the implications of epistemic uncertainty on the model predictions for the study area.

6.2 Sensitivity of land subsidence predictions

This section discusses the key findings of the sensitivity analysis to the effects of epistemic uncertainty in the geological schematization and corresponding parameterization of the hydraulic conductivity and geotechnical parameters on land subsidence model predictions.

6.2.1 Hydraulic conductivity

Model calibration (PEST) and uncertainty estimation (GLUE) were combined using hydraulic head observations to select behavioural hydraulic conductivity parameter sets. This procedure showed to be effective for the densely measured Gonzales-NO aquifer, generating a narrow hydraulic conductivity distribution. Consequently, the hydraulic head predictions were accurate with respect to hydraulic head observations and demonstrated a small prediction uncertainty. Despite the tight cutoff threshold of GLUE (1%), the hydraulic conductivity distributions of the less measured Norco aquifer, unmeasured aquitards and

1,200 foot aquifer demonstrated a higher uncertainty. The symmetry and width of the hydraulic head predictions reflect the uncertainty in the hydraulic conductivity distribution of the layer itself or/and an adjacent aquifer. The uncertainty in the hydraulic head conductivity predominantly affect the hydraulic head predictions with respect the spatial extent and magnitude of drawdown. Despite a significant range of hydraulic conductivity values was covered by this study, the hydraulic head predictions demonstrated no significant variation in time to drawdown. This is in contrast with other studies that suggest that the hydraulic conductivity of aquitards also affect the time to drawdown in the adjacent aquifer (Turnadge et al., 2018; Zhou et al., 2013). The absence of the hydrodynamic delay in the present study may be related to the rough vertical and time discretization applied in this study, which induces large vertical hydraulic head gradients between layers and stimulates unrealistically rapid response times.

The uncertainty in hydraulic head predictions propagated significantly into the land subsidence predictions. Similar to the hydraulic head predictions, the uncertainty in hydraulic conductivity affected predominantly the magnitude and spatial extent of subsidence predictions. Consistent with their compressible nature, uncertainty in the hydraulic conductivity of aquitards contributed to a greater extent to the total land subsidence prediction uncertainty relative to aquifers.

6.2.2 Geological schematization

Model predictions of the simplified four-layer geological schematization strongly deviate from the eight-layer geological schematization. The modelled drawdown by the four-layer model exceeds the modelled drawdown by the eight-layer model both in magnitude and extent. Subsequent subsidence predictions showed a similar increase in magnitude and extent of subsidence. It is difficult to disentangle the different causes for the described discrepancy between both models, as the subsidence results of the eight-layer model are based on calibrated hydraulic conductivity values in contrast to the results of the four-layer model. However, as the geological structure controls the continuity and interconnectivity of aquifer systems (Martin & Frind, 1998), the increase in thickness of the upper aquitard presumably decreases the groundwater recharge to deeper layers, stimulating excessive drawdown and subsequent subsidence. Moreover, as the geological schematization determines the distribution of compressible clays (Erkens et al., 2015), the increase in aquitard thickness increases the amount of compressible material.

6.2.3 Geotechnical parameterization

The sensitivity of the land subsidence predictions was assessed by running a range of geotechnical parameter combinations, that were determined based on empirical relations between soil properties and geotechnical parameters. Consistent with the mathematical formulation of the NEN-Bjerrum model (Kooi et al., 2018), a clear distinction could be made between the behaviour of elastic and viscous deformation. Elastic deformation demonstrated to be solely sensitive to the recompression parameter and induced a relatively limited uncertainty regarding the magnitude and spatial extent of subsidence. The amount of elastic deformation increases with increasing values for the recompression parameter. In

contrast, viscous deformation demonstrated to be very sensitive to all four geotechnical parameters, inducing a substantial uncertainty in the magnitude, spatial extent and timing of subsidence. Relatively low values for the recompression and secondary compression parameter in combination with relatively high values for the compression parameter correspond to a rigid underground, which is insensitive to subsidence. The opposite parameterization reflects a weak underground, which is sensitive to subsidence. The overconsolidation ratio amplifies or diminishes the effect of the other parameters with respect to modelled viscous deformation. The observed effect of the overconsolidation ratio is in agreement with the study of Minderhoud et al. (2017), which used this parameter to calibrate modelled subsidence against observed subsidence. However, the present study demonstrated that the other geotechnical parameters may affect the magnitude of viscous deformation similarly. Hence, a proper fundamental basis for the geotechnical parameterization is preferred over model calibration using the overconsolidation ratio, as the parameterization not only affects the magnitude of subsidence, but also the spatial extent and timing of subsidence.

As viscous deformation is modelled by the NEN-Bjerrum model as a time-dependent process, autonomous creep may accumulate with time regardless of the magnitude of drawdown. Given the geological development of the aquifer system (see section 3.2), high autonomous background creep was assumed to be unrealistic in this at present aged Pleistocene aquifer-system. Therefore, a set of geotechnical parameter combinations were selected based on realistic compaction behaviour, rather than on their performance with respect to land subsidence observations. The corresponding land subsidence predictions are dominated by elastic deformation and predominantly sensitive to the recompression parameter regarding the magnitude and spatial extent of subsidence.

6.3 Implications for the Greater New Orleans area

This section combines the previous sections to discuss the discrepancy between land subsidence observations and model results in the context of epistemic uncertainty. Land subsidence observations and model predictions deviate regarding both the magnitude and timing of subsidence. Hydraulic conductivity, geological schematization and geotechnical parameterization all showed to affect the magnitude of simulated subsidence. However, as the uncertainty analysis covered a significant range of realistic hydraulic conductivity values, the uncertainty in hydraulic conductivity is not expected to explain the current discrepancy in magnitude. Also, the uncertainty in the geological schematization is not expected to explain the discrepancy, as the hydraulic head predictions of the calibrated eight-layer groundwater model performed reasonably well regarding hydraulic head observations. Nonetheless, the geological schematization may affect the land subsidence predictions by an erroneous distribution of compressible material.

The largest uncertainty with respect to magnitude of subsidence is expected to stem from the geotechnical parameterization. The sensitivity analysis showed that the magnitude of subsidence is very sensitive to the geotechnical parameterization. Due to the lack of data to properly constrain the geotechnical parameters and the limited number of land subsidence observations in the study area, the geotechnical parameter combinations were

selected based on realistic deformation behaviour (i.e. no high rates of autonomous background creep). However, similar aged and stable Pleistocene settings have demonstrated significant deformation by creep after human intervention, which challenges the applied selection criteria. For example, the construction of Kansai Airport off the coast of Japan, induced significant creep in the Pleistocene clay layers (Mesri & Funk, 2014). Hence, significant viscous deformation itself is not unrealistic in this study area. However, the way that the NEN-Bjerrum model incorporates viscous deformation may not be most appropriate for this study setting, as viscous deformation accumulates over the entire study area regardless of the drawdown corresponding to the deformation behaviour of younger depositions. Nevertheless, without information about the actual geotechnical parameterization or high quality land subsidence observations, the proper deformation behaviour of this setting remains unclear.

The described discrepancy in timing of modelled subsidence is most likely to stem from epistemic uncertainty in the hydrogeology and geotechnical parameterization. Although the former was not demonstrated in this study, the delayed response of aquitards due to slow dissipation of excess pore pressure have shown to be of a significant order in other studies with similar settings (Zhou et al., 2013). Hence, the absence of ongoing modelled subsidence after the moment of maximum drawdown, as was shown by the observations of Dokka (2011) and Jones et al. (2016), may be related to either the low contribution of transient viscous deformation or the rough discretization of aquitards in this study (Kooi et al., 2018).

To better illustrate the effect of unrealistic and realistic geotechnical parameter combinations, the model run, which demonstrated the highest correlation with the observations of Dokka (2011) at the Mary Station, is selected out of the entire ensemble geotechnical runs. The corresponding subsidence rate and cumulative subsidence signal of this run are shown in purple by Figure 6.2. Despite the discrepancy between observed and modelled rates is still considerable, at the moment of maximum drawdown the modelled and observed rates are within the same order of magnitude. Hence, this 'unrealistic' run approaches the observed subsidence rates much closer than the best estimate model of realistic runs (in red). Moreover, subsidence continues up to 15 years after the groundwater low-stand, which is in better agreement to the observed subsidence signal at Paris Road Bridge (water gauge readings) (Dokka, 2011). However, even though the OCR of 1.3 of this 'unrealistic' run is not unrealistically low in comparison to similar studies (Bakr, 2015; Minderhoud et al., 2017), significant modelled subsidence accumulates ahead of the initiation of the large groundwater extractions at the Mary Station (see lower panel of Figure 6.2. Ultimately, this result in 'autonomous' creep exceeding 200 mm in the entire research area, which is very unrealistic in this at present aged setting.

In contrast to the observations of Dokka (2011), the observed subsidence rates by Jones et al. (2016) in 2009-2012 are impossible to explain on the basis of solely model uncertainties. Moreover, these high observed rates are unlikely to contain a large contribution of deformation induced by extractions from the Gonzales-NO, as they occur 40 years after the observed moment of maximum drawdown in the Gonzales-NO aquifer. Remarkably, the observed locations of serious subsidence by Jones et al. (2016) are consistent with both the present study and the locations of large industrial groundwater extractions. Hence,
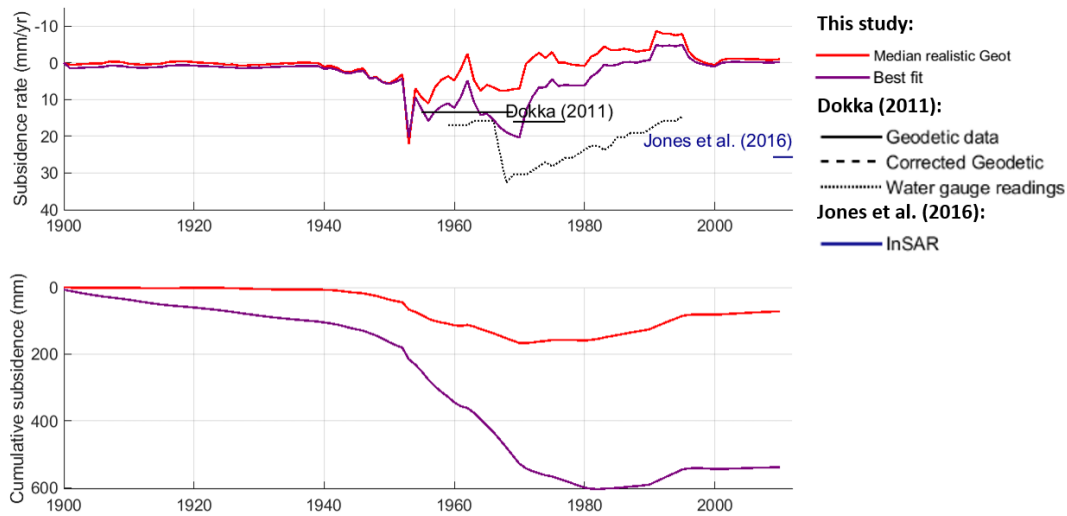
FIGURE 6.2: Upper panel: In red the median of subsidence rates at the Mary Station for the total ensemble of realistic geotechnical parameter model runs. In purple the subsidence rates of an 'unrealistic' run are plotted. This run demonstrates the highest correlation with the land subsidence observations of Dokka (2011). This run has the following geotechnical parameter combination: low RR, high CR, high C_α and OCR 1.3. Observed subsidence rates determined for the Mary Station by Dokka (2011) and Jones et al. (2016) are also indicated. Lower panel: cumulative subsidence for the both the median of ensemble of realistic geotechnical parameter runs (red) and best performing run (purple).

other subsidence processes may be induced by the industrial facilities at these locations, e.g. unreported groundwater processes at lower depth, but further research needs to be carried out to better explain these high observed subsidence rates.

Despite the significant influence of the hydraulic conductivity and geological schematization on the modelled land subsidence results, this section showed that the uncertainty in geotechnical parameterization is presumably the main cause of the large differences between modelled and observed subsidence. In order to make more reliable subsidence predictions in the study area, either a better description of the geotechnical properties or high quality land subsidence observations are required. The latter can be used for model calibration adjusting the geotechnical parameters. Moreover, also the type of land subsidence model should be chosen based on the geological setting. The NEN-Bjerrum model showed not to be able to simulate a realistic amount of subsidence without producing significant background creep over the entire study area. Other land subsidence models might be more appropriate to model subsidence in at present aged settings.

6.4   Recommendations

Based on the findings of this study, the following recommendations should be considered when modelling land subsidence at a regional scale:

1. Provide a fundamental base for the geotechnical parameterization if subsidence observations are absent. This studied showed that the amount of subsidence is very sensitive to all four geotechnical parameters. Adjusting the OCR value to calibrate

simulated subsidence against observed subsidence, may be effective as it greatly determines the effect of all parameters. However, such a procedure only affects the contribution of viscous deformation to the total deformation. Hence, a proper fundamental base of the geotechnical parameter is required to make realistic subsidence predictions with respect to magnitude, timing and spatial extent.

2. Provide an accurate groundwater model with a site specific hydraulic parameterization. Both the sensitivity analysis to the hydraulic conductivity and geological schematization showed that subsidence predictions rely significantly on the modelled hydraulic head dynamics. Model calibration against observed hydraulic head observations, may be a useful first step in compensating for epistemic uncertainty. However, this procedure showed mainly to be effective for measured aquifers. When no hydraulic head information is available a proper parameterization is required to provide accurate subsidence results.

This study made a first step in evaluating the sensitivity of land subsidence predictions to structural and parametric uncertainties. The following work needs still to be done:

- Investigate the sensitivity of the land subsidence predictions to structural uncertainty by comparing model predictions of different calibrated groundwater models corresponding to different interpretations of the geology. This study compared the results of an calibrated and uncalibrated model corresponding to two different geological interpretations. Hence, we were not able to distinguish how uncertainty in the geological schematization affects the land subsidence predictions by either the hydrogeoglogy or spatial distribution of compressible material.

- Investigate the sensitivity of land subsidence predictions of sufficiently discretized aquitards to the hydraulic conductivity. An insufficient discretization of the aquitards potentially led to unrealistic response times of aquitards as shown in this study. Hence, the role of parameterization of aquitards needs to be further investigated.

- Investigate the influence of surface hydrology on land subsidence predictions. Although, some studies have shown that parameters as recharge may influence head dynamics, the influence of these aspects were ignored in this study.

- Revise the way the NEN-Bjerrum model accounts for deformation by creep. Currently, to model significant (realistic) viscous deformation, additional high autonomous background creep is generated over the entire model domain. This may result in unrealistic subsidence predictions for aged settings. To well account for creep deformation in subsidence models for such settings, ideally deformation by creep due to aging should only be active, once triggered significantly by a hydraulic head decline.

7 Conclusions

The effects of epistemic uncertainty in the geological schematization and corresponding parameterization of both the hydraulic conductivity and geotechnical parameters on land subsidence model predictions were studied based on a land subsidence model of the New Orleans aquifer system. Land subsidence driven by historical groundwater extractions in the Greater New Orleans area, was modelled transiently from 1900 to 2010 using a one-way coupled hydrogeological subsidence model. The NEN-Bjerrum viscoelastic model was used to calculate subsidence, as this model accounts better for deformation by creep.

Parameter calibration (PEST) and uncertainty estimation (GLUE) were combined using USGS hydraulic head observations to find statistically well performing hydraulic conductivity distributions. These distributions were used to asses the effects of hydraulic conductivity on the land subsidence prediction uncertainty. The uncertainty in hydraulic head predictions was small for the densely measured Gonzales-NO aquifer. In contrast, the uncertainty of the hydraulic head predictions for the less measured or unmeasured aquifers and aquitards was relatively high. Consequently, the subsequent land subsidence model predictions demonstrated to be clearly affected by the uncertainty in hydraulic head prediction with respect to both the magnitude and spatial extent of modelled subsidence. Consistent with their compressible nature, uncertainty in the hydraulic conductivity of aquitards contributed to a greater extent to the total land subsidence prediction uncertainty relative to aquifers.

The hydraulic head and land subsidence predictions of the calibrated eight-layer groundwater model were compared with the model predictions of a simplified uncalibrated four-layer groundwater model to asses the influence of the geological schematization. The four-layer model simulated significantly more drawdown and subsidence in comparison to the eight-layer model. The differences between both models is presumably caused by the larger cumulative aquitard thickness in the four-layer model relative to the eight-layer model, which increases the magnitude of drawdown due to reduced groundwater recharge to lower layers and increases the amount of high compressible material. This example demonstrates the large dependency of subsidence models on reliable hydraulic head predictions. Consequently, model calibration against hydraulic head observations should be performed, when when using a simplified geological representation of an aquifer system, to get reliable subsidence predictions.

Running a wide range of geotechnical parameter combinations demonstrated that the land subsidence predictions were very sensitive to all four geotechnical parameters of the NEN-Bjerrum model: the recompression ratio, compression ratio, secondary compression ratio

and overconsolidation ratio. A clear distinction between the behaviour of elastic and viscous deformation was observed. Elastic deformation is solely sensitive to the recompression parameter and affects the model predictions with respect to the magnitude and spatial extent of subsidence. In contrast, viscous deformation is very sensitive to all four geotechnical parameters and affects land subsidence predictions regarding the magnitude, spatial extent and timing of subsidence. Model results of some geotechnical parameter combinations suggested that significant subsidence accumulated over the entire study area. Although consistent with the approach of the NEN-Bjerrum model, these high autonomous creep rates were considered to be unrealistic in the at present aged study setting. Therefore, realistic geotechnical parameter combinations, demonstrating limited autonomous creep, were selected among the ranges of empirically established geotechnical parameters. The selected geotechnical parameter combinations were used to make realistic simulations for historical land subsidence in the study area.

The best estimate model suggests that the groundwater extractions induced mean cumulative subsidence of 68.5 mm in the study area by 1970, which is the moment of maximum subsidence. Hereafter, the model results indicate significant rebound of the land surface. Maximum cumulative subsidence of 234 mm at Michoud in 1970 and 133 mm at Norco in 1965 is shown by the model. Although those locations correlate well with the locations as indicated by the observations in the study area, generally the model results poorly match the observations. Simulated subsidence is significantly smaller and of shorter duration in comparison to the observations. Besides the uncertainty in the land observations itself, epistemic uncertainty is likely to have contributed significantly to the determined discrepancy between model results and observations.

Despite the significant influence of the hydraulic conductivity and geological schematization on land subsidence model predictions as shown by this study, the uncertainty in geotechnical parameterization is presumably the main cause of the discrepancy between model results and observations. Due to the lack of data to constrain the geotechnical parameters and the limited number of land subsidence observations in the study area, the geotechnical parameterization was solely based on realistic deformation behaviour. However, none of the selected parameter combinations was able to reproduce the subsidence observations. In contrast, subsidence predictions using unrealistic geotechnical parameter combinations better approached the observed subsidence rates, but also demonstrated significant autonomous creep over the entire study area. Hence, in order to make more reliable subsidence predictions in the study area, either a better description of the geotechnical properties or high quality land subsidence observations are required, which can be used for model calibration. Moreover, the type of land subsidence model should be chosen based on the geological setting.

Based on this study one can conclude that the groundwater extractions in the Norco and Gonzales-NO aquifers contributed to historical land subsidence in the Greater New Orleans area. The observed subsidence rates at Michoud by Dokka (2011) may contain a significant contribution of land subsidence induced by the industrial groundwater extractions from the Gonzales-NO aquifer. Although, the observed locations of serious subsidence by Jones et al. (2016) are consistent with the present study, the high subsidence rates in 2009-2012 were not supported by the model results. Hence, other subsidence processes may be induced by

the industrial facilities at these locations, e.g. unreported groundwater processes at lower depth, but further research needs to be carried out to better explain these high observed subsidence rates.

Bibliography

Abelev, M. Y., & Tsytovich, N. (1964). Problems of application of the theory of consolidation for fully saturated clayey soils. *Soil Mechanics and Foundation Engineering*, *1*(3), 158–163.

Andreadis, K. M., Schumann, G. J.-P., & Pavelsky, T. (2013). A simple global river bankfull width and depth database. *Water Resources Research*, *49*(10), 7164–7168.

Bakr, M. (2015). Influence of groundwater management on land subsidence in deltas. *Water resources management*, *29*(5), 1541–1555.

Beigi, E., & Tsai, F. T.-C. (2015). Comparative study of climate-change scenarios on groundwater recharge, southwestern mississippi and southeastern louisiana, usa. *Hydrogeology Journal*, *23*(4), 789–806.

Beven, K., & Binley, A. (1992). The future of distributed models: model calibration and uncertainty prediction. *Hydrological processes*, *6*(3), 279–298.

Bieber, P., & Forbes, M. (1966). Pumpage of water in louisiana, 1965. Tech. rep., State of Louisiana Department of Conservation Geological Survey & Department of Public Works.

Biot, M. (1941). General theory of three-dimensional consolidation. *J. Appl. Phys.*, *12*, 155–164.

Bjerrum, L. (1967). Engineering geology of norwegian normally-consolidated marine clays as related to settlements of buildings. *Geotechnique*, *17*(2), 83–118.

Blasone, R.-S., Vrugt, J. A., Madsen, H., Rosbjerg, D., Robinson, B. A., & Zyvoloski, G. A. (2008). Generalized likelihood uncertainty estimation (glue) using adaptive markov chain monte carlo sampling. *Advances in Water Resources*, *31*(4), 630–648.

Cardwell, G., & Walter, W. (1979). Pumpage of water in louisiana, 1975. Tech. rep., United States Department of the Interior Geological Survey.

Carrera, J., Alcolea, A., Medina, A., Hidalgo, J., & Slooten, L. J. (2005). Inverse problem in hydrogeology. *Hydrogeology journal*, *13*(1), 206–222.

Chamberlain, E. L., Hanor, J. S., & Tsai, F. T.-C. (2013). Sequence stratigraphic characterization of the baton rouge aquifer system, southeastern louisiana. *Gulf Coast Association of Geological Societies Transactions*.

Cherry, J., Parker, B., Bradbury, K., Eaton, T., Gotkowitz, M., Hart, D., & Borchardt, M. (2004). Role of aquitards in the protection of aquifers from contamination: a "state of the science" report. *AWWA Research Foundation, Denver, CO*.

Coleman, J. M., & Roberts, H. H. (1988). Sedimentary development of the louisiana continental shelf related to sea level cycles: Part i—sedimentary sequences. *Geo-Marine Letters*, *8*(2), 63–108.

Coleman, J. M., Roberts, H. H., & Stone, G. W. (1998). Mississippi river delta: an overview. *Journal of Coastal Research*, (pp. 699–716).

Craig, N., Turner, R., & Day, J. W. (1979). Land loss in coastal louisiana (usa). *Environmental Management*, *3*(2), 133–144.

Crooks, J., & Graham, J. (1976). Geotechnical properties of the belfast estuarine deposits. *Géotechnique*, *26*(2), 293–315.

Cutter, S. L., & Emrich, C. T. (2006). Moral hazard, social catastrophe: The changing face of vulnerability along the hurricane coasts. *The Annals of the American Academy of Political and Social Science*, *604*(1), 102–112.

Den Haan, E. J. (1994). *Vertical compression of soils. PhD thesis*. Technical University of Delft.

Dial, D. (1970). Pumpage of water in louisiana, 1970. Tech. rep., State of Louisiana Department of Conservation Geological Survey & Department of Public Works.

Dial, D., & Kilburn, C. (1980). Ground-water resources of the gramercy area. *Louisiana: Louisiana Department of Transportation and Development, Office of Public Works Water Resources Technical Report*, *24*.

Dial, D., & Sumner, D. (1989). Geohydrology and simulated effects of pumpage on the new orleans aquifer system at new orleans. *Louisiana: Louisiana Department of Transportation and Development Water Resources Technical Report*, *46*, 63.

Dickinson, G. (1953). Geological aspects of abnormal reservoir pressures in gulf coast louisiana. *AAPG Bulletin*, *37*(2), 410–432.

Dixon, T. H., Amelung, F., Ferretti, A., Novali, F., Rocca, F., Dokka, R., Sella, G., Kim, S.-W., Wdowinski, S., & Whitman, D. (2006). Space geodesy: Subsidence and flooding in new orleans. *Nature*, *441*(7093), 587.

Dokka, R. K. (2006). Modern-day tectonic subsidence in coastal louisiana. *Geology*, *34*(4), 281–284.

Dokka, R. K. (2011). The role of deep processes in late 20th century subsidence of new orleans and coastal areas of southern louisiana and mississippi. *Journal of Geophysical Research: Solid Earth*, *116*(B6).

Erban, L. E., Gorelick, S. M., & Zebker, H. A. (2014). Groundwater extraction, land subsidence, and sea-level rise in the mekong delta, vietnam. *Environmental Research Letters*, *9*(8), 084010.

Erkens, G., Bucx, T., Dam, R., De Lange, G., & Lambert, J. (2015). Sinking coastal cities. *Proceedings of the International Association of Hydrological Sciences*, *372*, 189–198.

Erkens, G., & Sutanudjaja, E. (2015). Towards a global land subsidence map. *Proceedings of the International Association of Hydrological Sciences*, *372*, 83–87.

Fitts, C. R. (2011). *Groundwater science, second edition*. Elsevier.

Galloway, D. L., & Burbey, T. J. (2011). Regional land subsidence accompanying groundwater extraction. *Hydrogeology Journal*, *19*(8), 1459–1486.

Galloway, D. L., Erkens, G., Kuniansky, E. L., & Rowland, J. C. (2016). Preface: Land subsidence processes. *Hydrogeology Journal*, *24*(3), 547–550.

Gambolati, G., Gatto, P., & Freeze, R. A. (1974). Mathematical simulation of the subsidence of venice: 2. results. *Water Resources Research*, *10*(3), 563–577.

Gambolati, G., & Teatini, P. (2015). Geomechanics of subsurface water withdrawal and injection. *Water Resources Research*, *51*(6), 3922–3955.

Gedeon, M., & Mallants, D. (2012). Sensitivity analysis of a combined groundwater flow and solute transport model using local-grid refinement: a case study. *Mathematical Geosciences*, *44*(7), 881–899.

Gunduz, Z., & Arman, H. (2007). Possible relationships between compression and recompression indices of a low-plasticity clayey soil. *Arabian Journal for Science and Engineering*, *32*(2), 179.

Gupta, H. V., Kling, H., Yilmaz, K. K., & Martinez, G. F. (2009). Decomposition of the mean squared error and nse performance criteria: Implications for improving hydrological modelling. *Journal of Hydrology*, *377*(1-2), 80–91.

Hanor, J. S. (1993). Effective hydraulic conductivity of fractured clay beds at a hazardous waste landfill, louisiana gulf coast. *Water Resources Research*, *29*(11), 3691–3698.

Harris, G. D., & Fuller, M. L. (1904). Underground waters of southern louisiana, with discussions of their uses for water supplies and for rice irrigation. Tech. rep., Govt. print. off.,.

Højberg, A., & Refsgaard, J. (2005). Model uncertainty–parameter uncertainty versus conceptual models. *Water Science and Technology*, *52*(6), 177–186.

Hough, B. K. (1957). *Basic Soils Engineering.*. Ronald Press Co., New York.

Jacob, C. E. (1940). On the flow of water in an elastic artesian aquifer. *Eos, Transactions American Geophysical Union*, *21*(2), 574–586.

Jafari, N. H., Harris, B. D., & Stark, T. D. (2018). Geotechnical investigations at the caminada headlands beach and dune in coastal louisiana. *Coastal Engineering*, *142*, 82–94.

Johnson, A. I., et al. (1967). Specific yield: compilation of specific yields for various materials. *Geological survey water supply paper*.

Jones, C. E., An, K., Blom, R. G., Kent, J. D., Ivins, E. R., & Bekaert, D. (2016). Anthropogenic and geologic influences on subsidence in the vicinity of new orleans, louisiana. *Journal of Geophysical Research: Solid Earth*, *121*(5), 3867–3887.

Kaneko, S., & Toyota, T. (2011). Long-term urbanization and land subsidence in asian megacities: an indicators system approach. In *Groundwater and Subsurface Environments*, (pp. 249–270). Springer.

Kazmann, R. G., & Heath, M. M. (1968). Land subsidence related to ground-water offtake in the new orleans area. *GCAGS Transactions*.

Kolb, C. R., & Van Lopik, J. R. (1966). Depositional environments of the mississippi river deltaic plain—southeastern louisiana. *Houston Geological Society*.

Kooi, H., Bakr, M., de Lange, G., den Haan, E., & Erkens, G. (2018). *User guide to SUB-cr - a MODFLOW package for land subsidence and aquifer system comapction that includes creep*. Deltares.

Kooi, H., & Yuherdha, A. (2018). *Updated subsidence scenarios Jakarta, MODFLOW SUB-CR calculations for Sunter, Daan Mogot and Marnda*. Deltares.

Kowalsky, M., Finsterle, S., Williams, K. H., Murray, C., Commer, M., Newcomer, D., Englert, A., Steefel, C. I., & Hubbard, S. (2012). On parameterization of the inverse problem for estimating aquifer properties using tracer data. *Water Resources Research*, *48*(6).

Kuecher, G. J. (1994). Geologic framework and consolidation settlement potential of the lafourche delta, topstratum valley fill; implications for wetland loss in terrebonne and lafourche parishes, louisiana. *LSU Historical Dissertations and Theses*.

Lovelace, J. (1991). Water use in louisiana, 1990. Tech. rep., U.S. Department of the Interior U.S. Geological Survey.

Lovelace, J., & Johnson, P. (1996). Water use in louisiana, 1995. Tech. rep., Departement of Transporation and Development.

Lurry, L. (1987). Pumpage of water in louisiana, 1985. Tech. rep., Department of the Interior U.S. Geological Survey.

Martin, P., & Frind, E. (1998). Modeling a complex multi-aquifer system: The waterloo moraine. *Groundwater*, *36*(4), 679–690.

McDonald, M. G., & Harbaugh, A. W. (1988). *A modular three-dimensional finite-difference ground-water flow model*, vol. 6. US Geological Survey Reston, VA.

McFarlan Jr, E., & LeRoy, D. (1988). Subsurface geology of the late tertiary and quaternary deposits, coastal louisiana and the adjacent continental shelf. *Transactions - Gulf Coast Association of Geological Societies*, *38*.

Meinzer, O. E. (1928). Compressibility and elasticity of artesian aquifers. *Economic Geology*, *23*(3), 263–291.

Mesri, G., & Funk, J. (2014). Settlement of the kansai international airport islands. *Journal of Geotechnical and Geoenvironmental Engineering*, *141*(2), 04014102.

Mesri, G., & Godlewski, P. M. (1977). Time-and stress-compressibility interrelationship. *Journal of Geotechnical and Geoenvironmental Engineering*, *103*(ASCE 12910).

Mesri, G., Kelly, W., Vallee, R., & Andersland, O. (1973). Ceofficient of secondary compression (discussion). *Journal of Soil Mechanics & Foundations Div*, *99*(Proc Paper).

Minderhoud, P., Erkens, G., Pham, V., Bui, V. T., Erban, L., Kooi, H., & Stouthamer, E. (2017). Impacts of 25 years of groundwater extraction on subsidence in the mekong delta, vietnam. *Environmental Research Letters*, *12*(6), 064006.

Mishra, S., Deeds, N., & Ruskauff, G. (2009). Global sensitivity analysis techniques for probabilistic ground water modeling. *Groundwater*, *47*(5), 727–744.

Nicholls, R. J., Wong, P. P., Burkett, V., Codignotto, J., Hay, J., McLean, R., Ragoonaden, S., Woodroffe, C. D., Abuodha, P., Arblaster, J., et al. (2007). Coastal systems and low-lying areas. *Climate Change 2007: Impacts, Adaptation and Vulnerability. Contribution of Working Group II to the Fourth Assessment Report of the Intergovernmental Panel on Climate Change*, (pp. 315–356).

NNI (2012). Nen9997-1+c1: Geotechnical design of structures; part 1: General rules (in dutch). *Nederlands Normalisatie Instituut (Dutch Normalization Institute)*, (p. 306).

Phien-Wej, N., Giao, P., & Nutalaya, P. (2006). Land subsidence in bangkok, thailand. *Engineering geology*, *82*(4), 187–201.

Pianosi, F., Beven, K., Freer, J., Hall, J. W., Rougier, J., Stephenson, D. B., & Wagener, T. (2016). Sensitivity analysis of environmental models: A systematic review with practical workflow. *Environmental Modelling & Software*, *79*, 214–232.

Poland, F., & Davis, H. (1969). Land subsidence due to withdrawal of fluids. *Reviews in engineering geology*, *2*, 187–270.

Prakken, L. B. (2009). *Groundwater resources in the New Orleans area, 2008*. 80. Louisiana Department of Transportation and Development.

Refsgaard, J. C., Christensen, S., Sonnenborg, T. O., Seifert, D., Højberg, A. L., & Troldborg, L. (2012). Review of strategies for handling geological uncertainty in groundwater flow and transport modeling. *Advances in Water Resources*, *36*, 36–50.

Riley, F. S. (1969). Analysis of borehole extensometer data from central california. *Land subsidence*, *2*, 423–431.

Rollo, J. (1966). Groundwater resources of the greater new orleans area, louisiana: La. dept. *Public Works and Lousisian Geological Survey. Bull*.

Rushton, K. R., & Redshaw, S. C. (1979). *Seepage and groundwater flow: Numerical analysis by analog and digital methods*. Chichester.

Sargant, P. (2002). Water use in louisiana, 2000. Tech. rep., Departement of Transporation and Development.

Sargant, P. (2007). Water use in louisiana, 2005. Tech. rep., Departement of Transporation and Development.

Sargent, B. P. (2011). Water use in louisiana, 2010. Tech. rep., Louisiana Department of Transportation and Development.

Snider, J., & Forbes, M. (1961). Pumpage of water in louisiana, 1960. Tech. rep., Louisiana Department of Public Works & Department of Conservation Louisiana Geological Survey.

Snowden, J. O., Ward, W. C., & Studlick, J. (1980). Geology of greater new orleans: its relationship to land subsidence and flooding.

Sun, A. Y., Green, R., Swenson, S., & Rodell, M. (2012). Toward calibration of regional groundwater models using grace data. *Journal of Hydrology*, *422*, 1–9.

Syvitski, J. P., Kettner, A. J., Overeem, I., Hutton, E. W., Hannon, M. T., Brakenridge, G. R., Day, J., Vörösmarty, C., Saito, Y., Giosan, L., et al. (2009). Sinking deltas due to human activities. *Nature Geoscience*, *2*(10), 681.

Taylor, D. W., & Merchant, W. (1940). A theory of clay consolidation accounting for secondary compression. *Journal of Mathematics and Physics*, *19*(1-4), 167–185.

Terzaghi, K. (1925). Principles of soil mechanics, iv—settlement and consolidation of clay. *Engineering News-Record*, *95*(3), 874–878.

Theis, C. V. (1935). The relation between the lowering of the piezometric surface and the rate and duration of discharge of a well using ground-water storage. *Eos, Transactions American Geophysical Union*, *16*(2), 519–524.

Tolman, C. F., & Poland, J. F. (1940). Ground-water, salt-water infiltration, and ground-surface recession in santa clara valley, santa clara county, california. *Eos, Transactions American Geophysical Union*, *21*(1), 23–35.

Tomaszewski, D. J. (2003). *Ground-water Resources Along the Lower Mississippi River, Southeastern Louisiana*. 69. Louisiana Department of Transportation and Development.

Turnadge, C., Mallants, D., & Peeters, L. (2018). Sensitivity and uncertainty analysis of a regional-scale groundwater flow model featuring coal seam gas extraction. Tech. rep., CSIRO Land and water.

Van Asselen, S., Stouthamer, E., & Van Asch, T. W. (2009). Effects of peat compaction on delta evolution: a review on processes, responses, measuring and modeling. *Earth-Science Reviews*, *92*(1-2), 35–51.

Vermeulen, P., Burgering, L., Roelofsen, F., Minnema, B., & Verkaik, J. (2018). *iMOD User Manual V4.3*. Deltares.

Vipulanandan, C., Ahossin Guezo, Y., Bilgin, Ö., Yin, S., & Khan, M. (2008). Recompression index (cr) for overconsolidated soft clay soils. In *GeoCongress 2008: Characterization, Monitoring, and Modeling of GeoSystems*, (pp. 68–75).

Walter, W. (1982). Pumpage of water in louisiana, 1980. Tech. rep., United States Department of the Interior Geological Survey.

White, V., & Prakken, L. (2015). Water resources of st. charles parish, louisiana. Tech. rep., U.S. Geological Survey.

Whiteman, C. (1980). Measuring local subsidence with extensometers in the baton rouge area, louisiana, 1975-79. *Louisiana Department of Public Works Water Resources Technical Report*, *20*.

Wolstencroft, M., Shen, Z., Törnqvist, T. E., Milne, G. A., & Kulp, M. (2014). Understanding subsidence in the mississippi delta region due to sediment, ice, and ocean loading: Insights from geophysical modeling. *Journal of Geophysical Research: Solid Earth*, *119*(4), 3838–3856.

Wu, J., & Zeng, X. (2013). Review of the uncertainty analysis of groundwater numerical simulation. *Chinese Science Bulletin*, *58*(25), 3044–3052.

Xue, Y.-Q., Zhang, Y., Ye, S.-J., Wu, J.-C., & Li, Q.-F. (2005). Land subsidence in china. *Environmental geology*, *48*(6), 713–720.

Ye, M., Pohlmann, K. F., Chapman, J. B., Pohll, G. M., & Reeves, D. M. (2010). A model-averaging method for assessing groundwater conceptual model uncertainty. *Groundwater*, *48*(5), 716–728.

Yuill, B., Lavoie, D., & Reed, D. J. (2009). Understanding subsidence processes in coastal louisiana. *Journal of Coastal Research*, (pp. 23–36).

Zeng, X., Wang, D., & Wu, J. (2012). Sensitivity analysis of the probability distribution of groundwater level series based on information entropy. *Stochastic environmental research and risk assessment*, *26*(3), 345–356.

Zhou, Z., Guo, Q., & Dou, Z. (2013). Delayed drainage of aquitard in response to sudden change in groundwater level in adjacent confined aquifer: Analytical and experimental studies. *Chinese Science Bulletin*, *58*(25), 3060–3069.

Zhuang, C., Zhou, Z., Zhan, H., & Wang, G. (2015). A new type curve method for estimating aquitard hydraulic parameters in a multi-layered aquifer system. *Journal of Hydrology*, *527*, 212–220.

A Fit casing and extraction yields.